EXPLORATIONS OF THE REMNANT EXOPLANETARY DEBRIS DISKS AROUND WHITE DWARF STARS

Erik D. Dennihy

A dissertation submitted to the faculty at the University of North Carolina at Chapel Hill in partial fulfillment of the requirements for the degree of Doctor of Philosophy in the Department of Physics and Astronomy.

Chapel Hill
2018

Approved by:

J. Christopher Clemens

Fabian Heitsch

John H. Debes

Rosa Tamara Branca

Nicholas M. Law

ABSTRACT

Erik D. Dennihy: Explorations of the Remnant Exoplanetary Debris Disks around White Dwarf Stars.
(Under the direction of J. Christopher Clemens.)

Always amenable to modern astrophysical needs, the compact degenerate remnants of stars like our Sun known as white dwarf stars have recently been put into service as exoplanetary laboratories. Their nominally pure hydrogen or helium atmospheres reveal pollution from the debris of crushed up exoplanets, and our understanding of the physics of their atmospheres provides a means to explore the chemical makeup of the rocky bodies they accrete. This thesis work will build on observations of the exoplanetary systems around white dwarf stars by providing new discoveries of such systems, including one that appears to have accreted the crust of an exo-earth analogue. We also pioneer a novel discovery technique which is capable of both revealing new systems and isolating the most interesting among them. Some of our new observations required a major upgrade to a facility class scientific instrument at the Southern Astrophysical Research Telescope in Chile, and we detail the design and implementation of this new upgrade which is now available to the entire US astronomical community. With this upgrade, we discovered a rapidly evolving white exoplanetary system which both challenges the existing theories of white dwarf exoplanetary system evolution and provides the only path forward to test such theories on a reasonable timeline. We conclude with a discussion of the impact these new observations and discovery tools have on the field, and the future directions they enable.

ACKNOWLEDGMENTS

The work presented in this thesis is my own, but it would not have been possible without the contributions of many along the way. I specifically acknowledge a few of these people here, but have been fortunate to receive support from many more, and am forever grateful to all those involved.

Financial support for this work has been provided by a variety of sources, all of which deserve specific acknowledgment. The department of Physics and Astronomy provided early support through a Teaching Assistant appointment which was quite enjoyable. The SOAR telescope provided several Summers of financial support over the years, and substantial travel support to and from the telescope. The National Science Foundation provided the bulk of my research support through grant number AST-1413001, enabling me to focus on individual research projects. Finally, the Royster Society of Fellows within the graduate school provided a generous fellowship during my final year of study allowing me to focus entirely on the completion of this work, and I would like to acknowledge Thomas S. and Helena Borda Royster and Snowden and Elspeth Merck Henry for this year of support which truly enhanced my graduate education.

I am thankful for the support and dedication to the role of my advisor, Chris Clemens. I am particularly thankful for his encouragement to pursue new ideas and willingness to adopt the opposing view once I had them. These daily debates, discussions, and viewpoint reversals defined for me what it means to be a scientist.

I acknowledge the comments, advice, and direction provided by the members of my thesis committee, Fabian Heitsch, Nick Law, Tamara Branca, and John Debes. In particular, I would like acknowledge John Debes for always being open and willing to share research ideas, many of which feature prominently this work.

I acknowledge the technical support and expertise of the crew of the SOAR telescope and the UNC Machine shop, particularly in their support of my instrumentation projects. Their skill and patience in the early stages of my instrumentation development ensured the success of these projects.

I acknowledge my research group for their patience with my sometimes manic approach to day-to-day work. Over the years, this role of stabilizing counter-weight has been provided by various people including Josh Fuchs, Bart Dunlap, Stephen Fanale, JJ Hermes, Ben Kaiser, and Josh Reding among others. Bart Dunlap deserves particular recognition for always being willing to discuss ideas over coffee, and providing a daily example of what it means to be truly curious.

Finally, I would like to acknowledge the support of my friends and family, both near and far. Thank you for always being there to remind that there was always a way through no matter how poorly things were going, and when some pursuits inevitably failed, for unabashedly declaring that it was the science that was at fault, not me. I was honored to receive this unwavering support over the years and its effects are felt throughout this thesis.

TABLE OF CONTENTS

LIST OF FIGURES

LIST OF TABLES

LIST OF ABBREVIATIONS AND SYMBOLS

DA	White Dwarf with observed hydrogen lines
DAZ	Metal Polluted DA
DB	White Dwarf with observed helium lines
DBZ	Metal Polluted DB
DO	White Dwarf with observed helium lines
$\log g$	log of the surface gravity (cm s^{-2})
$R_{\odot}$	Solar radius
SDSS	Sloan Digital Sky Survey
$T_{\rm eff}$	Effective Temperature
WD	White Dwarf
SED	Spectral Energy Distribution
WISE	Wide-Field Infrared Survey Explorer
SOAR	Southern Astrophysical Research Telescope
EC	Edinburgh-Cape Blue Object Survey
$R_{\rm WD}$	White Dwarf Radii
e	Eccentricity

CHAPTER 1: INTRODUCTION

Up until the early 1990s studies of planets were limited to those within our own solar system. The dramatic announcement of the discovery of two extrasolar planets around the Pulsar B1257+12, a rapidly rotating remnant of a star that had completed its evolution, confirmed that not only do planets exist beyond our solar system, there is a good chance they can outlive their host star (Wolszczan & Frail, 1992). While discoveries of exoplanets now number in the thousands, our knowledge is largely limited to occurrence rates, orbital periods, masses, and occasionally bulk densities, as the the host star vastly outshines its exoplanets. While the next generation of giant telescopes and astronomical instruments offers the promise of direct imaging and chemical composition studies of exoplanets, careful studies of stellar remnants can provide answers to these questions today.

This thesis work will build on observations of the exoplanetary systems around the stellar remnants of low to intermediate mass stars known as white dwarf stars. We provide new discoveries of such systems using a novel discovery technique which is capable of both revealing new systems and isolating the most interesting among them. Our work required a major upgrade to a facility class scientific instrument at the Southern Astrophysical Research Telescope in Chile, and we detail the design and implementation of this new upgrade. Science highlights made possible by this instrument upgrade include the discovery of a rapidly evolving system which both challenges the existing theories of exoplanetary system evolution around white dwarf stars and provides the only way to test such theories on a reasonable timeline. We conclude with a discussion of the impact of these new observations and tools on the field, and the future directions they enable.

In this introduction we begin by reviewing the late stages of stellar evolution and the de-stabilizing effects they have on surrounding planetary systems. We then discuss the

more specific case of the remnant exoplanetary systems around white dwarf stars, which are the final stage of evolution for low to intermediate mass stars including our Sun. We briefly discuss the atmospheric physics of white dwarf stars and how their atmospheres enable measurements of the exoplanetary material deposited at their surface, making them sensitive laboratories for exoplanetary composition analyses (Jura & Young, 2014). We discuss the tidal disruption model, which is the favored dynamical model for delivering exoplanetary material to the white dwarf surface, and give an overview of the current state of observations and theoretical work describing this process and the exoplanetary debris accretion disks that result. Finally, we give a brief overview of our work, and the ways in which our observations can be used to drive the field forward.

1.1 White Dwarf Stars as Exoplanetary Laboratories

The ultimate fate of low and intermediate mass stars including our Sun, which make up nearly 97% of the stars in our galaxy, is to end their evolution as a compact, degenerate white dwarf star. As the core of the star begins to deplete its reservoir of hydrogen, energy production decreases leading to core contraction, which raises the core burning temperature ultimately resulting in higher energy production than before. The core goes through a series of shell burning and contraction events until reaching high enough temperatures and densities to begin burning helium fuel into carbon and oxygen, which is the final nuclear fusion product for low-to-intermediate mass stars. The outer layers of the star to expand in response to these changes until they are eventually expelled revealing a compact, degenerate core of spent nuclear fuel. The stellar remains is known as a white dwarf star. The white dwarf stage marks the end state of a lifetime of stellar evolution, and stars of this type are colloquially referred to as 'dead' as they are no longer able to convert nuclear fuel into energy via nuclear fusion. White dwarf stars spend the remainder of their existence slowly cooling down. The fate of any planetary system accompanying the star through this transition is more eventful.

1.1.1 Stellar and Planetary System Evolution

As stars begin their departure from the main sequence of normal hydrogen burning the resulting expansion of the outer layers has several notable effects on the surrounding planetary system. The most destructive is the engulfment of close-in bodies. The Sun's outer layers could reach the orbit of Mars (Schröder & Connon Smith, 2008), engulfing any bodies it encounters during expansion. Bodies whose orbits exist beyond this expansion radius face a range of de-stabilizing effects. Mass-loss during the post-main-sequence evolution should expand the orbits of bodies that survive engulfment (Villaver & Livio, 2007), and the ever-increasing luminosity of the post-main-sequence star has the potential to destroy smaller bodies by sublimation (Stern et al., 1990), tidal forces (Mustill & Villaver, 2012), and second order effects such as radiation induced runaway rotation (Veras et al., 2014a).

Despite all of these competing destructive effects, the majority of the planetary bodies in a system like our own solar system are expected to survive and outlive their host star. But their large separations from their host star and low intrinsic brightness make them undetectable by traditional exoplanet observing methods such as through radial velocity variations, transits, or direct imaging. Instead, we must infer their existence through careful examination of the white dwarf star.

1.1.2 Atmospheric Metal Pollution of White Dwarf Stars by Exoplanetary Remnants

The primary utility of white dwarfs as expolanetary laboratories comes from their propensity to display of the chemical composition of any material that arrives at their surface. While it is true that main-sequence stars also regularly accrete exoplanetary bodies (e.g. comets entering the solar atmosphere), the simple stellar structure of the white dwarf star allows us to quickly distinguish between material that is inherent to the stellar atmosphere, and material that was recently deposited.

For most white dwarf stars, their primary atmospheric constituent is hydrogen. We

refer to these hydrogen atmosphere white dwarf stars as type DA. The second most common white dwarf stars have primarily helium atmospheres and are referred to as type DB or DO. White dwarf stars which also show heavier metals in their atmosphere have the letter Z appended to their primary classification (e.g. DAZ). Owing to their strong surface gravity, heavy elements in white dwarf atmospheres will sink out of view through a process called atmospheric diffusion (Koester & Wilken, 2006). The amount of time it takes a metal species to sink below the observable photosphere is referred to as its 'diffusion timescale', and it is this knowledge that allows us to translate the observed atmospheric abundances of metals in white dwarf stars into accretion rates. There are a handful of physical processes that can support heavier elements in the atmospheres of white dwarf stars for extended periods, such as radiative levitation in the hottest stars (Chayer & Dupuis, 2010) and convective mixing in cooler stars, but for a large range of temperature evolution in the DA type stars the diffusion timescales for heavy elements can be as short as days (Koester et al., 2014), implying that any observation of photospheric metals is from ongoing accretion.

Observations of atmospheric metal pollution in white dwarf stars date back as far as 1917 (Zuckerman, 2015), but the understanding of exoplanetary accretion as the origin of the metals is fairly recent. Once this theory for the exoplanetary origin of metals became widely accepted, high-resolution spectroscopic studies transformed white dwarf stars into the most sensitive known probes of chemical compositions of rocky exoplanets (Jura & Young, 2014).

Results from careful studies of metal-polluted white dwarf atmospheres are profound and wide-ranging. A recent comprehensive study by Xu et al. (2014) demonstrated that the bulk abuandances of accreted bodies roughly match what we see in Earth. Figure 1.1 succinctly captures this result. Other detailed studies of individual objects have revealed cometary-like patterns (Xu et al., 2017) and water-rich planetesimals (Dufour et al., 2012; Raddi et al., 2015). There have even been claims that white dwarf atmospheres offer the promise of detecting signatures of tectonic activity on rocky extrasolar bodies (Jura et al., 2014),

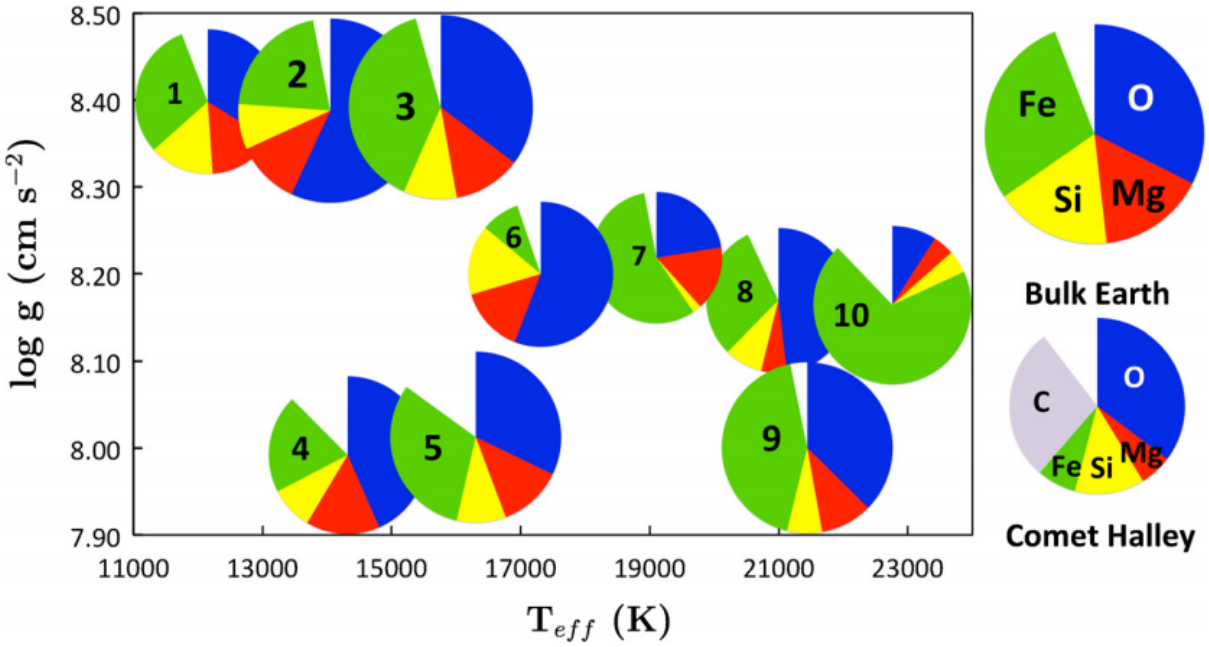

Figure 1.1: Exoplanetary abundances measured from atmospheric pollution in a sample of well-studied DA white dwarf stars from Xu et al. (2014). The bulk abundances suggest white dwarf stars overwhelmingly accrete rocky, Earth-like material as opposed to carbonaceous, comet-like material.

demonstrating the endless possibilities of these fully equipped exoplanetary laboratories.

1.2 Delivery of Exoplanetary Remnants to the White Dwarf Surface

While extremely powerful, these abundance measurements rely heavily on our understanding of atmospheric physics in the white dwarf stars, and the exact method for delivering the surviving exoplanetary remnants from the outer reaches of the exoplanetary system to the white dwarf surface remains unsolved. The leading theory is known as the 'tidal disruption model', and was first introduced by (Jura, 2003) to explain the atmospheric metals and excess infrared radiation observed around the white dwarf star G29-38. This model for the the deposition of remnant debris onto the white dwarf surface can be thought of as occurring in three distinct phases: the first is the scattering of smaller, rocky bodies onto star-grazing orbits. The second phase is the destruction of the scattered bodies via the strong strong tidal forces imparted by close passage to the white dwarf star (tidal disruption) and the formation

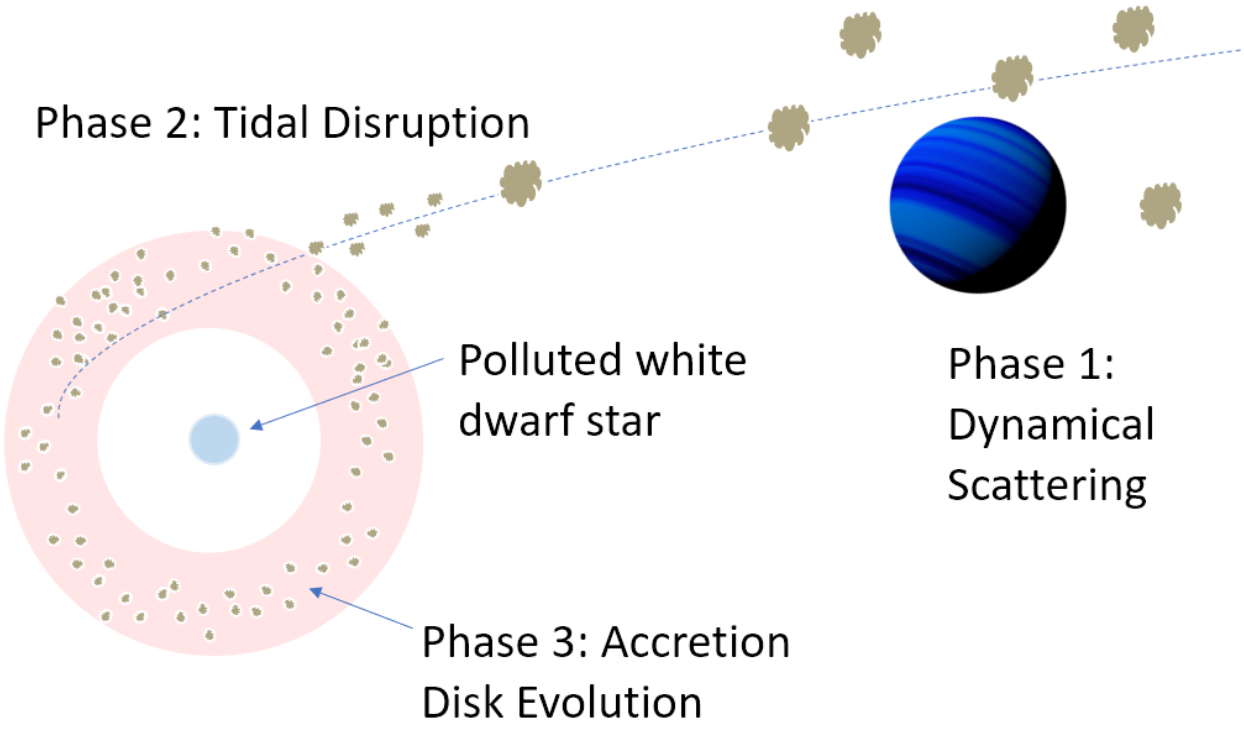

Figure 1.2: Cartoon showing the various phases of exoplanetary debris delivery to the white dwarf surface in the tidal disruption model, resulting in atmospheric metal pollution. Phase 1 represents the dynamical interactions between planetesimals which scatter smaller bodies in towards the white dwarf star. In Phase 2 the scattered bodies are shredded by the extreme tidal forces of the white dwarf star and settle into a compact debris disk. Phase 3 includes the transport of material through the debris disk, before finally arriving at the white dwarf surface. The work in this thesis focuses on the third stage of debris disk evolution.

of a compact accretion disk around the white dwarf star. The third and final phase is the transfer of material from the accretion disk onto the white dwarf surface. We briefly review the theoretical foundation for each phases individually in the following subsections.

1.2.1 Phase 1: Dynamical Scattering of Planetesimals

The concept of post-main sequence dynamical interactions scattering planetesimals on to compact destructive orbits with the white dwarf star was first explored by Debes & Sigurdsson (2002). In this early study, the authors demonstrated that the evolution of stars off of the main-sequence can de-stabilize multiple planet systems, providing a feasible exoplanetary source for the heavy metals seen in white dwarf atmospheres. As computational

resources improved later studies were able to explore this problem in depth, focusing on specific scattering scenarios. Bonsor et al. (2011) explored the effects of post-main sequence evolution on a kuiper belt analog, finding that a single planet interacting at the edges of a Kuiper belt can readily scatter enough material into the inner solar system to explain the observed accretion rates of metals in white dwarf atmospheres, though they did not follow the material all the way down the white dwarf surface.

Debes et al. (2012b) considered the dynamical scattering of smaller objects by a larger body through interactions at mean motion resonances, rather than close encounters, expanding the reach of large bodies to scatter smaller bodies. Bonsor & Veras (2015) explored the effect of wide binary systems on the planetary systems that surround each star, demonstrating that binary systems could scatter smaller bodies just as efficiently as heirarchical planet systems. And recently Frewen & Hansen (2014) and Mustill et al. (2017) demonstrated the scattering efficiency of eccentric planets and super-earths, expanding the range of planetary systems that are though to scatter smaller bodies in towards the white dwarf star.

Together, these works demonstrate that there a multitude of options for planetary scattering, and they should not be considered as mutually exclusive scenarios. There could however be a way to differentiate between theses scenarios, as different sources of rocky material are likely to have different chemical signatures in the white dwarf atmosphere, though none of the scattering scenarios have been preferred or ruled out. The truth likely involves some combination of all of these methods and others that have yet to be explored. In fact, in the one system where an active disruption process via irregularly shaped and variable transits around the white dwarf star 1145+017 (see subsection 1.3.3), the scattered body appears to be largely in-tact and on a circular orbit (Gurri et al., 2017), suggesting our picture is far from complete.

1.2.2 Phase 2: Tidal Disruption of Planetesimals and Exoplanetary Debris Accretion Disk Formation

Once the planetesimals have been scattered onto star-grazing orbits, they do not need to directly impact the white dwarf surface to be destroyed. As the white dwarf star is a massive, compact object, it has a strong gravitational field, and the differential gravitational forces imparted on a body moving through this gravitational field are often sufficient to tear bodies apart. This process is known as tidal disruption, and is also observed when stars pass too closely to super-massive blackholes (Hills, 1975). The radius within which a body is expected to be destroyed by tidal forces is thus known as the 'Hill sphere', the 'Roche radius', or the 'tidal disruption radius'.

The calculation of the tidal disruption radius primarily depends on the mass and radius of the central, disrupting object (in our case the white dwarf star) and the density of the disrupted body, but it can also depend on the different material properties of the body such as its tensile strength. If we take the typical density of scattered planetesimals to be similar to the asteroids in our Solar System, the average mass and radius white dwarf star will tidally disrupt rocky bodies which pass within approximately 1 $R_{\odot}$, though this rough calculation ignores the tensile strength of the body.

Once planetesimals pass within this radius their disruption is inevitable though it is unknown how long it may take an object to be completely disrupted or at what particle scale the disruption ceases. Debes et al. (2012b) considered the case of a rubble pile approximation to an asteroid, which is a collection of particles held together by self-gravity, and find that objects are spread out into a narrow, elliptical stream of debris within their initial interaction.

In a series of papers, Veras et al. (2014b) expanded the rubble pile disruption simulations to explore the efficiency of disruption as a function of the planetesimals' initial orbital parameters. Their findings are similar to Debes et al. (2012b), and they conclude that the bodies should be completely disrupted down to the resolution of the particle sizes used in the simulation within a few passages, independent of the assumed orbits. They also find

that the resulting debris is broadly distributed in large streams on highly eccentric orbits.

However, as we will discuss in section 1.3, observations of the exoplanetary debris accretion disks so far indicate that the accretion disks that result from these disruption events are entirely contained within about 1 $R_{\odot}$, meaning the debris must undergo a significant amount a circularization and orbital shrinking following disruption. As a follow-up to their disruption study, Veras et al. (2015) later considered the contribution of radiation forces from the white dwarf star to shrinking and circularizing the orbits of the disrupted debris, finding that full circularization and shrinking of the debris can be accomplished within a reasonable timescale by radiation forces alone, though the timescale is highly dependent on the assumed particle size (Veras et al., 2015).

In contrast with the previous studies which assumed collisionless particles, Kenyon & Bromley (2017a) performed numerical simulations on the collisional environments that could be expected in the orbital plane of recently disrupted planetesimals. Their findings indicate that high velocity collisions between particles can rapidly lead to collisional cascades, which pulverize the disrupted bodies on timescales that are potentially faster than the tidal disruption could occur. This collisional evolution could also lead to more rapid circularization of the material (Kenyon & Bromley, 2017a), and is also expected to produce a significant amount of gas (Kenyon & Bromley, 2017b).

1.2.3 Phase 3: Exoplanetary Debris Accretion Disk Evolution

The third and final stage of transporting material to the white dwarf surface involves the evolution of material through the exoplanetary debris accretion disk. The rate of transfer of material through the accretion disk has the most direct connection to the observed accretion rates in the white dwarf atmospheres, as the white dwarf cannot accrete material faster than the accretion disk can supply. Estimates of the lifetime of the accretion disk before it is completely depleted can also be combined with accretion rates to give estimates on the initial mass of the tidally disrupted body (Wyatt et al., 2014). For the remainder of this

work we will often refer to the exoplanetary debris accretion disk as the 'accretion disk' or the 'debris disk', though they should be considered synonymous.

The primary force responsible for the angular momentum evolution of the debris disk is expected to be provided by the radiation from the white dwarf in the form of Poynting-Roberston drag (hereafter PR drag). Due to the abberation of starlight, particles on circular orbits around a central illuminating source perceive incoming light rays from as having a slight vector projection anti-parallel to their orbital velocity, as opposed to being purely perpendicular, and this component acts as a drag force when interacting with the orbiting particles. The effects of this drag on the debris disks around white dwarfs were explored in detail by Rafikov (2011) and Bochkarev & Rafikov (2011), where they found that the PR drag is most efficient at dragging in material in regions where the disks are optically thin. This can result in an outward-in evolution, where the outer optically thin edge of the debris disk slowly creeps inwards over time (Bochkarev & Rafikov, 2011) leading to a narrow ring-like particle distribution as opposed to a fully filled disk.

In addition to PR drag, at the inner edge of the debris disk, the particles directly exposed to the light from the white dwarf star will be sublimated directly into gas, establishing a physical expectation for the inner radius for the solid particle debris disks around white dwarf stars (Rafikov & Garmilla, 2012). This gaseous debris can then spiral-in toward the white dwarf through viscous angular momentum loss (Rafikov & Garmilla, 2012). If a sufficient amount of gas is allowed to build-up in the same plane as the solid particle debris, the pressure supported gas particles will have velocities which deviate from the purely keplerian velocities of the solid dust particles. This leads to interactions between the solid and gaseous debris in the disk, and angular momentum exchanges can cause the gas to spread outward in addition to its inward migration (Metzger et al., 2012). If conditions are right, this outward spreading of gas can feed back into the evolution of the solid debris, providing an additional drag force and increasing the speed at which material is delivered to the inner edge of the debris disk. This produces even more gas via sublimation, resulting in a runaway process by

which the entire debris disk can be rapidly converted in gas (Metzger et al., 2012).

As the debris disk evolution couples directly to the accretion rate estimates of the metals in the white dwarf atmosphere, observational constraints on the theories of debris disk evolution can assist our interpretations of the chemical abundance estimates we gain from atmospheric analysis. This thesis is therefore focused on observations of existing debris disks and their application to debris disk evolution.

Our results in the evolution of debris disks include the identification of the locus of gaseous and dusty debris disk hosting systems in a new plane for studying dusty debris disks, which could suggest cyclical evolution towards and away from gaseous dominated phases. We also explore the potential for elliptical dust distributions to explain some of the key trends in infrared brightness of dusty debris disks as a function of white dwarf cooling age, which can track the evolution of dusty debris disks over long timescale. Finally, we report the discovery of a rapidly evolving gaseous debris disk and explore new theories for the evolution of gaseous components which can uniquely be tested in this system over the next few years.

1.3 Observations of Exoplanetary Debris Accretion Disks around White Dwarf Stars

Direct observation of the exoplanetary debris in the accretion disks can be accomplished using either the infrared emission from the warm dust that constitutes the solid particulates in the disk or the emission or absorption features that occasionally result from the gaseous component of the disk. Infrared studies of the dust are more common but are often limited to photometry as the debris disks themselves are intrinsically very faint, and infrared spectroscopy of the brightest disks have revealed limited information (Reach et al., 2009; Jura et al., 2009a). Optical spectroscopy can be used to study the disks with gaseous components in emission or absorption (e.g. Gänsicke et al. (2006); Debes et al. (2012a)), though observable gaseous components are rare compared to the observable dust. In this section,

we review the literature on the observations of accretion disks using both the dusty and gaseous components. We will use this review to frame the issues that our work will address, including the need for continued discovery of new systems and new techniques for modeling existing systems.

1.3.1 Infrared Radiation from Dusty Debris

While spectroscopic observations of metals in the atmospheres of white dwarf stars were suggestive of an exoplanetary accretion source, it was well known that an accretion disk source would be required to sustain the atmospheric metals. In a very prescient paper, Graham et al. (1990) invoked a flat dust disk model to explain the discrepancies between the optical and near-infrared pulsation cycles of the white dwarf star G29-38, which had recently been discovered to display an excess of infrared radiation (Zuckerman & Becklin, 1987). This was followed up by the modeling of the excess infrared radiation around the metal polluted white dwarf star G29-38 as a compact, dusty accretion disk, and its connection to the observed atmospheric pollution by Jura (2003). This now seminal paper opened the door to the discovery of remnant exoplanetary systems via the excess infrared light from the dusty components of their debris disks. By comparing the expected near-infrared brightness of models against measured values the sample of white dwarfs with dusty disks rapidly grew. Several techniques were employed in their discovery including targeted searches with the space-based Spitzer Telescope (Kilic et al., 2006; Jura et al., 2007a; Farihi et al., 2008; Barber et al., 2012) and queries of all-sky photometric surveys including the WISE all-sky survey (Debes et al., 2011b; Hoard et al., 2013), and the sample of dusty infrared excess white dwarfs has now grown to over 40 confirmed systems (Rocchetto et al., 2015).

The Jura (2003) model for the dusty debris in the accretion disks has a few properties that have allowed it to be successful in modeling the dusty exoplanetary accretion disks where others have failed. The first is that it assumes the dust to be optically thick to incoming radiation and geometrically flat, perhaps with a scale height only a few particles

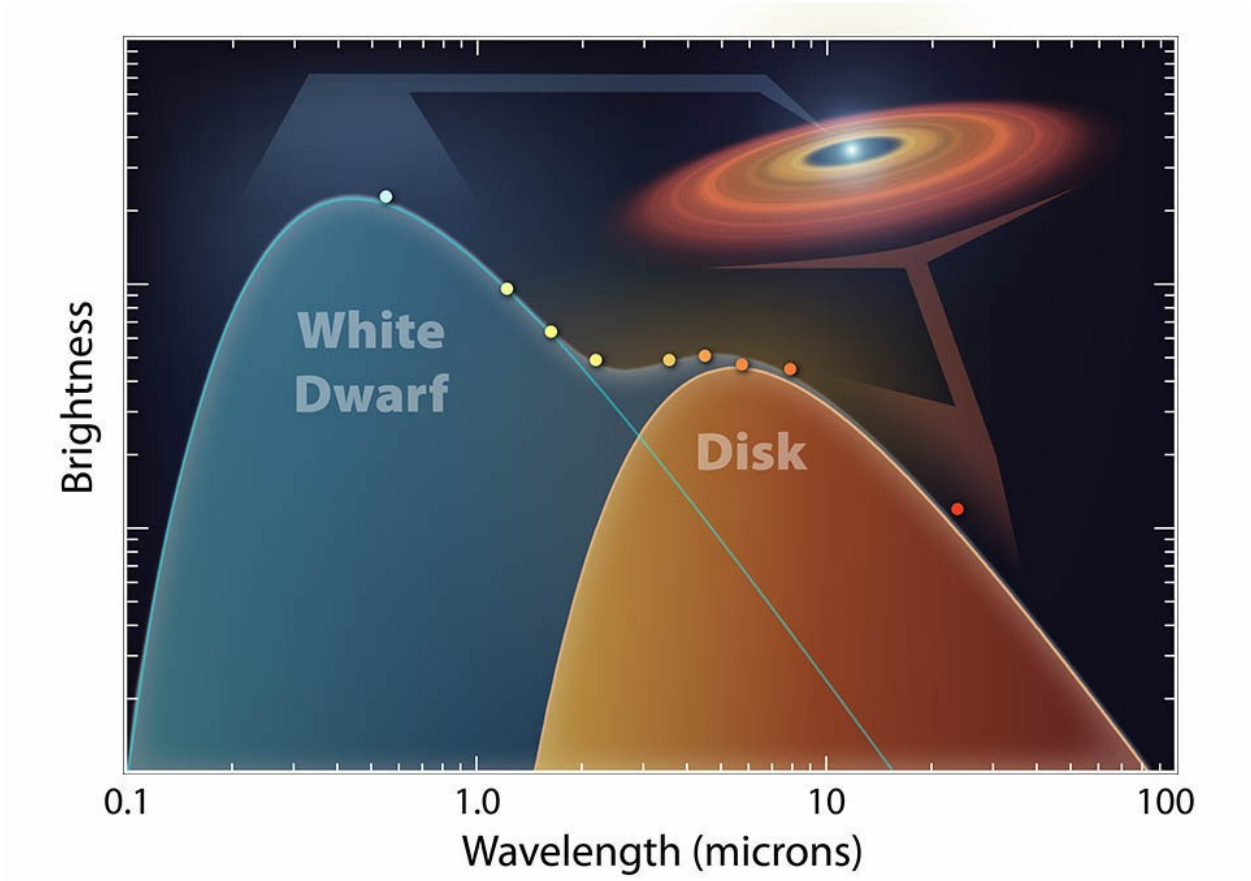

Figure 1.3: Spectral energy distribution of the white dwarf dusty debris disk systems GD 16 (image credit J. Farihi, NASA/JPL-Caltech). The spectral energy distribution includes optical data which is primarily due to the white dwarf star and near-infrared data from the Spitzer Space Telescope which primarily results from the dusty debris disk. The separation of these two components allows us to easily identify dusty debris disk systems around white dwarfs stars via excess infrared radiation.

thick, meaning only the very inner edges of the debris disk are exposed to direct starlight in the absence of any flaring. In this way, the majority of the dust in the disk is protected from the intense radiation of the white dwarf that would otherwise heat the dust to temperatures well above its sublimation point. The dust particles themselves are believed to be small due to the tidal disruption, ranging in size from centimeters to microns. The result of these assumptions is a disk that is heated passively by re-radiation within the disk, with a temperature profile that only depends on the radius from the white dwarf star as described by Chiang & Goldreich (1997) in their modeling of T Tauri Stars. These compact particulate disks can be visualized as resembling the rings of Saturn.

With these geometric assumptions and knowledge of the temperature and radius of the white dwarf star, the contribution of the dusty debris to the infrared portion of the spectral energy distribution can be completely modeled with only three free parameters for the dusty debris: an inner radius, an outer radius, and an inclination relative to the observers line-of-sight. Detailed observations of one of the brightest dusty debris disk hosting white dwarfs, GD 362, required a more complex, warped disk model (Jura et al., 2007b) to reproduce the observed near-infrared features, but for the most part the Jura (2003) model is preferred.

This model not only does a good job in reproducing the observed infrared excesses, but the inferred parameters largely match our physical expectations for the boundaries of the dusty debris (Farihi, 2016). The near-infrared light of the dust debris disk is well fit with dust at temperatures below 1800K, which is a reasonable estimate for the sublimation temperature of the orbiting dust (Rafikov & Garmilla, 2012), establishing an expectation for the inner radius of the dust of around 0.2 $R_{\odot}$. The lack of mid-infrared light suggests the coolest dust at the outer edges is only a few hundred degrees kelvin, corresponding to distances around 1 $R_{\odot}$, roughly equivalent to the tidal disruption radius of the white dwarf star. In these ways, the Jura (2003) model is able to both reproduce the observed infrared excess, and provide support for the tidal disruption origin for the dusty debris.

With an appropriate model for comparison with the data and a growing sample size,

studies have recently begun to explore the bulk properties of the dusty debris that might provide insight into their formation and evolution. In a joint space telescope observing effort Koester et al. (2014) explored the frequency of exoplanetary debris around white dwarf stars evidenced by both the frequency of atmospheric metal pollution and the occurrence rates of infrared bright dusty debris disks. Remarkably, the authors found that 25-50% of white dwarf stars in their sample showed evidence for active accretion (Koester et al., 2014), yet it is estimated that only 1-3% of white dwarf stars display infrared excesses due to dusty debris disks (Farihi, 2016), indicating that most accretion disks go undetected.

In another study of the sample of white dwarfs with confirmed dusty infrared excess from the Spitzer Space Telescope, Rocchetto et al. (2015) considered the ratio of the infrared luminosity of the dusty debris disk (as modeled by a single temperature blackbody) to the infrared luminosity of the white dwarf as a function of white dwarf effective temperature. Figure 1.4 has been adapted from Rocchetto et al. (2015), and summarizes their results by comparing the maximum expected fraction infrared luminosity (dashed line) of a model dusty white dwarf system against the measured fractional infrared luminosity for all confirmed dusty debris disk systems (black dots)

The dashed black line represents the maximum fractional infrared luminosity for a debris disk which fills its entire available area between the sublimation and tidal disruption radii and is viewed in a face-on inclination, representing the maximum brightness that a debris disk can have. The shape of this theoretical brightness maximum curve can be understood as decreasing for higher temperature white dwarfs, as the inner radius of the debris disk is set by the sublimation temperature, which is at larger distances for hotter white dwarfs, and the outer radius of the debris disk is fixed at the tidal disruption radius independent of white dwarf temperature. In this way, hotter white dwarf stars have a smaller area in which solid particulate dust is expected to survive, leading to decreasing maximum fractional infrared luminosities.

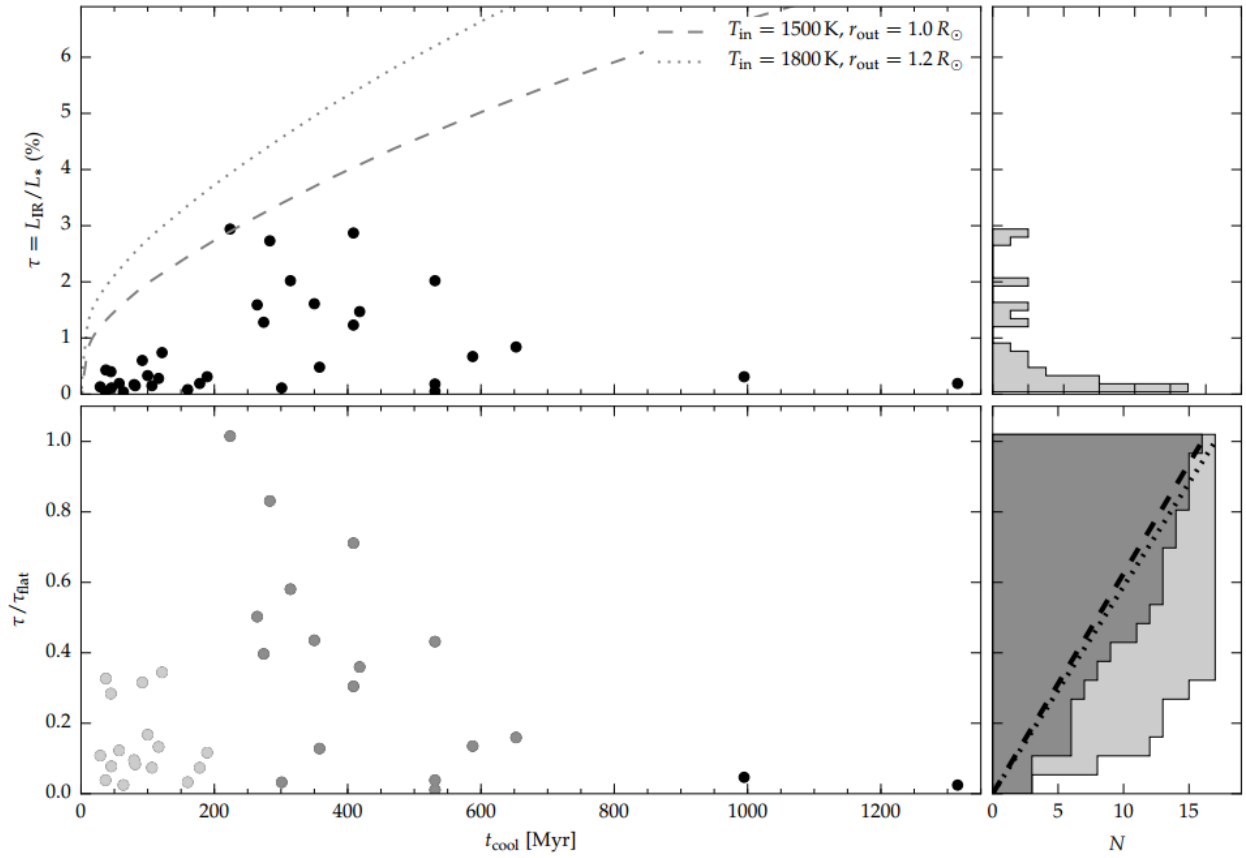

Figure 1.4: Fractional Infrared Luminosity of dusty exoplanetary debris disks plotted as a function of white dwarf cooling ages adapted from Rocchetto et al. (2015). The x-axis could likewise be thought of as decreasing white dwarf effective temperature, as hotter white dwarfs appear on the left-hand side at young cooling ages, and cool white dwarfs appear on the right-hand side at old cooling ages. The fractional infrared luminosities of debris disks around older white dwarfs follow the smooth distribution one would expect from randomly drawn inclinations (see lower panel), while the fractional infrared luminosities of debris disks around young white dwarfs aggregate at low fractional infrared luminosities, suggesting that there is a fundamental difference between disks around young white dwarfs vs disks around old white dwarfs. In section 4.1 we will demonstrate that a geometric model that considers elliptical dust distributions can capture this trend, suggesting that debris disks around young white dwarfs may be more elliptical than their counterparts around older white dwarfs.

Since this dashed curve represents the maximum brightness a disk filling all of its available area could have, one expects all systems to lie below this line in a distribution which is proportional to the sine of the inclination if we assume that all observed disks fill their available area. While this appears to be true for systems at white dwarf cooling ages greater than 200 Myr, there is a dearth of high fractional infrared luminosity systems at white dwarf cooling ages below 200 Myr, indicating that the debris disks in this bin are nominally fainter than their counterparts around older white dwarf stars. Rocchetto et al. (2015) interpret this as evidence that debris disks around young, hot white dwarf stars are narrow and ring-like while those around old, cool white dwarf stars are completely filling their available area. In section 4.1, we will present a new geometric model for the distribution of the dust which includes the possibility of highly eccentric dust orbits, such as those expected immediately after tidal disruption, and show that the delineation between the fractional infrared brightnesses of disks around young and old white dwarf stars can also be produced if the debris disks around younger white dwarf stars are more elliptical, suggesting more frequent or recent formation.

1.3.2 Double-Peaked Emission Lines from Gaseous Debris

While all white dwarfs with dusty debris disks are expected to be producing gas at the inner edge of the debris disk via sublimation, direct observations of this gaseous component are rare. The first announcement by Gänsicke et al. (2006) of metal rich gaseous debris around white dwarf stars included the detection of strong double-peaked emission lines at the wavelengths of the Calcium infrared triplet near 850nm in the SDSS spectrum of the white dwarf star WD 1226+110. Using the formalism developed in Horne & Marsh (1986) to describe emission line formation in optically thick debris disks, Gänsicke et al. (2006) were able to model and constrain the gaseous debris to be completely contained within 1.2 $R_{\odot}$, similar to constraints on the dusty debris in the accretion disks found around other white dwarfs and consistent with the tidal disruption origin. The authors also reported strong

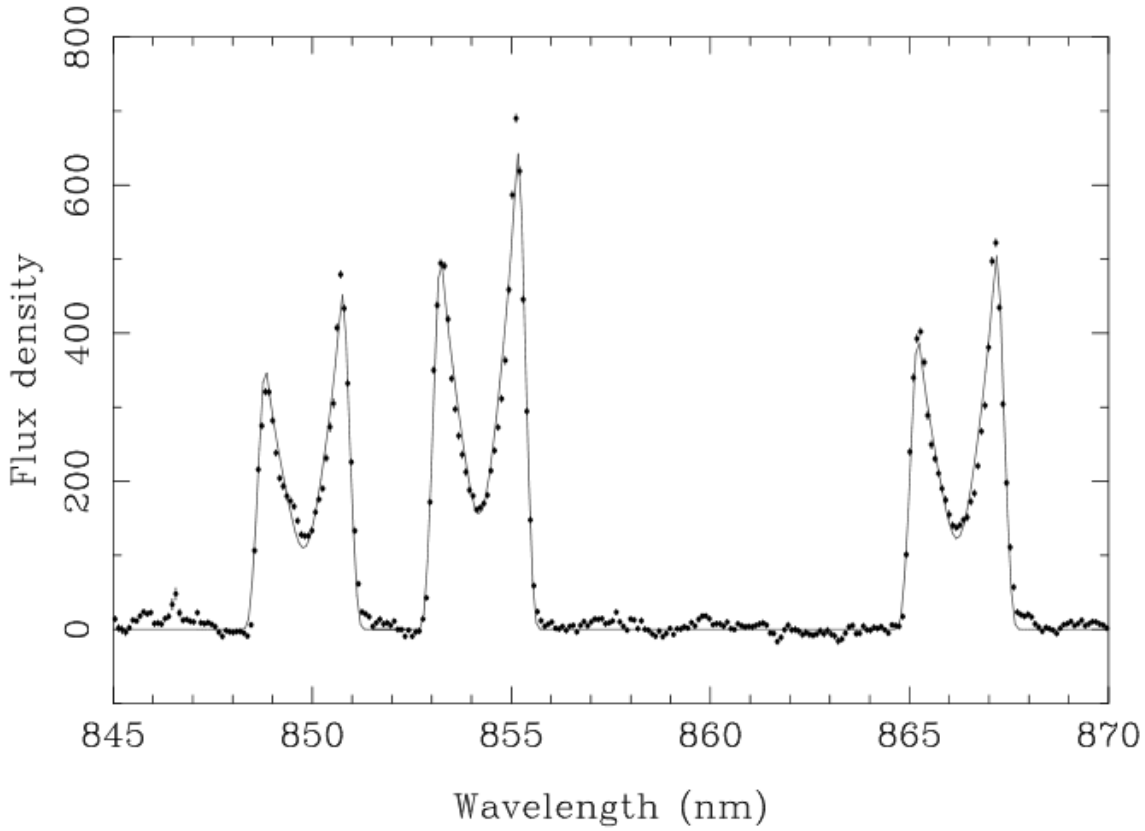

Figure 1.5: The asymmetric double-peaked Calcium infrared triplet emission lines emanating from the gaseous debris disk around WD 1226+110 (Gänsicke et al., 2006). The dots show the observed spectrum, while the solid line shows the optically thin gaseous model used to describe the emission. The observed spectrum is re-produced well by a hot, optically thin metal-rich gaseous disk which lies within the tidal disruption radius of the white dwarf star, suggesting it is also the result of the tidal disruption of a rocky planetesimal.

signatures of ongoing atmospheric metal accretion in parallel with the dusty debris systems. It would later be revealed that WD 1226+110 also displayed a strong, dusty infrared excess (Brinkworth et al., 2009), solidifying its status as the archetypal gaseous and dusty debris disk hosting system. The asymmetric, double-peaked emission lines discovered by Gänsicke et al. (2006) are shown in Figure 1.5

Since the discovery of the gaseous emission lines around WD 1226+110, seven additional systems have been found and confirmed including WD 1043+0855 (Gänsicke et al., 2007), WD 0845+2257 (Gänsicke et al., 2008), HE1349–2305 (Melis et al., 2012), WD 0959-0200 (Farihi et al., 2012), WD0738+1835 (Dufour et al., 2012), WD 1617+1620 (Wilson et al.,

2014), and WD 1144+0529 (Guo et al., 2015). All eight systems show strong double-peaked emission profiles at the Ca II infrared triplet, and a few additional metal species have been observed in emission around WD 1228+110, though the emission at other transitions is much weaker than at the Ca IRT (Gänsicke et al., 2012).

In addition, circumstellar gas has also been observed in absorption around a few systems including WD 1226+110 (Gänsicke et al., 2012), WD 1124-293 (Debes et al., 2012a), PG 0843+516 (Koester et al., 2014), WD 1054-226 (Vennes & Kawka, 2013), and WD 1145+017 (Vanderburg et al., 2015), though they will not be a focus of this thesis work.

All of the systems with gaseous debris in emission have also been shown to display strong infrared excesses, indicative of a corresponding dusty component to the debris disk. However, it is not yet clear why some systems show gaseous debris in emission while others do not. Melis et al. (2010) explored the geometry of the gaseous and dusty components of three systems and found that the gaseous and dusty debris largely overlap in a single disk rather than existing at separate locations, which is another challenging observation to explain given their expected interaction (Metzger et al., 2012). Several theories have come forward to explain the origin of the gaseous emission line systems and the overlap with the dusty debris including the radial migration of gas produced via sublimation at the inner edge of the debris disk (Metzger et al., 2012) and the impact of micro-asteroids on existing debris disks producing gas via high velocity collisions (Jura, 2008), though none have satisfactorily explained why some of these systems contain gas in emission and others do not. The gaseous emission line systems do tend to display higher rates of accretion and infrared luminosity than their non-emitting counterparts (Farihi, 2016). In section 4.2, we will show that in the single temperature blackbody observational plane we developed to discover dusty debris disks systems in chapter 2 the dusty debris disk systems which show gas in emission form a boundary of the dusty debris disk region. We discuss the evolution of systems within the blackbody plane, and show that population synthesis techniques can be used to explore properties that make these systems unique.

Another key property that appears to be shared amongst the systems with gaseous emission lines is significant emission profile evolution on timescales of decades (Manser et al., 2016a), providing an opportunity to directly study debris disk evolution in these systems. The first discovery of emission profile evolution by (Wilson et al., 2014) detailed the gradual disappearance of the emission line feature in WD 1617+1620 over the course of 15 years of observations. This appeared to indicate either accretion of the gaseous debris or a recent impact event that may have only temporarily heated the gas (Wilson et al., 2014).

This work was followed up by more than a decade of observations of the emission profiles around WD 1226+110, which showed secular evolution of the asymetries in the emission profiles, slowly shifting from red-dominated emission profiles to blue dominated emission profiles, indicating periodic evolution on a timescale of 30 years (Manser et al., 2016b). Similar evolution was later reported in the emission profiles of WD 1043+0855 (Manser et al., 2016a) and WD 0845+2257 (Wilson et al., 2015) on timescales of decades indicating this asymmetric emission profile evolution was a common occurrence. Manser et al. (2016b) used doppler tomography to demonstrate that the emission profile variations could be reproduced by the precession of a fixed intensity pattern, later confirmed by Hartmann et al. (2016), and posited the general relativistic precession of a recently formed elliptical disk could readily explain the observations. The variations observed in these systems could provide clues to the origin of the gaseous emission and regular follow-up of all eight systems is needed to track their evolution.

In chapter 3, we will discuss the design, deployment, and performance of a new fringe-surpressing camera we have integrated into the Goodman Spectrograph to enable continued follow-up on the gaseous emission profiles of the debris disks around white dwarfs. We detail our follow-up of the four remaining known systems and a search for additional emission lines among the known debris disk hosting white dwarfs. We will present the discovery of rapid variability of the emission lines around one system, HE1349–2305, which challenges the interpretation of general relativisitic precession as the variability we discovered is an order

of magnitude faster than previously seen. Finally, we discuss the origin and evolution of the gaseous debris in the context of this new discovery in chapter 4, suggesting instead that the propagation of global density waves within the disk could more readily explain the long and short emission profile variations observed.

1.3.3 Transiting Debris Around WD 1145+017

Finally, no discussion of exoplanetary debris around white dwarf stars would be complete without mention of the transiting debris around WD 1145+017 (Vanderburg et al., 2015). The asymmetric periodic dips in the Kepler Space Telescope light curves of this white dwarf were found to be consistent with the sorts large debris clumps one would expect during the tidal disruption phase, and the white dwarf star is accompanied by excess infrared radiation one would expect from a dusty debris disk (Vanderburg et al., 2015). Furthermore, high-resolution spectroscopic observations revealed the presence of both atmospheric pollution and circumstellar gas (Xu et al., 2016). It is clear that this system has been capturing undergoing the tidal disruption of a planetesimal and the formation of an accretion disk.

As expected in the tidal disruption model, follow-up studies have demonstrated significant evolution to both the transiting debris (Rappaport et al., 2016; Gänsicke et al., 2016b; Croll et al., 2017) and the circumstellar gas (Redfield et al., 2017; Cauley et al., 2018). WD 1145+017 will certainly be an important benchmark for theories of exoplanetary debris evolution of white dwarfs for many years to come, though it is not a focus of this thesis work.

1.4 Overview of Thesis Contents

In this dissertation we will try to untangle some of the mysteries of the debris disk evolution with a combination of new observations and new techniques for analyzing existing observations. This work is motivated by a desire for a complete understanding of debris disk evolution that can be used to further constrain the atmospheric accretion rates of metals at the white dwarf surface, lending knowledge to exoplanetary compositional analyses.

We begin with our efforts to discover new debris disk hosting white dwarfs in chapter 2, which includes the discovery of a dusty debris disk hosting white dwarf which appears to have accreted a differentiated body similar in composition to our Earth's crust. We follow this with the discovery of thirteen new dusty debris disk candidates and a present new discovery technique for mining for dusty debris disk candidates in large photometric samples which is ideally suited for future studies of the large number of new white dwarf stars expected to be discovered by GAIA (Gänsicke et al., 2016a). This technique involves placing all infrared excess candidates on a single observational plane for classification, which consists of the best-fitting temperature and radius of a single temperature blackbody fit to the infrared excess. New dusty debris disk candidates are quickly identified in the single temperature blackbody plane. We provide a roadmap for confirming these new candidates as bona-fide dusty debris disks which, if confirmed, have the potential to increase the known dusty debris disk sample by 25%.

In chapter 3, we discuss our observations of the gaseous emission observed in a handful of dusty debris disk hosting white dwarfs. To enable these observations, we completed a substantial upgrade to the Goodman Spectrograph to support a second camera optimized for studies at longer wavelengths, creatively named the Goodman Red Camera, which is now available to the entire US astronomical community. With this camera we discovered rapid variability in the emission profiles of the gaseous debris disk surrounding the white dwarf star HE1349–2305. The yearly variations we have discovered in this system push the limits of the existing theoretical interpretations for what could drive the emission profile variability and provide the only test-case for monitoring the stability over multiple cycles, as other similar systems take several decades to complete single variability cycles.

In chapter 4, we discuss how these observations help constrain theories of debris disk evolution. Our specific contributions include the interpretation of the dusty debris disks as elliptical rather than circular, providing an alternative explanation for fainter disks around younger white dwarfs. We also identify the gaseous emission line hosting white dwarfs as

forming the terminus of the dusty debris disks in the single temperature blackbody plane, and discuss interpretations of this boundary in terms of both single system evolution within the plane and the shared properties of the gaseous debris disk hosting white dwarfs as uncovered via population synthesis studies. Finally, we consider the theory of global density waves to explain the emission profile variations observed around white dwarf stars as an alternative to general relativisitic precession. We conclude in chapter 5 with a summary of results and and an outlook on how this work can be incorporated into or extended upon in future studies.

CHAPTER 2: Discoveries of New Dusty Debris Disk Systems [1]

Still in its infancy, the study of exoplanetary systems around white dwarf stars is readily driven by new observational discoveries. One technique for discovering new systems is to search for the excess radiation emanating from the dusty components of the exoplanetary debris disks. Starting with a list of known white dwarf targets, one can collect observations taken at various wavelengths in order to construct a spectral energy distribution (SED). White dwarf model photometry can then be compared against the spectral energy distribution to determine if there is excess infrared radiation. Several studies have employed this technique in search of new systems, but techniques for doing so in era of diverse and expansive all-sky photometric surveys are lacking.

The exoplanetary debris heated by the white dwarf typically reaches temperatures of around 1000 K, meaning it's radiation is most apparent at wavelengths longer than a few microns. Light at these wavelengths is mostly blocked by the Earth's atmosphere, so space-based observatories provide the best tools for programmatic searches of this dust. A handful of targeted studies have been carried out with the Spitzer space telescope (e.g. Kilic et al. (2006), Rocchetto et al. (2015)), but as we continue to search larger lists of white dwarf stars and the number of dust disk candidates increases, searches based on single targeted object observations quickly become infeasible. Publicly available survey telescope data provides a path forward.

The Wide-Field Infrared Survey Explorer (*WISE*) was an infrared telescope launched in 2009 with the mission to complete a photometric survey of the entire sky at wavelengths of 3, 4, 12, and 22 microns. The telescope recorded photometric measurements for hundreds of

[1]Parts of the work presented in this chapter previously appear in *The Astrophysical Journal*, see Dennihy et al. (2016) and Dennihy et al. (2017a)

millions of stars, assembling a one-of-a-kind photometric database of observations at near-infrared and infrared wavelengths. Several studies have made use of this database for studies of white dwarf stars, including the series of papers on the Wise Infrared Excesses around Degenerates (Debes et al., 2011a,b; Hoard et al., 2013) demonstrating the power of mining for new dusty debris disk candidates using survey data as opposed to targeted data, but the candidates mined come with some inherent uncertainty.

One of the main issues one must overcome when searching for excess infrared radiation around white dwarf stars using catalog photometry is the possibility of contamination by nearby sources, particularly in the *WISE* data as the spatial resolution of the *WISE* images is very coarse compared to surveys at shorter, optical wavelengths. The result is that two objects which are clearly resolved in one image may appear as a single object in a *WISE* image, resulting in an erroneous infrared excess detection. Furthermore, for studies of debris disks around white dwarfs, only the 3 and 4 micron *WISE* bands are of sufficient depth to probe for dust (Debes et al., 2011a), leaving one with 1-2 potentially contaminated data points to constrain the fits to the excess radiation.

Several different techniques can be applied to circumvent this issue, including re-examination of the photometry in question and careful modeling of the infrared excess to rule out contaminating sources. We can also search for signs of active accretion in the white dwarf atmosphere which independently suggest the presence of a compact accretion disk, but with the caveat that several white dwarf stars are known to shown active signs of accretion without an infrared bright debris disk, so it is not sufficient to prove an infrared excess is necessarily due to a dust disk. All of these techniques were combined and utilized in our first discovery of a new debris disk hosting white dwarf around the white dwarf star EC 05365–4749.

2.1 EC 05365–4749: the initial discovery

2.1.1 Target Selection and Observations

In order to carry out a survey mining program, one must first collect a sample of white dwarf stars and their on-sky coordinates. For example, previous WIRED surveys used the white dwarf stars detected in the SDSS photometric catalog (Debes et al., 2011b) and the McCook and Sion white dwarf catalog (Hoard et al., 2013). For our sample of white dwarf stars, we chose the objects identified as white dwarf stars in the Edinburgh-Cape Blue Object survey (hereafter EC survey) (Kilkenny et al., 1997; O'Donoghue et al., 2013). This survey was released in stages and so our initial search only included objects identified in Zones 1 and 2 of the survey. We later extend this search to include the entire EC Survey in section 2.2.

Of the approximately 110 targets we surveyed in the first two zones, two were identified as strong infrared excess candidates: EC 05365–4749, the focus of this section, and WD 1150–153, a previously known dusty white dwarf (Kilic & Redfield, 2007). These numbers are roughly consistent with recent estimates of the frequency of dust disks around white dwarfs (Debes et al., 2011a; Barber et al., 2014; Rocchetto et al., 2015).

2.1.2 Collected Photometry

We collected published photometric measurements of EC 05365–4749 from the 2 Micron All-Sky Survey Point Source Catalog (2MASS; Cutri et al. (2003)), the AllWISE photometric catalog (Cutri & et al., 2013), the AAVSO Photometric All Sky Survey (APASS; Henden et al. (2009)), the Galaxy Evolution Explorer telescope (*GALEX*; Martin et al. (2005)) Data Release 6, and the VISTA Hemisphere Survey 3rd data release (VHS; McMahon et al. (2013)), enabling the construction of a spectral energy distribution spanning ultraviolet to near-infrared wavelengths. We also collected near-infrared images for astrometric information from the VISTA Science Archive, described in Irwin et al. (2004), Hambly et al. (2008), and Cross et al. (2012).

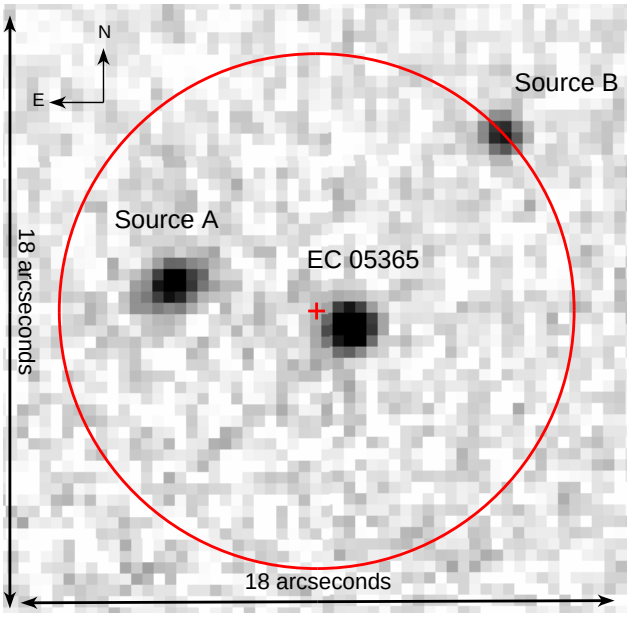

Figure 2.1: Infrared K_s image taken from the VISTA VHS Survey DR3. EC 05365–4749 is identified at $5^{h}37^{m}53.5^{s}$, -47°58′05.3″ in FK5 coordinates along with a nearby sources 'A' and 'B'. A 7.8 arcsecond circle is shown centered on the red cross which identifies the AllWISE detection photocenter.

As discussed in Debes et al. (2011a), the large point-spread function of the *WISE* telescope often leads to contamination or source confusion. High spatial resolution follow-up images are necessary for identifying nearby contaminants. The *WISE* photometry system implements profile fit photometry and source deblending routines that are robust against contamination of resolved sources separated by more than 1.3 time the full-width half-max (FWHM) of the of the point-spread function of the band of interest (approx. 7.8 arcseconds for *W1*), and it is capable of flagging sources contaminated by a nearby unresolved source by virtue of the goodness of fit of the best fit point-spread profile. The use of these deblending routines in the photometric measurement of a source is captured in a set of photometric flags; 'nb' for the passive deblending routine of resolved sources separated by more than 1.3×FWHM of the point-spread function of the band, and 'na' for the active deblending of a pair of unresolved sources. For the photometry taken at the source position associated with EC 05365–4749, the source was not flagged for active profile deblending, indicating that the reported photometry is not corrected for contamination for a nearby source within 7.8

Object	J (mag)	σ_J	K_s (mag)	σ_{K_s}	Sep (")
EC 05365	16.099	0.010	16.114	0.038	1.12
Source A	17.869	0.041	16.615	0.057	4.46
Source B	17.796	0.036	17.469	0.128	7.73

Table 2.1: VISTA VHS Photometry for EC 05365–4749 and potential contaminating sources.

arcseconds.

Figure 2.1 displays the VISTA VHS K_s band image which allowed us to identify two potential nearby contaminants to our targetwhich we label Source A and Source B. The red circle indicates the limit of source resolution implemented by the AllWISE photometry pipeline prior to attempting blended profile fit photometry. The VISTA J and K_s band measurements and approximate separation from the AllWISE detection photocenter for each source are given in Table 2.1. Source B is just at the limit of resolution. Given the relatively faint K_s magnitude and J - K_s color, we suspect it is below the detection limit of the *WISE* bands and not a source of contamination for the ALLWISE detection. Source A however is comparable in K_s brightness and has a J-K_s color indicating it could have a measurable flux in the *WISE* 1 and 2 bands. Source A is also extended and has a high probability of being extra-galactic. Considering only the information contained in the AllWISE catalog, we have no way of determining if the AllWISE measurement represents a blend of EC 05365–4749 and Source A, or if it is instead consistent with a single source at either the position of the target or Source A. However, since we know the positions of the target and Source A very well from the VISTA catalog (compared to the course sampling of the *WISE* pixel scale), we can perform a set of estimations to determine the potential for *WISE* contamination. We discuss this potential for contamination in detail in the context of our spectral energy distribution in subsection 2.1.5.

2.1.3 Spectroscopic Follow-up

Though photometry alone is often sufficient to identify a dusty debris disk around a white dwarf, spectroscopic follow-up can be used for identifying and characterizing the atmospheric

pollutants that indirectly probe the remnant planetary system. As part of our spectroscopic follow-up of EC 05365–4749, we first observed the target with the Goodman Spectrograph (Clemens et al., 2004) on the SOAR telescope configured to search for atmospheric metal pollution on 2015 April 04. The 0.46" long slit and 1800 l/mm grating were chosen to maximize spectral resolution (≈ 0.66 Å per resolution element) while allowing the spectral range to probe for the Ca II H & K transitions at 3934 Å and 3967 Å, and the Mg II doublet at 4481 Å. We achieved a signal-to-noise per resolution element of 27 near 4000 Å in 3240s of combined exposure time. The data revealed an absorption feature at the approximate location of the Mg II doublet with an equivalent width of 75 ± 16 mÅ, though without a published radial velocity or suitable comparison line we could not rule out the possibility that the feature was from the absorption of interstellar gas along our line-of-sight.

To confirm the detection of Magnesium and search for additional metal species, we observed EC 05365–4749 with the MIKE spectrograph (Bernstein et al., 2003) on the Magellan telescope on 2015 April 30. We used the 0.5"×5" slit which translated to a resolution of 0.083 Å per resolution element and a signal-to-noise per resolution element of 25 near 4000 Å in the combined 3×1200 s exposures. The data were extracted and flatfielded using the MIKE reduction pipeline, with methodology described in Kelson et al. (2000) and Kelson (2003). Using the reduced spectra we confirmed the detection of Mg with a measured equivalent width of 83 ± 6 mÅ and discovered a Ca K absorption feature with an equivalent width of 47 ± 11 mÅ. Both the Ca and Mg absorption features were found to be at the photospheric velocity as calibrated against the core of the hydrogen alpha absorption line. After applying heliocentric velocity corrections we found the photospheric velocity of the white dwarf star (combined gravitational redshift and radial velocity) to be $40 \pm 7\,\mathrm{km\,s^{-1}}$.

To better constrain the fundamental parameters of the white dwarf star such as the effective temperature and surface gravity, we observed EC 05365–4749 with the Goodman Spectrograph on 2015 May 21 with a low resolution setup. The spectrograph was configured with the 930 l/mm grating and the wide 3.0" long slit to minimize the effect of variable

seeing conditions which were measured to be between 1.4-1.6". The seeing limited resolution was approximately 4.2 Å per resolution element with a wavelength range of 3700 to 5200 angstroms and we achieved a signal-to-noise of 110 per resolution element near 4200 Å in the combined 7×180 s exposures. We reduced and extracted the spectra with standard IRAF techniques and employed user developed techniques for wavelength and continuum calibration. The spectroscopic standard LTT 2415 was observed to provide continuum calibration.

2.1.4 Atmospheric Modeling

Though the atmospheric parameters of white dwarfs can be constrained with photometric data (Bergeron et al., 1995), the surface temperature implied by our photometry is poorly constrained (21 000-26 000 K), which is often the case for stars this hot. We instead rely on the spectral line fitting technique initially developed by Bergeron et al. (1992) and refined by Bergeron et al. (1995); Liebert et al. (2005). The method uses a grid of model spectra over a range of surface gravities ($\log g$; g measured in cm s^{-2}) and effective surface temperatures ($T_{\rm eff}$; K). A Levenberg-Marquardt chi-squared minimization is then used to determine which values of $\log g$ and $T_{\rm eff}$ best reproduce the Balmer profiles relative to their local continuum. By using only the shape and depth of the Balmer profiles, this method is expected to be robust against overall flux calibration errors.

We first obtained atmospheric parameters using the low resolution Goodman data and the corresponding spectrophotometric standard data for flux calibration. The best-fit $\log g$ and $T_{\rm eff}$ were 8.03 ± 0.05 and 24,050 ± 150 K respectively, with the error bars representing the statistical uncertainties of the fitting process. As expected, the individual Balmer profiles were reproduced well by the model atmosphere but the continuum shape between lines was poorly fitted. Given the cloudy conditions of the night, we suspected the data used for flux calibration to be unreliable.

To asses the reliability of the standard flux calibration, we generated a comparison set of spectra which were flux calibrated with an independent set of white dwarf model spectra,

kindly provided by D. Koester (see Koester (2010) for details on model input physics and methods). We chose models spanning the photometrically constrained temperature range and only used continuum points for calibration to avoid biasing the fits to the Balmer profiles. When fitting the model flux calibrated spectra of EC 05365–4749 we found the best fitting $\log g$ and $T_{\rm eff}$ to be 8.20 ± 0.05 and 22,800 ± 150 K independent of the white dwarf model used for flux calibration. The agreement of the model flux calibrated solutions further supports our suspicion of the standard flux calibrated data. We therefore adopt $T_{\rm eff} = 22,800^{+1400}_{-150}$ K and $\log g = 8.19^{+0.05}_{-0.20}$ for the remainder of the analysis, incorporating the solutions from our standard flux calibrated data into our reported uncertainty. Figure 2.2 shows the Balmer series fits to the model calibrated Goodman data. Using the evolutionary sequences of Fontaine et al. (2001), the surface gravity and temperature are consistent with a white dwarf mass and cooling age of $0.74^{+.03}_{-.12}\,M_\odot$ of 63^{+7}_{-36} Myr.

2.1.5 Establishing the Infrared Excess

To establish and model the infrared excess, we first converted all measured photometry to units of flux density using published zero points (Wright et al., 2010; Skrutskie et al., 2006; Holberg & Bergeron, 2006). We scaled the white dwarf model to the observed photometry by calculating a median scale factor for all photometry points without clear excess ($\leq 2.15\,\mu$m). The scaling factor is consistent with a photometric distance of 87^{+13}_{-3} parsecs. The resulting scaled white dwarf model is plotted with the observed photometry in Figure 2.3.

The departure of the *W1* and *W2* photometry from the white dwarf model of EC 05365–4749 is evidence for an additional infrared bright source. But before we can attribute it to a source coincident with EC 05365–4749 we must consider the contribution to the *W1* and *W2* measurement of the nearby extra-galactic Source A. There were no photometric flags of the EC 05365–4749 data in the AllWISE database indicating profile deblending was not performed for this detection, and any contributions from Source A are included in the catalog measurements at *W1* and *W2*.

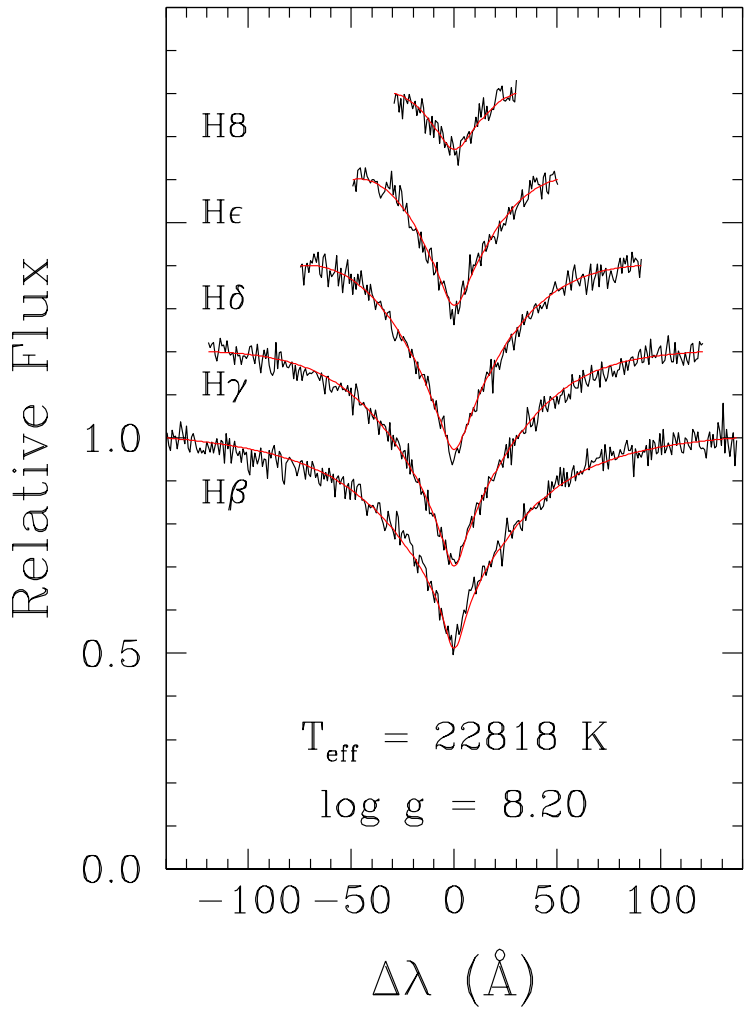

Figure 2.2: Normalized hydrogen Balmer absorption lines of spectroscopic data taken with SOAR with best fitted $\log g$ and $T_{\rm eff}$ model overplotted in red. The two parameters are used to constrain both the SED and the atmospheric diffusion times necessary for exoplanetary abundance analyses.

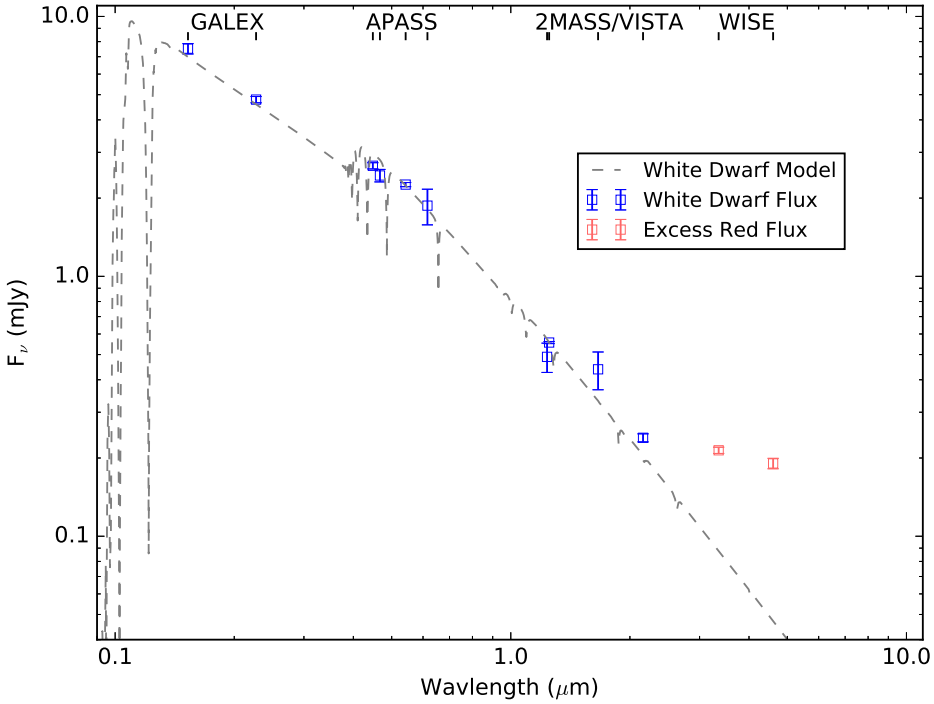

Figure 2.3: EC 05365–4749 observed photometry in blue overplotted with white dwarf model shown in light grey. The VISTA photometry for Source A and the spatially coincident AllWISE photometry are plotted separately in red and green. Note that the errors presented are catalog uncertainties and likely underestimate the absolute (including systematic) photometric uncertainty.

We are unable to model the expected contribution of the galaxy to *W1* and *W2* bands as it is only detected in the two VISTA bands and we cannot constrain both the galactic spectral type and redshift. As a rough test, we used the galaxy SED atlas of (Brown et al., 2014) to determine whether any nearby galaxy SEDs could match the observed *J*-*Ks* colors and reproduce the entire *W1* and *W2* excess. The atlas constitutes a large set of observed SEDs of nearby ($z < 0.05$) galaxies spanning a wide range of morphological types. Few of the observed catalog SEDs are able to reproduce the observed slope from *J* to *Ks* and none of them are likewise consistent with the *W1* and *W2* excess. We are confident this rules out the possibility of a nearby galaxy accounting for the excess, but cannot rule a higher redshift source.

A by-eye extrapolation of the flux from Source A in Figure 2.3 might suggest a very strong contribution to the *W1* and *W2* measurements, but the spectral energy distribution does not consider all of the information available, namely the relative separations of the AllWISE photocenter from the measured positions of EC 05365–4749 and Source A in the VISTA VHS catalog. Based on the additional astrometric evidence, we now argue that even if there is contamination from Source A in the *W1* and *W2* measurements, there is still a significant infrared excess associated with EC 05365–4749.

In Figure 2.4 we show the VISTA K_s and the WISE *W1* band image, each overplotted with isoflux contours of the *W1* image. It is immediately apparent that the contours of the *WISE* detection are more consistent with a source detection at the position of the target EC 05365–4749, with a minor asymmetry and offset in the direction of Source A suggesting some measureable contamination. As a first-order estimate of the level of contamination, we can use the relative separations of the target and Source A from the *WISE* photocenter as a rough proxy of their relative flux. Assuming the positions of the target and Source A as reported by the VISTA Science Archive and considering the source position of the AllWISE detection and its associated error ellipse, we find the ratio of the flux of the target to the flux of Source A within the *WISE* bands to be $4.0/1.0 \pm 0.6$. If we subtract this level of

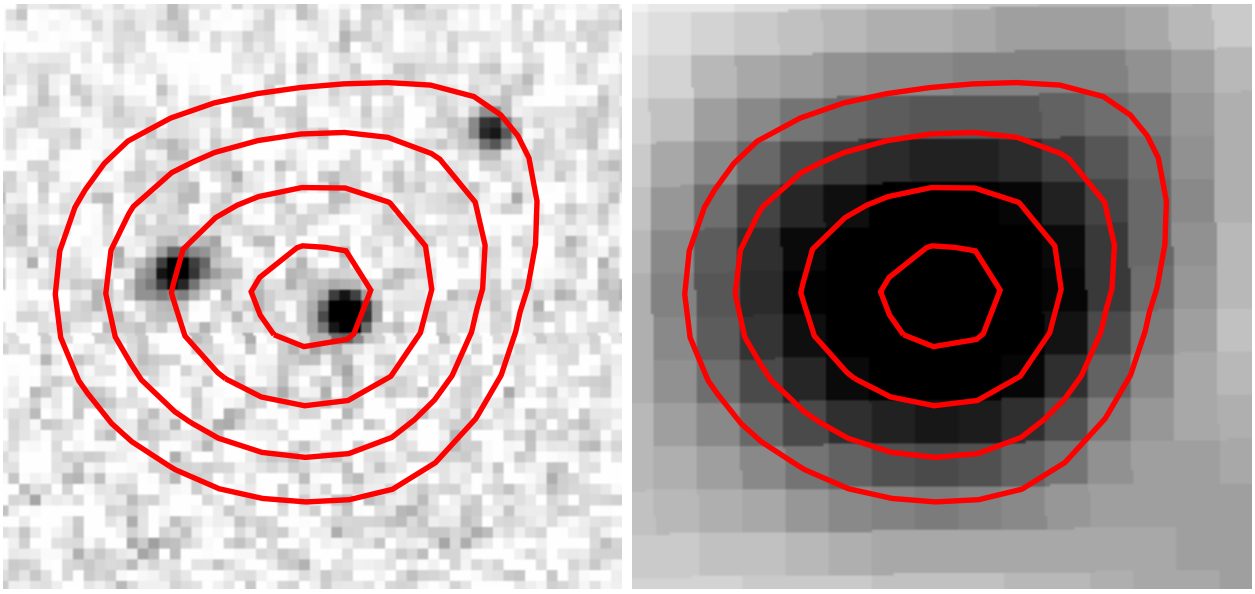

Figure 2.4: Left: Vista K_s image with *W1* isoflux contours overlaid. Right: *WISE* W1 image with isoflux contours. The images are 18 x 20 arcseconds to match the scale of Figure 1. Both the minor asymmetry of the contours along the line between EC 05365–4749 and Source A and the offset in the AllWISE photocenter from the position of EC 05365–4749 suggest potential for source confusion.

contribution of Source A from the AllWISE flux measurements (approx. 20%) we still find an excess above the white dwarf model in the *W1* and *W2* bands of $13\,\sigma$ and $12\,\sigma$, assuming the reported photometric errors. Given the significance of the excess, we do not expect any systematic error introduced by assuming the reported photometric errors to invalidate the excess.

As a more informative approach, we followed the technique of 'forced' photometry of Lang et al. (2016). The technique relies on forward modeling of the *WISE* catalog images by taking the positions of sources, the point-spread function of the band of interest, and a per pixel noise model a known-quantities and solving for the most likely combination of source fluxes that can reproduce the observed *WISE* images (Lang et al., 2016).

For our images we used the unWISE coadds produced by Lang (2014), which are a publicly available set of *WISE* co-added images sampled at the nominal resolution of the detector and optimally combined for the purpose of forced photometry. As our point-spread functions for each *WISE* band, we used a combination of gaussian functions as derived in

Lang et al. (2016) with weight and standard deviation given in their Table 1. As an estimate of the local noise we chose three neighboring regions that are source free in the VISTA J and K_s images, and in the unWISE coadded images. Since we are only concerned with the relative flux of two sources, we proceed by generating a grid of fluxes for each source. At each point on the grid we convolve the fluxes at their source position with the point-spread function of the band of interest, sampled at the resolution of the image, and subtract the result from the unWISE image. We then compared the resulting subtracted image with the local noise estimates using the method of least squares to find the most probable combination of fluxes. We performed this exercise separately on the *W1* and *W2* images.

As expected, the result of the forced photometry measurement varies between *W1* and *W2*. For the *W1* band, a target to Source A flux ratio of 2.0/1.0 best reproduced the image. Whereas for the *W2* band, the best fitting target to Source A flux ratio was 3.39/1.0. Assuming that Source A contributes these fractional fluxes to the AllWISE detection, if we again subtract the contribution from Source A to the *W1* and *W2* measurements we find the remaining flux above the white dwarf model to represent $8\,\sigma$ and $11\,\sigma$ excesses respectively, securing the excess of infrared radiation around EC 05365–4749.

2.1.6 Modeling the Infrared Excess

We proceed by exploring different astrophysical models that can reproduce the infrared excess associated with EC 05365–4749, in each case considering a minimally (using the results from astrometry alone) and maximally (using the results from the forced photometry) contaminated flux measurement for the *W1* and *W2* bands. For the remainder of the section we will refer to these results as Case 1 and Case 2 levels of contamination.

The simplest model we explored was a spherical blackbody source taken to be at the photometric distance of the white dwarf, e.g. an unresolved low mass companion. Using a minimum chi-square fitting method, we determined the best fitting temperature and radius for the Case1 and Case 2 contamination levels to be 1040 K, 0.15 $R_\odot$ and 800 K, 0.23 $R_\odot$

Fixed i (deg)	T_{inner} (K)	T_{outer} (K)	R_{inner} ($R_\star$)	R_{outer} ($R_\star$)
Case 1 Contamination:				
45	1100	1030	34	37
80	1150	860	32	47
Case 2 Contamination:				
45	860	800	47	52
80	920	650	43	68

Table 2.2: Best-fitted circular dust disk parameters for the infrared excess around EC 05365–4749.

respectively. The temperatures are consistent with the T dwarf sub-stellar class but the radii are implausibly large. In addition, the J-K_s color provided by both 2MASS (J–K_s < 0.556) and VISTA (J–K_s = –0.28) rule out a companion of this spectral class (Chabrier et al., 2000).

By dividing the bolometric flux of these single temperature blackbody solutions with the bolometric flux of the model white dwarf, we can also get an estimate for the fractional infrared luminosity $\tau = L_{\rm IR}/L_\star$ of the system. Such a metric has been demonstrated by Farihi (2011) and Rocchetto et al. (2015) to point towards aggregate properties of the debris discs around white dwarfs. The different levels of contamination result in a range of $\tau = 0.066$-$-\,0.080\,\%$, adding EC 05365–4749 to the growing sample of subtle infrared excesses around young white dwarfs.

We also modeled the infrared excess with a flat, optically thick circular disk using the formalism developed by Jura (2003). As discussed in subsection 1.3.1, the model invokes a radially dependent temperature distribution and can be used to constrain the inclination, inner, and outer radius of the disk. There is however an unavoidable degeneracy between inclination and the width of the disk, which is amplified in the absence of longer wavelength data. Having only two mid-infrared data points with clear excess, we fixed the inclination and explored only the inner and outer radius of the disk. Considering the degeneracy between width and inclination, we fitted the models under assumptions of both high ($i = 80$ deg) and low ($i = 45$ deg) inclination, and present both as viable solutions.

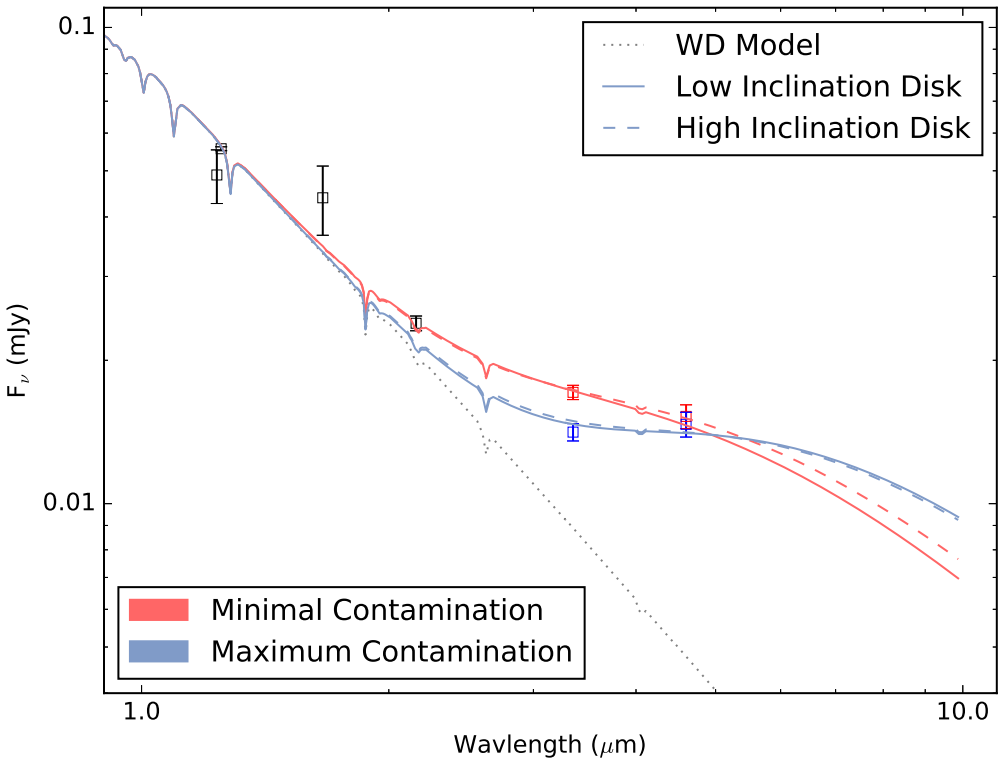

Figure 2.5: Best-fitted circular disk models overplotted on measured infrared photometry and white dwarf model. The minimally contaminated solutions are shown in red while the maximally contaminated solutions are in blue. The solid/dashed lines represent low/high inclination solutions.

We used a minimum chi-squared fitting procedure to determine the best fit inner radius and disk width. We parameterized the inner radius in terms of its temperature and explored a range of inner temperatures from 500 to 2500 K and a range of disk widths from 1-20 stellar radii. The results from considering both the Case 1 and Case 2 contaminated *W1* and *W2* measurements are summarized in Table 2.2. We overplot the best fitted combined spectral energy distributions of the white dwarf and the dust disks on the observed photometry for Case 1 and Case 2 contamination in Figure 2.5.

The range of parameters that can fit the data is large, but qualitatively the subtle excess forces the circular disk models to two classes of solutions: a wide disk observed at high inclination or a narrow disk observed at low inclination. With no prior expectation for the

inclination, there is no preference for either class of solutions. The subtle excess associated with EC 05365–4749 is so far typical of dusty white dwarfs with cooling ages below 200 Myr, as recently explored by Rocchetto et al. (2015). The tendency towards narrow disks (which do not span the available space between the sublimation radius and tidal disruption radius) is less apparent for older dusty white dwarfs with cooling ages between 200 and 700 Myr, presenting an interesting delineation between the two samples. We discuss an alternative to this interpretation using and elliptical model for the dust distribution and its application to EC 05365–4749 in section 4.1.

2.1.7 Atmospheric Accretion and Exoplanetary Abundance Measurements

We followed the procedures detailed in Dufour et al. (2010) to estimate the atmospheric abundance of Ca and Mg. In short, assuming the atmospheric parameters above, we generated model white dwarf atmospheres using the codes developed by Dufour et al. (2007) and performed a chi-squared minimization over a grid of atmospheric abundances for each element detected. We find the atmospheric metal pollution to be consistent with logarithmic abundances of [Mg/H] = –5.36 ± 0.25 and [Ca/H] = –5.75 ± 0.25. Figure 2.6 shows the best fit profile to the Mg 4481 Å doublet.

The observed atmospheric abundances can be transformed into estimates of the accretion rate with knowledge of the rates of diffusion for each element. Using the atmospheric parameters derived in subsection 2.1.4 and the updated diffusion calculations described in Koester (2009)[2], we determined the diffusion timescales for Ca and Mg to be 2.75×10^{-3} and 4.47×10^{-3} years respectively. The atmospheric calculations of Koester (2009) also include an estimate of the hydrogen mass necessary to translate the observed photospheric number densities into mass densities for the accretion rates of each species. Assuming the hydrogen mass to an optical depth of $\tau = 2/3$ is 1.73×10^{-17} $M_{\odot}$, we find the system to be accreting Ca at a rate of 3.8×10^{7} $g\,s^{-1}$ and Mg at rate of 2.6×10^{7} $g\,s^{-1}$. We did not include the

[2]See updated tables here: http://www1.astrophysik.uni-kiel.de/ koester/astrophysics/astrophysics.html

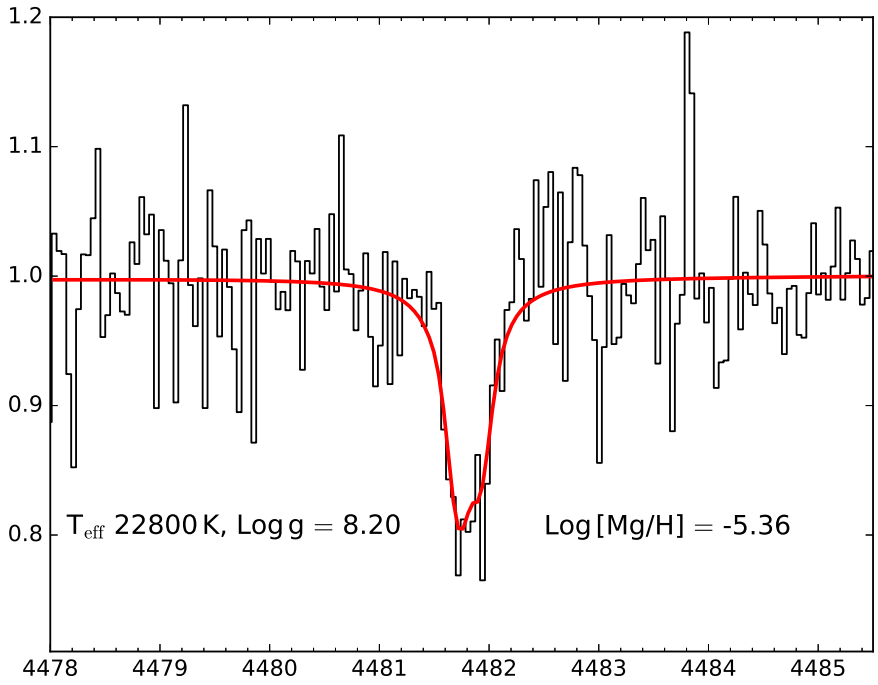

Figure 2.6: Magellan/Mike data overplotted with the atmospheric abundance model around Mg II 4481 Å. The red line is the best fit model with a logarithmic abundance of [Mg/H] = –5.36.

effects of radiative levitation on the observed abundance and inferred accretion rate as they are are less important for lighter elements such as Ca and Mg, and negligible for accretion rates as high as observed (Chayer & Dupuis, 2010).

The most exciting feature of exoplanetary studies using white dwarf stars is the opportunity to translate the observed accretion rates into the abundances of the accreted parent body, thereby probing rocky exoplanetary abundances not accessible to other direct methods. The observed abundances depend on the rates of accretion, diffusion, and critically the understanding of the current accretion phase as either in a build-up phase, a steady-state phase, or a declining phase. As discussed in Koester (2009), the rate of diffusion sets the relevant timescale ($\tau_{\rm diff}$) for the accretion phase and it is reasonable to expect the atmospheric abundances have reached a steady state as long as the accretion has been held constant for $> 5\,\tau_{\rm diff}$. In the case of EC 05365–4749, the diffusion timescales for both Ca and Mg are on the order of days, guaranteeing that accretion has proceeded for several times the diffusion time. Therefore, we can be certain the atmospheric abundance has reached a

steady state and, to within the ratios of the diffusion timescales, the observed atmospheric abundance ratios directly reflect that of the accreted parent body. Including the ratio of the diffusion timescales derived above we calculate the abundance ratio of the accreted body as $[\mathrm{Mg/Ca}] = +0.24 \pm 0.25$.

Because these two elements have strong transitions in the optical, the [Mg/Ca] ratio has been studied for a large sample of polluted white dwarfs (see the recent assessment Jura & Xu (2013)[3] in particular their Figure 1). Despite some dispersion, it is clear that the ensemble abundance ratio reflects bulk earth composition, but the abundance ratio for EC 05365–4749 represents a large departure from mean of this sample.

One possibility for this departure could be the accretion of some refractory dominated material, such as the crust of a larger, differentiated body. Such a scenario is discussed by Jura et al. (2015), and the spread in abundances ratios of well-studied polluted white dwarfs is further evidence for the post-nebular processing of extrasolar asteroids. The closest analog to EC 05365–4749 is GD 362, which Xu et al. (2013) demonstrated must have accreted from either multiple distinct sources, or some material that underwent post-nebular processing. A detailed abundance study will be necessary to confirm whether EC 05365–4749 is indeed accreting from such a unique source. Since the publication of this work, EC 05365–4749 has been targeted by the Hubble Space Telescope by an external group to perform such a study, and the results are pending.

2.2 ECxWIRED: the survey

Having honed our techniques for dusty debris discovery on EC 05365–4749, we then extended our search to include the complete list of white dwarf stars identified in the EC

[3]Jura & Xu (2013) use the instantaneous accretion approximation (also described as the early phase approximation as it does not account for differences in elemental diffusion timescales) for the sample in their Figure 1. Under this assumption $\log[\mathrm{Mg/Ca}] = +0.39$ for EC 05365.

Survey. As expected, we were again faced with significant contamination and source confusion issues. Given the much larger sample of white dwarf stars, we did not have the resources to dedicate as much time to establishing the validity of the infrared excess of each candidate as we did in the prior section. Furthermore, the quality of photometric data varied wildly between each candidate, an issue that is certain to plague future all-sky searches for dusty debris disk hosting white dwarfs, specfically studies of the hundreds of thousands of new white dwarf stars expected to be discovered by the GAIA satellite in 2018 (Gänsicke et al., 2016a).

To overcome these challenges, we developed a new technique for classifying infrared excess sources based only on the parameters derived from a single temperature blackbody model fit of the infrared excess. This technique allowed us to quickly classify infrared excesses as either dusty, stellar, or other, and even helped us identify a published dusty debris disk as a likely case of line-of-sight contamination masquerading as dust. We discuss the EC Survey sample, the new single temperature blackbody selection technique, and the results in this section.

2.2.1 Target Selection and Collected Photometry

Of the 2,637 unique hot objects identified in the completed EC survey, we find that 489 have been designated as hydrogen atmosphere white dwarf stars with type DA or possible type DA (e.g. DA?, DAweak, etc.). Candidates that have an uncertain but possible DA spectral type are also included in this study and are discussed later in the context of possible mis-classifications. For each target, we extract additional photometry from the *GALEX* All-sky Imaging Survey GR5 (Bianchi et al., 2014), the APASS DR9 (Henden et al., 2016), the 2MASS PSC (Cutri et al., 2003), the VHS catalog (McMahon et al., 2013), and the AllWISE catalog (Wright et al., 2010). Data collection for the EC Survey began in the 1980s and some of the other catalogs used are still collecting data so in order to minimize source mis-identification while cross-matching our targets across nearly three decades worth

of surveys, we also collected proper motions for our targets from the PPMXL catalog (Roeser et al., 2010). Using the J2000 epoch from PPMXL, we queried each photometric catalog for sources within 2.5" of the proper motion corrected target position, corrected to the mid-point of each survey's data collection period.

To ensure we have selected the correct PPMXL source, we use a method similar to that described in Gentile Fusillo et al. (2017), which selects all nearby sources from the proper motion catalog of choice, then corrects their positions to the known epoch of the target before automatically selecting the nearest source. Unfortunately, the later releases of the EC Survey are increasingly lacking in epochs for each object coordinates, so the procedure was modified to enable user selected sources. To do this, we overlaid the J2000 corrected EC target coordinates and proper motion projections of all PPMXL sources within 15" on POSS2 imaging plates (Reid et al., 1991). This search returned 3 or less PPMXL sources for 468/489 candidates with many having only a single nearby source, leading to simple, unique source identifications based on proximity to the target coordinates. 4/489 targets had no PPMXL sources within 15". For the remaining 17/489 targets where multiple sources were found near the target coordinates, we selected the PPMXL source most consistent with both the EC Survey position and the measured EC Survey B magnitude. These results suggest that up 5% of our candidates could be mis-identified, potentially leading to spurious infrared excess selections or classifications.

To identify targets with potentially contaminated *WISE* photometry, we collected cutouts of survey images from the VISTA-VHS and VST-ATLAS (Shanks et al., 2015) catalogs in K_s and z bands from the VISTA Science Archive. When both images were available, the VHS K_s images were preferred as the photometric band is much closer to the *WISE*photometry. Examples of images from each catalog are shown in Figure 2.7. Overplotted on each image is the position of the white dwarf target as identified in the EC Survey, and the position of the corresponding AllWISE detection, including a 7.8" circle around the *WISE*position, which is the approximate limit of the automatic deblending routine used for the AllWISE

pipeline. The imaging circle allowed us to quickly identify and flag targets with potentially contaminated *WISE* photometry. Each target was assigned an image quality flag based on the results of studying the collected images by eye, which is included in the object tables in appendix A. Targets that were identified as having potentially contaminated *WISE* photometry were not excluded and should not be ruled out without more careful analysis of the contaminating source, but their *WISE* excess should be given more scrutiny than those with clean images.

2.2.2 White Dwarf Model Fitting and Infrared Excess Identification

The first step in identifying systems with an infrared excess is fitting the collected photometry of each target with a white dwarf model. We use a grid of hydrogen atmosphere white dwarf models, kindly extended to include *GALEX* and *WISE* photometry by P. Bergeron (Bergeron et al., 1995). To ensure the model and collected photometry were on the same magnitude scale, we applied zero-point offsets to the *GALEX*, EC Survey, APASS, 2MASS, and VHS magnitudes[4] as defined in Holberg & Bergeron (2006) and Camarota & Holberg (2014). Each transformed magnitude was then converted to flux density units using published zero points (Cohen et al., 2003a,b; Jarrett et al., 2011). Our photometric uncertainties are derived from reported catalog values, and we assume a 5% relative flux uncertainty floor.

Compared with previous WIRED surveys, our sample has a few unique features; first, our targets do not have a consistent set of optical measurements which are needed to anchor the white dwarf model photometry. The U, B, and V band photometry from the EC Survey is incomplete and the APASS survey is ongoing, leading to sporadic coverage across the different photometric bands. The second is that fewer than half of our white dwarfs have a prior spectroscopic effective temperature and surface gravity determination, the latter of which is often necessary to split the degeneracy between the solid angle subtended by the

[4]VHS magnitudes were transformed to the 2MASS system using the color-color equations described at http://casu.ast.cam.ac.uk/surveys-projects/vista/technical/photometric-properties

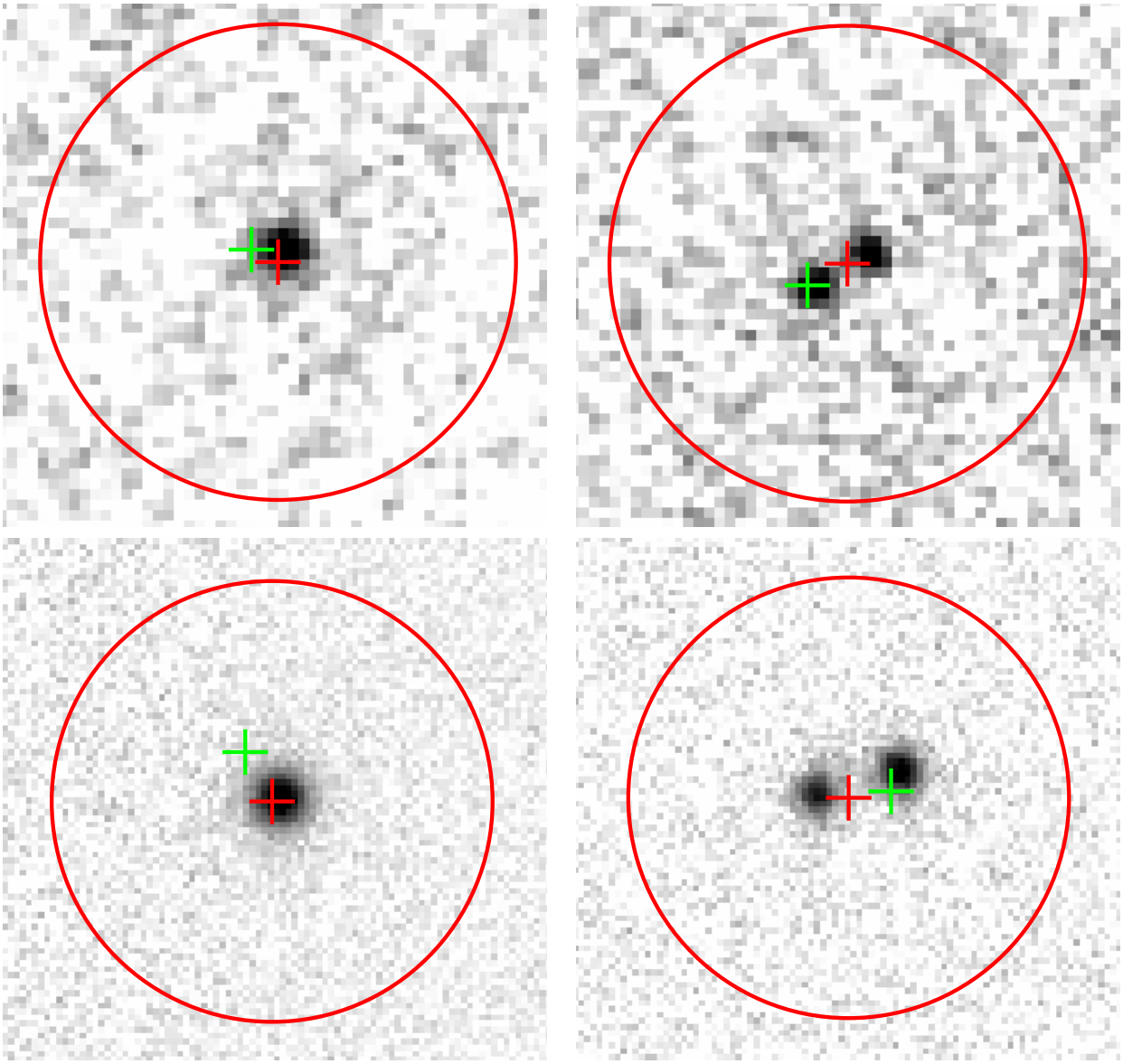

Figure 2.7: Examples of survey images examined for nearby contaminants and the image quality flags they received, North up, East right. The green and red crosses show the EC coordinates (not corrected for proper motion) and AllWISE detection centers. The 7.8" radius red circle represents the limit of the AllWISE automatic source deblending routines which is capable of resolving sources at separations greater than 1.3×FWHM of the *W1* beam. Targets with additional sources within this circle are flagged as having potentially contaminated *WISE* photometry. From left to right: Vista VHS K_s band images showing (a) EC 05267-4305 clean image, Im Flag: 00 (b) EC 05024-5705 potentially contaminated *WISE* photometry, Im Flag: 01 and pair of VST ATLAS z images showing (c) EC 21335-3637 clean image, Im Flag: 10 (d) EC 01107-1617 potentially contaminated *WISE* photometry, Im Flag: 11

white dwarf and its photometric distance.

To address these issues, for our photometric white dwarf model fits we fixed the surface gravity of our model atmosphere grid to $\log g = 8.0$. For each model in our grid, we determine an initial flux scaling based only on the available optical data ($0.4\mu\mathrm{m} \leq \lambda \leq 0.7\mu\mathrm{m}$). The photometric scale factors were then transformed to initial distance estimates, and following the prescription of Harris et al. (2006), we apply photometric reddening corrections to our photometry for all sources beyond 100pc. The white dwarf model was then re-fit to the corrected photometry. The best-fitted model was chosen by minimizing the chi-square metric as computed for each scaled model using all photometry at wavelengths below 1.0 μm. As discussed in section 2.2.3, for white dwarfs identified with strong stellar excesses that obviously extended into the near-infrared and optical, we limited the photometry used to determine the best-fit to wavelengths below 0.5 μm. For those targets with prior spectroscopic $\log g$ and $\mathrm{T_{eff}}$ solutions from either Koester et al. (2009) or Gianninas et al. (2011), we assumed the spectroscopic $\log g$ and $\mathrm{T_{eff}}$ for our white dwarf atmospheric parameters, and generated model photometry scaled to the observed, de-reddened photometry with the method described above.

We compare our photometrically derived effective temperatures to the spectroscopic determinations for apparently single objects where we have both in Figure 2.8, with the spectroscopic surface gravity displayed as a colorscale. The most egregious outliers on Figure 2.8, shown as open symbols, are cases where fewer than three photometric points were available to constrain the photometric fit. We note that none of our new infrared excess candidates suffered from this severe lack of data. Using the scatter in the relationship, we can establish uncertainties for our white dwarfs which only have photometric fits. Below 15,000 K, the fits are generally good, with an uncertainty of $\approx$1000 K. Between 15,000–30,000 K, the scatter is greater, resulting in an uncertainty of $\approx$3000 K. Above 30,000 K, the photometric fits are generally unreliable which reflects a lack of short wavelength optical and ultra-violet photometry needed to constrain the bluer SEDs. Despite the agreement below 30,000 K,

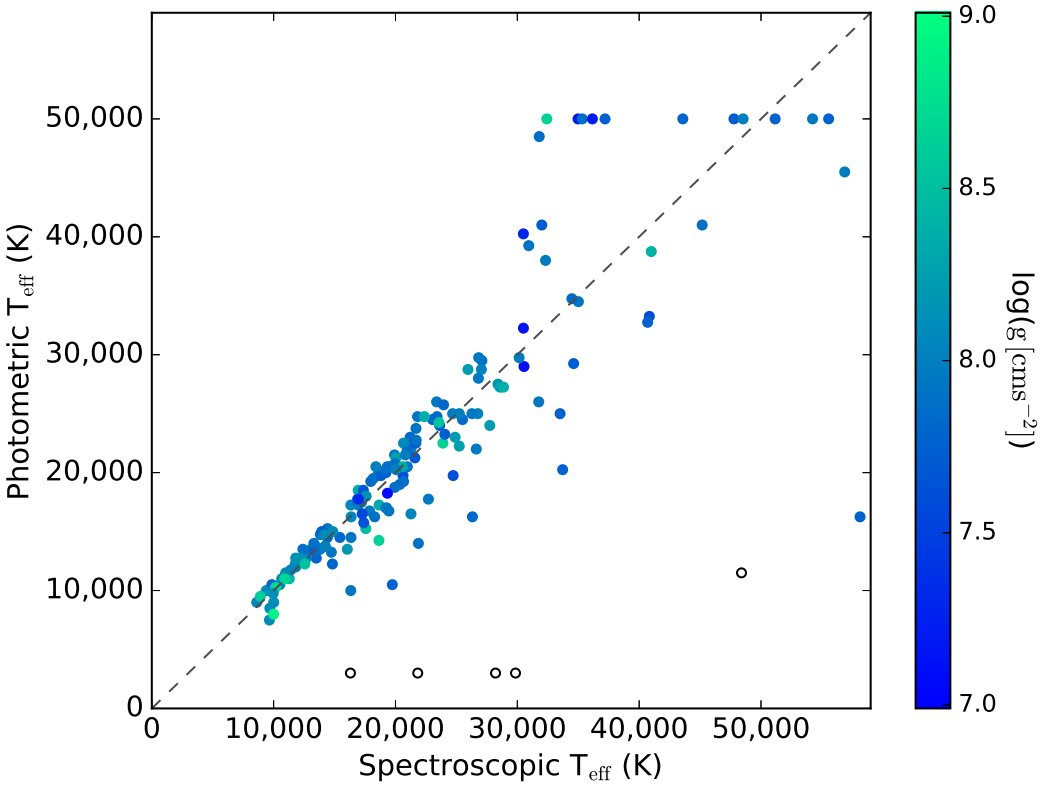

Figure 2.8: Our photometric white dwarf temperatures assuming $\log g$=8.0 compared with spectroscopic fits from Koester et al. (2009) and Gianninas et al. (2011). Open symbols represent targets with less than 3 datapoints used to constrain the photometric fit. The colorscale represents the spectroscopic surface gravity. A handful of white dwarfs can be seen hitting the top of our photometric grid at 50,000 K.

there are still a handful of 3σ outliers given the uncertainties above, all of which exhibit a bias toward lower photometric temperatures. We find the culprit to be sporadically poor U band photometry from the EC Survey, examples of which can be seen in the SEDs of EC 02566-1802 and EC 23379-3725 in Figure 2.10 and Figure 2.12 respectively. Unfortunately, we found no way to determine a priori if the EC U band photometry was poor, and therefore cannot correct for it in our fits. Based on the number of 3σ outliers in Figure 2 below 30,000 K we estimate the poor U band photometry to be affecting less than 10% of our sample.

Targets showing a 5σ excess in either the *W1* or *W2* bands or a 3σ excess in the *W1* and *W2* bands were flagged as infrared excess candidates. These criteria flagged 111 out of 378 white dwarfs with AllWISE detections as infrared excess candidates.

2.2.3 Infrared Excess Classification

While the selection of infrared excess candidates is straightforward, classification of the infrared source without a clean separation of the SEDs can be misleading. For programmatic searches of infrared excesses like the prior WIRED studies (Debes et al., 2011b; Hoard et al., 2013), the root of this problem is the shortage of infrared excess data points, which in our case is exacerbated by an incomplete near-infrared dataset. Techniques for classifying excesses as dusty debris disks are particularly lacking and needed for the large sample of white dwarf stars expected to be discovered by GAIA (Gänsicke et al., 2016a). Conventional color-color selection (Hoard et al., 2013) can miss the subtle infrared excesses that likely comprise a majority of dusty debris disks (Rocchetto et al., 2015; Bonsor et al., 2017), and it does not make use of all of the available information gained from fitting a model white dwarf atmosphere to the observed photometry, namely the photometric distance. More complex models can in theory distinguish between stellar and dusty infrared excesses (Debes et al., 2011b), but reduced chi-square metrics are often degenerate between stellar and dusty classifications given the limited number of infrared excess points constraining the models.

Because of these concerns, and our uniquely deficient photometry, we sought a simple technique that could distinguish between whether the excess is consistent with a dusty debris disk, an unresolved stellar or sub-stellar companion, or a background contaminant, and that would quickly highlight the best candidates for follow-up studies.

The simplest model that describes the infrared excess is a single temperature blackbody assumed to be at the photometric distance of the white dwarf star. Assuming the white dwarf atmospheric parameters and photometric distances derived above, we fit a single temperature blackbody to the observed infrared excess for each infrared excess candidate in our sample, with only the blackbody effective temperature and radius as free parameters. Figure 2.9 shows the results of the single temperature blackbody fits for our entire sample of infrared excess candidates, plotted as the effective temperature versus radius of the infrared source as scaled to the white dwarf radius. It is important to keep in mind that what is actually being fitted is a ratio of the solid angle subtended by the single temperature blackbody source to that of the white dwarf star, and so errors in the assumed white dwarf radius and distance, particularly for those with photometric atmospheric solutions where we have assumed a surface gravity, propagate into this measurement.

Figure 2.9 should not be interpreted as giving an accurate description of the temperature and radius of the infrared source, particularly for dusty debris disk candidates which are neither spherical nor at a single temperature, but rather it can be used as guidance for selecting targets of interest. To help guide the reader, we also plot in the background as light grey squares the effective temperature and radius for the stellar and sub-stellar models of Chabrier & Baraffe (1997) and Chabrier et al. (2000), which extend from early M dwarf stars down to sub-stellar and late type brown-dwarf stars, scaled to a typical $\log g = 8.0$ white dwarf radius. We also show the parameters for single temperature blackbody fits to all known dusty debris disks confirmed with *Spitzer*, independently fitted by Rocchetto et al. (2015), in the background as grey diamonds. We have derived the blackbody radius used in the fits of Rocchetto et al. (2015) from the white dwarf effective temperature, blackbody

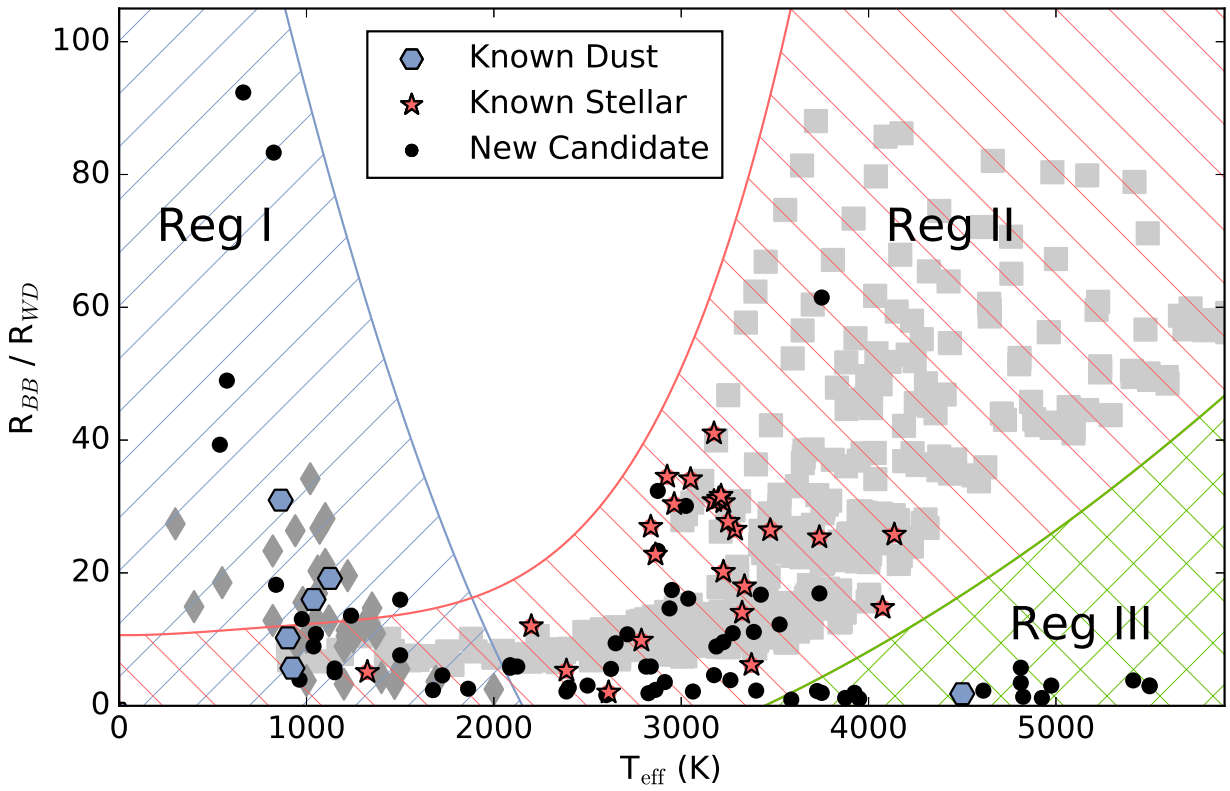

Figure 2.9: Plot of best-fitting blackbody T_{eff} and radius for each infrared-excess candidate (black circles), with the blackbody radius scaled to the white dwarf radius. Literature identified WD+dM systems are denoted with red stars while identified dust excesses are denoted with blue hexagons. Light grey squares show stellar and sub-stellar model effective temperatures and radii from the models of Chabrier & Baraffe (1997) and Chabrier et al. (2000) as scaled to a $\log g = 8.0$ white dwarf radius. Grey diamonds show the effective temperatures and radii adopted from the single temperature blackbody fits of all *Spitzer* confirmed dusty debris disks by Rocchetto et al. (2015).

temperature, and fractional infrared luminosity from their Table 3, assuming the radius of a $\log g$=8.0 white dwarf, consistent with what the authors used when fitting their single temperature blackbodies.

We also performed a literature search for all of the objects in our sample and found six with published infrared excesses identified as dusty debris disks and 44 with published infrared excesses identified as stellar or sub-stellar companions. We indicate these on Figure 2.9 with blue hexagons (dusty disks) and red stars (stellar companions) and see that, in general, these groups occupy distinct regions of the plot. We define three regions of interest in this plot. Region I is defined as a region of low effective temperature ($\mathrm{T} < 2000\,\mathrm{K}$) and varying radius. We see that the 5/6 known dusty debris disks in our sample cluster in this region in the lower left corner of our plot. The one literature identified dusty debris disk in our sample which does not follow this trend, PG 1457-086, is discussed in more detail in section 2.2.3 where we use archival high-spatial resolution imaging to show the infrared excess is likely the result of a previously unresolved contaminant and not a dusty debris disk. While the five literature-identified dusty debris disks in this region provide a nice set of boundaries for selecting new dusty debris disk candidates within our sample, the single temperature blackbody fits of the sample of 35 *Spitzer* confirmed dusty white dwarf systems from Rocchetto et al. (2015), overplotted as grey diamonds, provide an independent view of the extent of the dusty debris disk region.

In Region II, known stellar companions to white dwarfs congregate at higher temperatures and radii, in a locus around 3000 K and $30\,\mathrm{R_{WD}}$ ($0.4\,\mathrm{R_\odot}$), which are the temperature and radii expected for an unresolved M dwarf type companion. Region II extends down into the low temperature and small radius regime of Region I, where the overlap between dusty debris disks and late-type stellar and sub-stellar companions forces us to a less certain conclusion about the source of the infrared excess.

Objects in Region III, which consists of infrared excess best reproduced by objects of higher temperature ($\mathrm{T} > 3500\,\mathrm{K}$) and small radius $\mathrm{R} < 10\,\mathrm{R_{WD}}$ ($0.1\,\mathrm{R_\odot}$), have no obvious

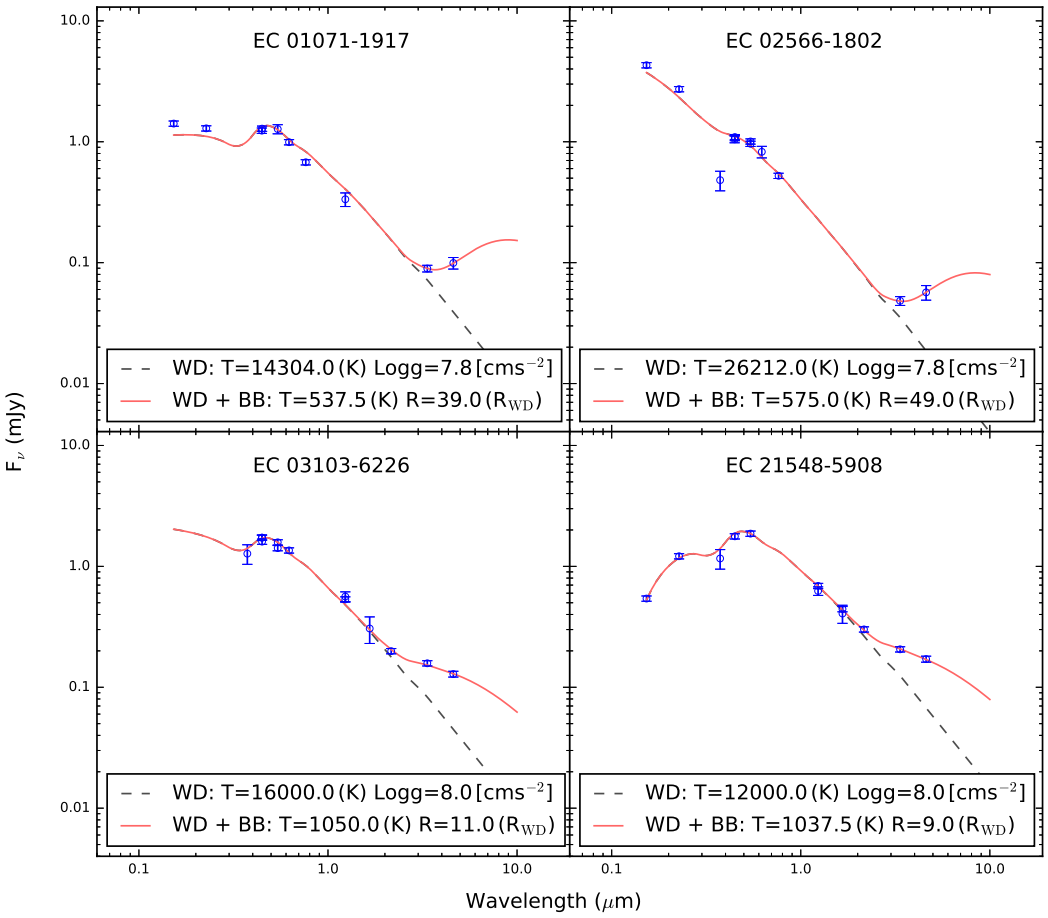

Figure 2.10: SEDs of four of the most promising dusty debris disk candidates with white dwarf model given as a dashed line and white dwarf plus single temperature blackbody fits shown as a solid line.

source, but are likely the result of mis-classification or contamination. We discuss each region and the objects they contain in detail in the following subsections.

Region I: Compact, Dusty Debris Disks

In addition to the empirical boundaries given by the single temperature blackbody fits to the known dusty debris disks, there is a corresponding theoretical expectation that dusty debris disks should congregate in this region. The formation of dusty debris disks via the tidal disruption of asteroids suggests they should not extend well beyond the asteroid tidal disruption radius at $1.0\,R_\odot$, or $85\,R_{WD}$ for typical white dwarf masses around $0.6\,M_\odot$

and asteroid densities $\sim 2\,\mathrm{g/cm^{-3}}$ (Veras et al., 2014b). At their inner edge, the cm to micron sized dust is only expected to be able to survive at temperatures below 2000 K before sublimating into gas (Rafikov & Garmilla, 2012). Since the dust within this region is expected be optically thick, the majority of it is shielded from direct radiation and it's temperature falls off rapidly with distance from the white dwarf (Chiang & Goldreich, 1997; Jura, 2003), with the outer dust near the tidal disruption radius radiating at only a few hundred degrees kelvin. The temperature of the single temperature blackbody fit along the x-axis of Figure 2.9 can be thought of as an area weighted temperature average of the dust disk, which given the expected inner and outer boundaries should be between 500-1500 K depending on the width of the disk. The radius of the single temperature blackbody plotted along the y-axis is less straightforward to interpret as it is dominated by the inclination of the dust disk.

There is some overlap with the stellar candidates defined by Region II and the bottom of Region I. We choose to list the objects in this overlapping region as dusty debris disk candidates. Because the new dusty debris disk candidates are of particular interest to this work, we provide the spectral energy distributions with the single temperature blackbody fits for each new dusty debris disk candidate in Figure 2.10 and Figure 2.12. Table A.1 provides a summary of the properties of all objects in Region I, including new debris disk candidates, known debris disk systems recovered by our search, and candidates we have chosen to reject as dusty debris disks based on either an obviously poorly fit SED or an independent physical reason, detailed in the Rejected Candidates notes. We also performed extensive literature searches on each object in this region and provide notes, additional data, and recommendations for follow-up on each object at the end of this section.

In the remainder of this section, we highlight our follow-up on four promising candidates which appear firmly inside of Region I, have high resolution spatial follow-up which suggests their *WISE* photometry is unlikely to be contaminated, and have optical spectroscopy to

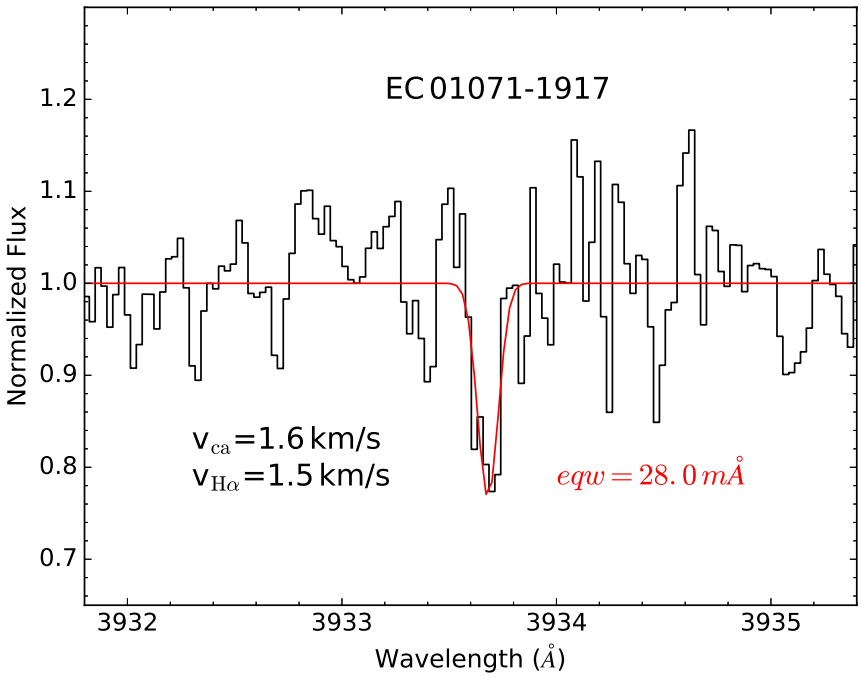

Figure 2.11: Combined UVES SPY spectrum for EC 01071–1917, centered on Ca K. Equivalent width measurement shown in red.

search for atmospheric metal pollution. The signature of recent accretion is not necessarily independent confirmation that an observed *WISE* infrared excess is consistent with a dusty debris disk. Recent studies have shown that the frequency of atmospheric pollution consistent with metal rich exoplanetary debris accretion could be as high as 25% (Koester et al., 2014). However, to date every confirmed dusty debris disk hosting white dwarf has been demonstrated to be actively accreting metal rich debris (Farihi, 2016) so limits on the atmospheric pollution from optical spectra can be used as an easy way to prioritize the necessary follow-up dusty debris disk candidates. The most commonly detected transition in the optical is the Ca II K resonance line at 3934 Å(Zuckerman et al., 2003; Koester et al., 2005; Kawka et al., 2011). For each object we provide measurements or conservative upper limits to equivalent widths of the Ca II K line based on archival or collected spectra. Ultimately, only higher spatial resolution, longer wavelength observations, or near-infrared spectroscopy can confirm *WISE* excesses as necessarily due to dust.

EC 01071-1917: Also known as GD 685 and WD 0107-192. The best-fitted single

temperature blackbody parameters place it well away from the overlapping stellar models of Region II. The ATLAS z band image is free of nearby contaminants. This object was also targeted as part of the SPY survey (Koester et al., 2001), from which we have adopted the spectroscopic effective temperature and surface gravity ($T_{\rm eff}$=14,304 K, $\log g$=7.8) for our white dwarf model parameters in the SED fit. We collected and combined the pipeline reduced archival SPY spectra using the ESO Science Archive to search for atmospheric Ca. We detect a subtle Ca K absorption feature shown in Figure 2.11 with an equivalent width of 28.0 ± 9.0 mÅ at a heliocentric corrected velocity of 1.6 ± 1.4 km/s, which is consistent with the white dwarf photospheric velocity of 1.5 ± 0.9 km/s as measured with a gaussian fit to hydrogen alpha line core.

EC 02566-1802: Also known as HE 0256-1802 and WD 0256-180. The best-fitted single temperature blackbody parameters place it well away from the overlapping stellar models. ATLAS z band imaging is free of nearby contaminants. We also obtained additional K_s follow-up with the SPARTAN infrared camera on the SOAR telescope (Loh et al., 2012) which confirm the lack of nearby sources, but are unable to provide additional calibrated photometry due to poor observing conditions. We adopt a spectroscopic temperature of 26,120 K and surface gravity of $\log g$=7.76 from the SPY survey (Koester et al., 2009) for our SED fits, which agrees with our independent photometric temperature. The white dwarf effective temperature is high, but not prohibitively so, for white dwarfs which host dusty debris disks. At this temperature, the optical spectra are less useful as probes for atmospheric pollution due to higher ionization states of atmospheric metals with transition wavelengths in the ultra-violet (Koester et al., 2005, 2014). Nevertheless we place an upper limit to the equivalent width of the Ca II K line of 17.5 mÅ. A nearby absorption feature of ~ 21.0 mÅ was detected at 10.3 ± 1.1 km/s, but is inconsistent with the white dwarf photospheric velocity of 25.5 ± 1.7 km/s, and is likely interstellar.

EC 03103-6226: Also known as WD 0310-624. The white dwarf model is well constrained and the best-fitted single temperature blackbody parameters place it within the

region of known dusty debris disks, though there is some overlap with the stellar models of Region II. VHS K_s band imaging is free of nearby contaminants. This object was identified as a white dwarf candidate and followed up spectroscopically by Subasavage et al. (2007), where it is noted that the difference in spectroscopic and photometric temperatures are suggestive of it being an unresolved double-degenerate candidate. Our independent photometric temperature is slightly hotter than their photometric fit (15,250 K vs 13,900 K) and in better agreement with their spectroscopic temperature of $\approx$17,000 K. Considering that both estimates of the photometric temperature assume a surface gravity of $\log g$=8.0, the remaining discrepancy could be within the photometric temperature error budget. We also obtained high signal-to-noise optical spectroscopy on 2015 November 18 with the Goodman Spectrograph on SOAR. We used the 0.46" slit in combination with the 1800 l/mm grating to cover a wavelength range from 3740 Å to 4580 Å with a resolving power of R $\approx$ 7000. No absorption features are detected near Ca K, resulting in an upper limit to the equivalent width of 46.5 mÅ.

EC 21548-5908: The white dwarf model is well constrained by multiple near-infrared photometry points (2MASS and VHS). VHS K_s band imaging is free of nearby contaminants. To confirm the atmospheric parameters, we obtained low resolution optical spectroscopy with the Goodman Spectrograph on SOAR covering the hydrogen Balmer series from Hβ blueward. Using the techniques described in Fuchs (2017), we fit the spectra to a grid of hydrogen atmosphere white dwarf models kindly provided by D. Koester (Koester, 2010), and determined a spectroscopic effective temperature and surface gravity of 12,330 K and $\log g$=8.04, which are consistent with the photometric fit. We also obtained high signal-to-noise optical spectroscopy on 2015 October 18 with the Goodman Spectrograph on SOAR, using the same instrument setup described for EC 03103-6226. No absorption features are detected near Ca K, resulting in an upper limit for the equivalent width of 65.9 mÅ.

The remaining candidates show be considered as lower priority for follow-up, but we are not yet able to rule them out as dusty debris disk candidates.

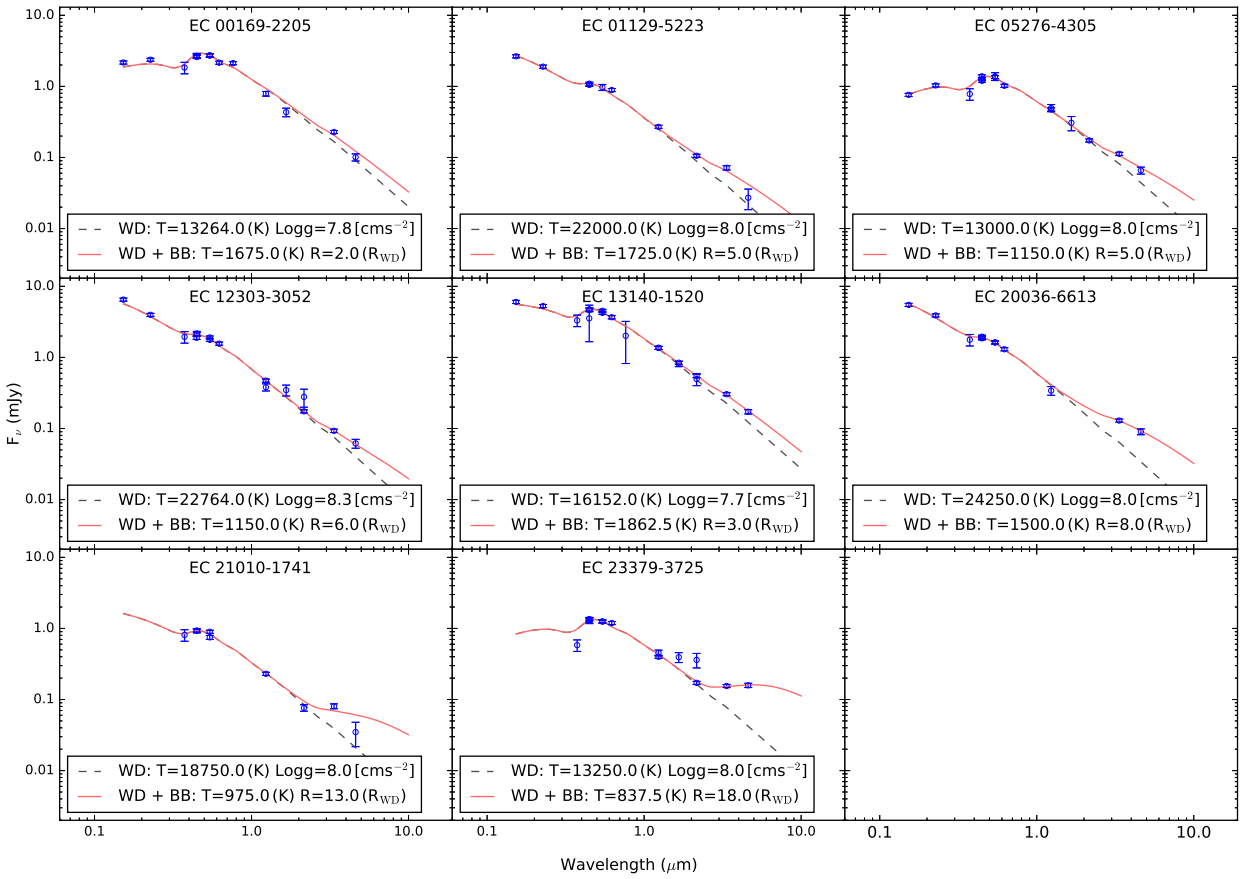

Figure 2.12: SEDs of new dusty debris disk candidates not shown in Figure 2.10. These candidates have not been search for signs of atmospheric accretion which should be the first step in their follow-up.

EC 00169-2205: Also known as GD 597 and WD 0016-220. This object has a tenuous excess, which does not continue into the *W2* band, although the error bars on *W2* are large. It was included as part of a high resolution imaging survey by Farihi et al. (2005) to uncover low luminosity companions to white dwarfs and no companion was detected. EC 00169-2205 was also included in the Zuckerman et al. (2003) search for metals in white dwarfs via the Ca II K line. No Ca was detected, and Zuckerman et al. (2003) provides an upper limit to the Ca K equivalent width of $< 10\,\mathring{A}$, which at this temperature, corresponds to an atmospheric abundance upper limits of [Ca/H] < -10. This would be an unusually low abundance for an object with an infrared bright dust disk (Farihi et al., 2012) and we therefore believe the detected excess to be the result of poor *WISE* photometry.

EC 01129-5223: Also known as JL 237. This object has a tenuous excess, which does not continue into the *W2* band, although the error bars on *W2* are quite large and the excess does begin in the Ks band which is high quality. The VHS K_s band image available is free of nearby contaminants. The spectral energy distribution is not very well constrained by the limited optical photometry, but the departure from blackbody in the K_s band and *W1* band are statistically significant.

EC 05276-4305: The excess is small but the white dwarf model is well constrained by the multiple near-infrared data points (2MASS and VHS). The VHS K_s band image is free of nearby contaminants.

EC 13140-1520: Also known as LP 737-47 and WD 1314-153. This object has a tenuous excess, and no high spatial resolution imaging exists to search for nearby contaminants.

EC 20036-6613: The white dwarf model is well constrained by the multiple optical photometry data points but the object is lacking in near-infrared photometry. We obtained

follow-up K_s band imaging with the SPARTAN infrared camera on the SOAR telescope, which shows a nearby source likely contaminating the *WISE* photometry.

EC 21010-1741: The white dwarf model is well constrained by the high quality VISTA infrared data points, but the infrared excess is not consistent with a single source between *W1* and *W2*. The VHS K_s band image available shows a potential nearby contaminant, which is likely the source of the infrared excess.

EC 21459-3548: The white dwarf model is not well constrained by the limited available photometry, particularly in the near-infrared. ATLAS z band imaging reveals a nearby contaminant that is too close to be resolved in *WISE* photometry.

EC 23379-3725: The best-fitted single temperature blackbody parameters place it well away from the overlapping stellar models. The discrepant near-infrared data present some concern for contamination, but the VHS K_s band imaging is free of nearby contaminants.

The candidates listed as Rejected Candidates are objects that were classified as dusty debris disk candidates but have some external reason for us to discard them as candidates for continued follow-up.

Rejected Candidates: We chose to reject nine candidate dusty debris white dwarfs for a variety of reasons. Their SEDs are shown in Figure 2.13. EC 00323-3146 and EC 04552-2812 were designated spectral type 'DAwk' in the EC catalog, indicating narrow/weak Balmer lines preventing clear DA white dwarf classification. EC 19442-4207 is identified in the EC catalog as a CV/DAe, indicating the system is a cataclysmic variable (O'Donoghue et al., 2013). Both EC 12303-3052 and EC 11023-1821 were followed up with *Spitzer* by Rocchetto et al. (2015) and found to have no infrared excess, indicating the *WISE* excesses are the result of contamination. EC 04114-1243 and EC05024-5705 both have white dwarf

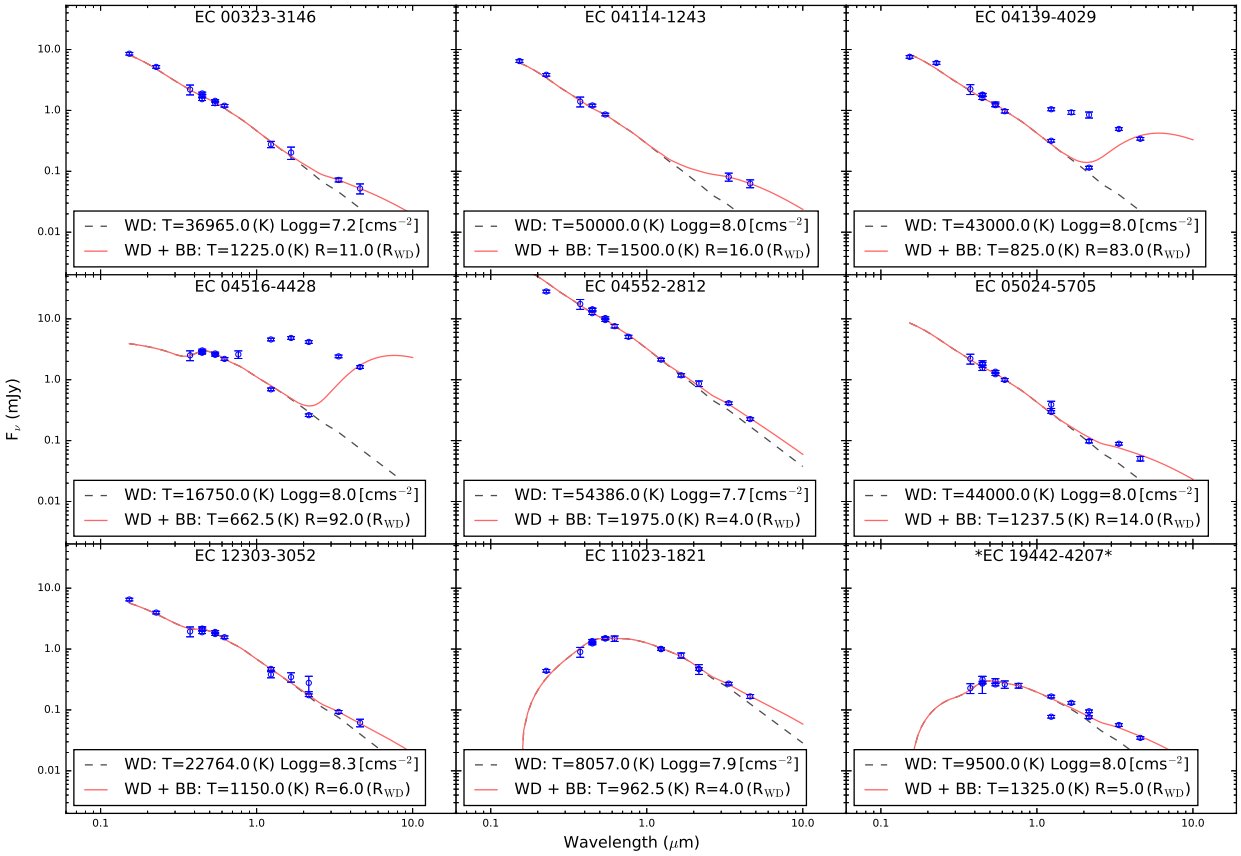

Figure 2.13: SEDs of rejected candidates. *Denotes fluxes plotted in (Jy). The discrepant near-infrared photometry seen in EC 04139-4029, EC04516-4428, and EC19442-4207 results from source confusion in the 2MASS photometry that was resolved by the higher spatial resolution VHS photometry.

temperatures which are too high for optically thick dust to survive sublimation within their tidal disruption radius (von Hippel et al., 2007). EC 04139-4029 and EC 04516-4428 are both are strong outliers in Figure 2.9. Their spectral energy distributions are suggestive of source confusion, particularly the highly discrepant near-infrared data from 2MASS and VHS. The higher spatial resolution images for both objects from VHS show nearby sources, indicating the *WISE* excesses are very likely the result of contamination.

Region II: Unresolved Stellar/Sub-Stellar Companions

The results of objects that fall within Region II are summarized in Table A.2. We provide examples of SEDs of objects with the stellar classification in Figure 2.14. We note that for

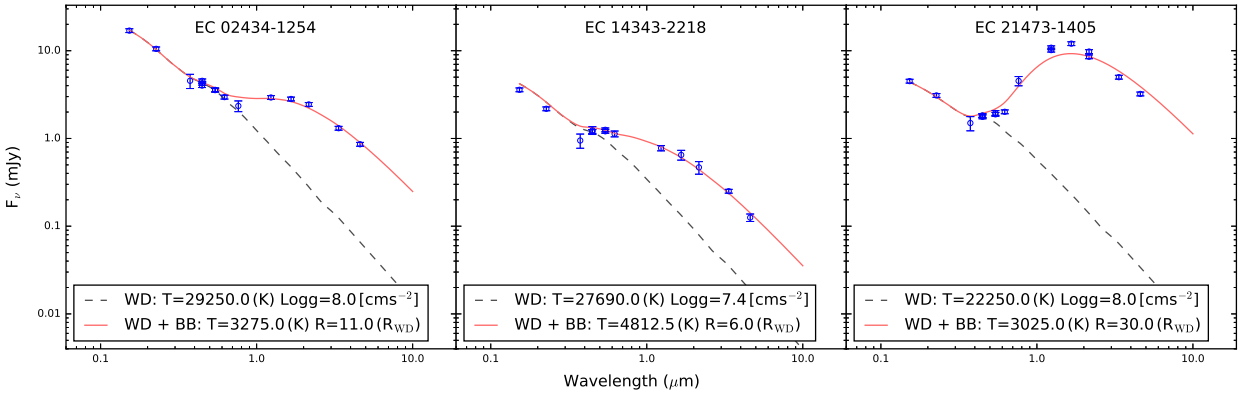

Figure 2.14: Examples of SEDs of stellar/sub-stellar companions

the brighter stellar excesses which begin in the optical wavebands, our white dwarf models often attempted to fit some of the additional optical flux from the unresolved companion, resulting in white dwarf model fits that were systematically overluminous, and single temperature blackbody fits that were systematically underluminous, pulling the single temperature blackbody fits to lower temperatures. To account for this, we re-fit the white dwarf models restricting our photometry to wavelengths less than 0.5 μm. The positions of objects in Figure 2.9 and the fitted parameters given in Table A.2 reflect our best-fitted values after this correction was applied. More detailed modeling is necessary to determine the stellar companion spectral type.

Region III: High Tempertaure, Small Radius

The third region of Figure 2.9 consists of objects with an infrared excess that is best fitted by a single temperature blackbody with a high temperature ($T > 4000\,K$) and small radius ($R < 10\,R_{WD}$). The results of objects that fall within this region are summarized in Table A.3. Examples of objects in this region are shown in Figure 2.15. The nature of the objects populating this region is less obvious than the other two regions. Furthermore, since Region III includes one of the known dusty debris disks in our sample, PG 1457–086, we took great care in investigating this region. We propose these objects are the result of some combination of the following four scenarios.

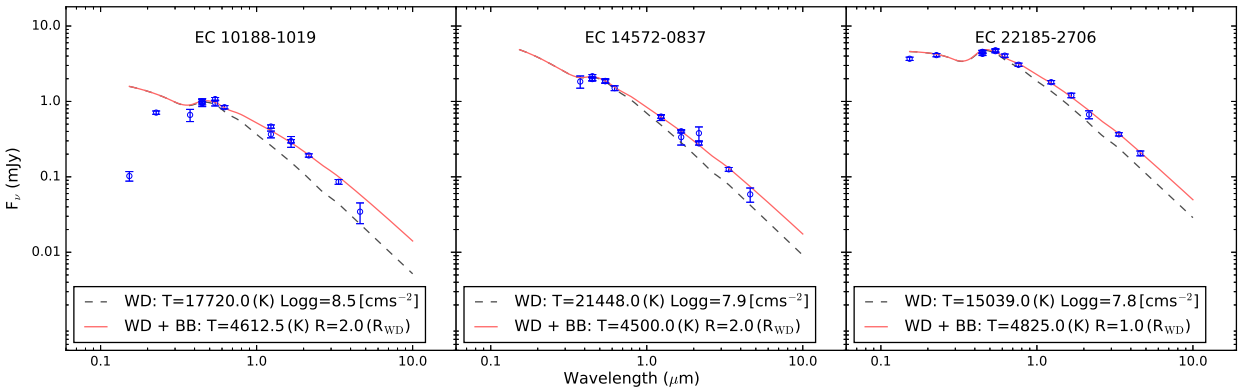

Figure 2.15: Examples of SEDs with High Temperature/Low Radius Excesses

1) Erroneous stellar classification/poor photometry/poor WD model fit: The first thing that stands out when looking through the results in Table A.3 is that 6/15 of the objects have an uncertain EC spectral type and five of them are identified as potential hot sub-dwarfs. With uncertainty about the object classification, we can no longer rely on our DA white dwarf atmospheric models to accurately predict the photometric flux in the near-infrared. 5/9 remaining objects have high signal-to-noise spectral follow-up and atmospheric model parameter fits from either the Gianninas (Gianninas et al., 2011) or Koester spectroscopic surveys (Koester et al., 2009) so they cannot be accounted for by misclassification.

If an erroneously high white dwarf temperature model is applied to the photometry, the difference in slope between the SED of the model and true white dwarf can result in the excesses observed in this region. This appears to be the case for at least one of the white dwarfs where we have assumed a spectroscopic temperature, EC 10188-1019, as evidenced by the highly discrepant *GALEX* photometry. Our fitted photometric temperature is much lower than the reported spectroscopic temperature from Gianninas et al. (2011) (11,000 K vs 17,720 K), and the difference in temperature completely accounts for the observed infrared excess. We note that EC 10188-1019 is flagged by Gianninas et al. (2011) as being magnetic, which is likely affecting the spectroscopic temperature as non-magnetic models were assumed for the fits.

As discussed in both Koester et al. (2009) and Gianninas et al. (2011), the Balmer

features used to determine spectroscopic atmospheric parameters peak in strength around 13,000-14,000 K, and fits of white dwarfs near this temperature often suffer from a hot/cold solution degeneracy across this boundary. Photometric fits are one way to break this degeneracy. Three white dwarfs in this region have spectroscopic temperatures near this boundary, the magnetic white dwarf EC 10188-1019 discussed above, EC02121-5743, and EC 22185-2706. Again, if the 'hot' solution was erroneously chosen to represent the white dwarf photometry, cooler white dwarf models could explain the observed infrared excess for these objects.

2) Irradiated sub-stellar/planetary mass companion: The best-fitted radii of objects in this region are consistent with Jupiter and brown-dwarf sized companions, but the best-fitted temperatures require a substantial amount of additional heating for far-out planets. The post-main sequence evolution of the white dwarf progenitor is expected to result in planetary re-heating via accretion and irradiation (Spiegel & Madhusudhan, 2012), but the temperatures needed to fit the infrared excesses in this region ($T > 4000$ K) are well beyond what is expected. Furthermore, the thermal relaxation timescale of the re-heated planets is on the order of hundreds of millions of years, meaning re-heated planets would only be expected around the youngest white dwarfs in this sample (Spiegel & Madhusudhan, 2012), making this scenario unlikely.

There are a handful of confirmed white dwarf-brown dwarf binaries in compact orbits which suggest that, despite engulfment, the brown-dwarf survives post-main sequence evolution relatively unscathed (Farihi & Christopher, 2004; Maxted et al., 2006; Casewell et al., 2012; Steele et al., 2013). The compact orbits lead to tidally synchronous orbits and significant differences between dayside and nightside brown-dwarf surface temperatures (Casewell et al., 2015). Despite the strong irradiation, the day-side temperatures (≈ 3000 K) are still too cool to explain the excesses seen in this region (Casewell et al., 2015). Nonetheless, if the excesses in this region are the result of irradiated brown-dwarf companions, there should be observable spectral features in the near-infrared and optical, and brightness modulations

from tidal and reflection effects from the companion. The lack of these features could quickly rule out compact brown-dwarf companions.

It is also worth pointing out that previous studies have found the brown dwarf companion fraction to white dwarfs to be low. In a search for binary companions that included near-infrared direct imaging and near-infrared excess techniques, Farihi et al. (2005) find the white dwarf brown dwarf companion fraction to be $< 0.5\%$. In a previous WIRED study, Debes et al. (2011b) find the observed frequency to be between $1.3 \pm 0.6\%$ after accounting for likely contaminants. Even in the most optimistic case, in our sample of 383 white dwarfs with *WISE* detections we should only expected 7-8 white dwarf brown dwarf systems, which is not sufficient to explain all of the observed excesses in this region.

3) Unresolved contaminants: Another way to produce the subtle excess is with an unresolved, line-of-sight object which is at a different distance than the white dwarf. Even with high quality near-infrared follow-up from the VISTA-VHS survey, care must still be taken to confirm the excesses seen in this section are not the result of a contaminant. We find EC 14572-0837, also known as PG 1457-086 (hereafter EC 14572), to be an example of contamination by an unresolved background source.

EC 14572 is identified in the literature as a dusty debris hosting white dwarf, with strong atmospheric metal pollution (Farihi et al., 2009). The infrared excess was confirmed by *Spitzer* and determined to be most consistent with a dusty debris disk. EC 14572 is included in the sample of *Spitzer* confirmed dusty debris disks identified by Rocchetto et al. (2015)

EC 14572 is the only published dusty debris disk that we failed to correctly identify in our single temperature blackbody selection. Because this indicated a short-coming in our dusty debris disk selection technique, we performed a thorough archival data search to determine if any additional data on this system. Our ESO archive search revealed that EC 14572 was a target in a multi-epoch, high-contrast and high-spatial resolution imaging search for Jupiter

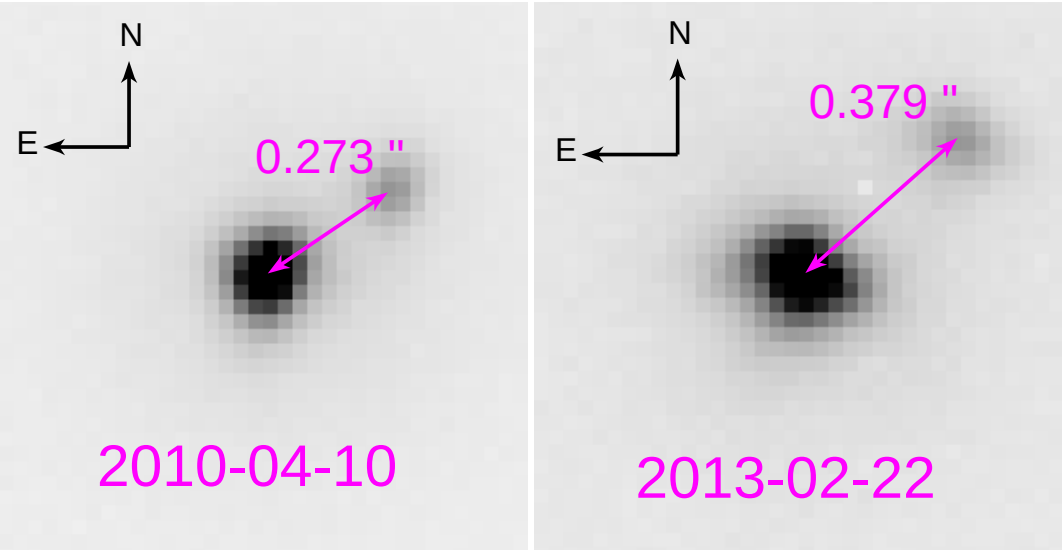

Figure 2.16: Two epochs of NAOS+CONICA high resolution near-infrared images of EC 14572. The two J band images show a very nearby source which does not appear to be in a common proper motion pair with the white dwarf.

sized planets around dusty debris disk hosting white dwarfs with the NAOS+CONICA near-infrared imager on the Very Large Telescope as a part of program 085.D-0673(A) led by M. Radiszcz. The high quality J band imaging reveals a close contaminant. Figure 2.16 presents two epochs of imaging from this study for EC 14572, taken 3 years apart, centered on the brighter object, with approximate separation measurements.

The change in separation between the two epochs of 0.126" is consistent with the direction and magnitude of the proper motion of EC 14572 as measured by the PPMXL survey (μ_α =2.4 mas yr^{-1} and μ_δ=-38.8 mas yr^{-1}), suggesting the two objects are not in a common proper motion pair. We performed aperture photometry on the two sources and find the flux ratio between the white dwarf and the contaminant to be 3.2±0.6, which is agreement with the excess flux above the white dwarf model observed in the J band. The best-fitted blackbody that can explain the excess has a temperature of 4400 K.

Any additional flux from the unforeseen companion is certainly contaminating our near-infrared and *WISE* data, and is very likely present in the *Spitzer* data of Farihi et al. (2009). Though Farihi et al. (2009) scaled the white dwarf model photometry to the near-infrared

data when modeling the excess as a dusty debris disk, effectively including the near-infrared flux of the unresolved contaminant in their stellar model, if the contaminant is significantly cooler than the white dwarf the difference in slope of the spectral energy distribution at these wavelengths could be solely responsible for the infrared excess measured for EC 14572. Given the difference in proper motion between the white dwarf and contaminant, increased separation should allow future follow-up to independently measure the near-infrared flux of the white dwarf and the contaminant, and definitively resolve the source of the excess infrared radiation.

2.3 Significance of Results

As a result of our work, thirteen new dusty debris disk hosting white dwarf candidates have been identified, including two with clear signs of ongoing atmospheric accretion, EC 05365–4749 and EC 01071–1917. If confirmed, these candidates have the potential to increase the sample size of dusty debris disk hosting white dwarfs by more than 25%. The ratio of atmospheric Calcium and Magnesium accretion rates in EC 05365–4749 derived in subsection 2.1.7 point towards a parent body with a unique abundance pattern, similar to the differentiated material found in the Earth's crust. After our publication of these results, EC 05365–4749 was selected as a target for Hubble Space Telescope observations as part of a cycle 24 general observers program to further study the accreted material. The results of that study are awaiting publication.

More significantly, the techniques we pioneered in the discovery of candidates, including the application of forced photometry and the single temperature blackbody selection technique, are ideally suited for prioritizing the follow-up of the hundreds of dusty debris disk candidates expected to be uncovered by studies of the GAIA white dwarf sample. The GAIA white dusty white dwarf sample has the potential to increase the sample size of known dusty white dwarf by an order of magnitude, but only if the true dusty debris disks can be separated from the likely contaminants. As we have demonstrated with EC 14572 in section 2.2.3,

our single temperature blackbody selection method is capable of isolating white dwarfs with nearby contaminants where other selection techniques have failed, and will enable for more accurate targeted follow-up of future samples.

CHAPTER 3: Gaseous Observations [1]

In addition to their dusty components, a handful of accretion disks around white dwarf stars also display double-peaked emission lines from hot, circumstellar gaseous components to their debris disks. In this chapter we discuss our new observations of the gaseous components of the exoplanetary debris disks, which required a substantial upgrade to the Goodman Spectrograph prior to beginning data collection. The new Red Camera upgrade was completed in the Spring of 2017 and is available to all SOAR observer, further expanding the scientific reach of the Goodman Spectrograph. Of the eight known gaseous debris disk hosting systems, four had studies published on their variability over the course of this thesis project. These objects include WD 1617+1620 (Wilson et al., 2014), WD J0845+2257 (Wilson et al., 2015), WD 1226+110 (Manser et al., 2016b), and WD 1041+091 (Manser et al., 2016a) and are not included in this thesis. We present our follow-up of the four remaining systems, three of which show no significant evolution in their emission profiles over the baseline of observations. The fourth object, HE 1349–2305, displayed significant variations in its Ca II infrared triplet emission profiles over the course of our observations, which lasted just over a year. The yearly variations we observed occurred on a timescale more than an order of magnitude shorter than what has been observed in other similar systems. We discuss the challenges these rapid variations present to the current understanding of gaseous debris disk evolution in more detail in section 4.3.

[1]Parts of the work presented in this chapter previously appear in *The Astrophysical Journal*, see Dennihy et al. (2018)

3.1 The Red Camera Upgrade

The Goodman Spectrograph was initially designed with a focus on high throughput at wavelengths shorter than 400 nm, making it an ideal spectrograph to observe the blue dominated spectra of white dwarf stars. However, achieving this design goal came with a few detriments to scientific performance at longer wavelengths. The most dramatic of these is a high frequency pattern imprinted on images taken at longer wavelengths of light (beyond 700 nm), which is caused by the interference of the incoming light with its own reflection off of the surface of the thinned charge-coupled device detector (CCD). This fringing pattern has amplitudes greater than 20% at wavelengths around 850 nm, which is the region in which the gaseous debris disks show emission lines, and the fringing pattern is not completely stable due to the flexure in the instrument. Conventional data reduction techniques can reduce this fringing pattern to approximately $\pm$ 2%, but the signal-to-noise of the observations is always limited by this pattern.

Since it is inherent to the physical thickness of the CCD, this fringing pattern is unavoidable, and has plagued observers at longer wavelengths since the spectrograph was installed. To address this issue, the scientific advisory board of the SOAR telescope approved the purchase of a new, fringe-suppressing CCD in late 2013 to replace the existing CCD. Replacing the existing blue-optimized CCD with the fringe suppressing CCD camera would require a sacrifice in quantum efficiency at shorter wavelengths and risk extended instrument downtime during commissioning of the new camera. Instead we elected to perform a re-design of the back-end of the spectrograph to support the independent use of two cameras, which constituted a significant upgrade of a facility class instrument. Hereafter we will refer to the old CCD camera as the 'Blue Camera' and the new fringe supressing camera as the 'Red Camera'.

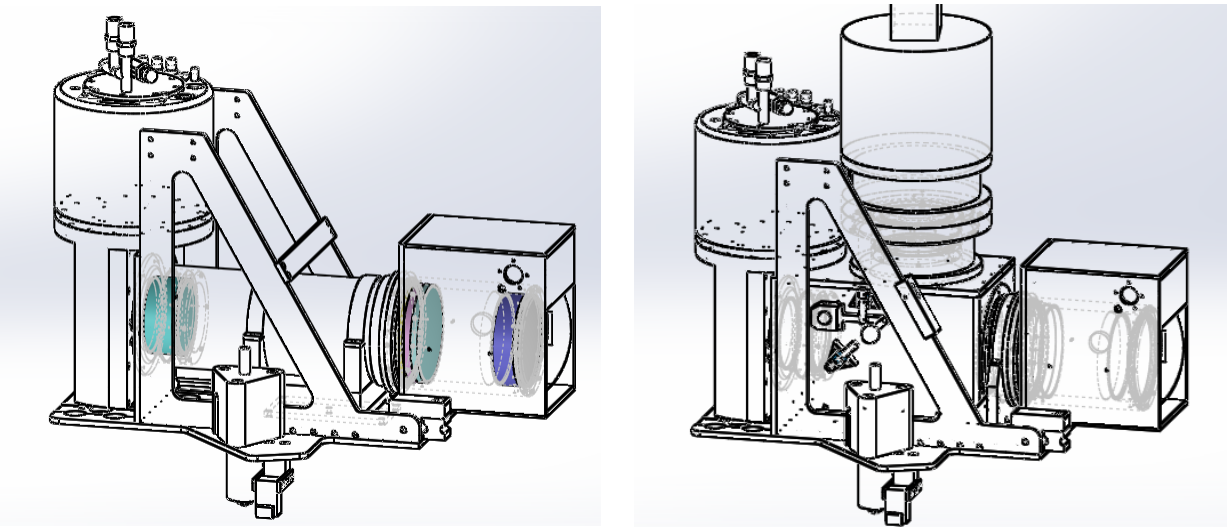

Figure 3.1: Left: Original Goodman Spectrograph camera stage designed to support a single camera. Right: Our two camera design utilizing existing hole patterns for mating and maintaining original performance of the current spectrograph.

3.1.1 Design

The new two-camera design needed the ability to redirect the optical path to the desired camera as part of a routine daytime operation. Additionally, to accommodate the new opto-mechanical structure, we needed to redesign the focus stage of the spectrograph which maintained optical alignment of the system without compromising the performance of the Blue Camera. The two camera design was done using Solidworks auto-cad software. The mechanical design of the Red Camera support and mirror housing (hereafter optical switchyard) utilized light-tight mating surfaces and was equipped with adjustable mounting points to ensure optical alignment upon installation.

We performed a finite element analysis to simulate the flexure of the new mechanical design under varying gravitational loads to ensure the design met the original instrument specifications for flexure and image quality. By incorporating the measured flexure from these simulations into the optical model of the spectrograph in Zemax, we were able to verify the current performance of the Blue Camera would be maintained. Examples of these studies are shown in Figure 3.2 and Figure 3.3.

We employed a hand-operated fold mirror to intercept the incoming light beam, with

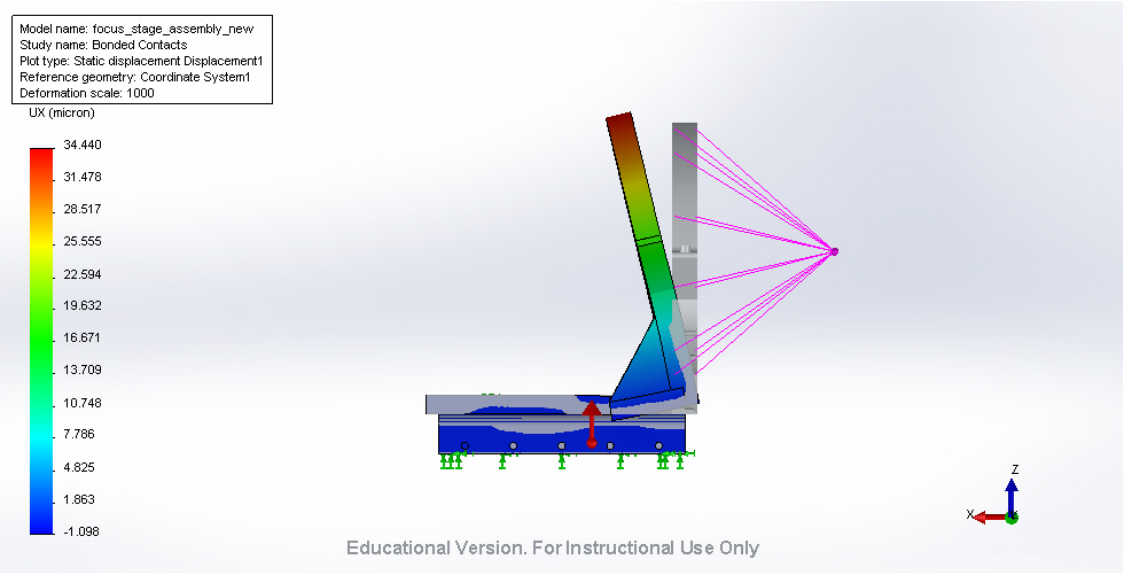

Figure 3.2: Deformed view of focus stage under increased weight load of new camera at 1000:1 deformation scale. Color-bar scale represents deflection along optical axis (x-axis on image) in units of microns.

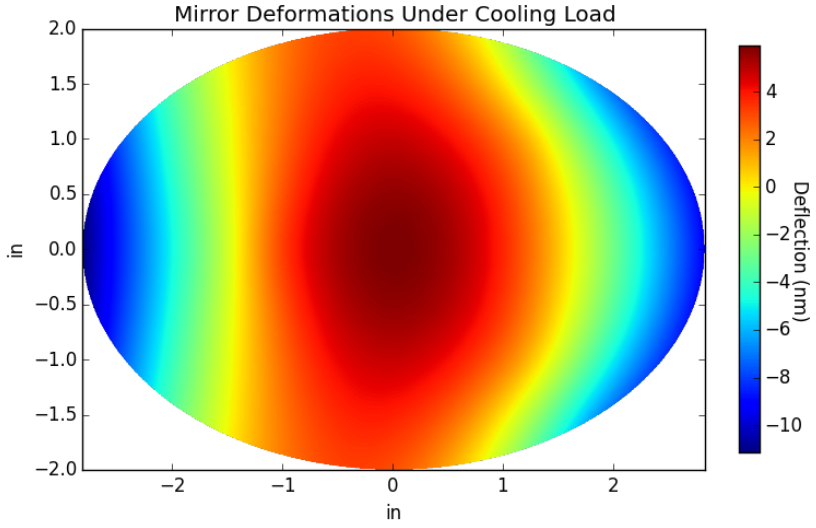

Figure 3.3: Second order mirror deflection under cooling load manifested as a surface deformation. Colorscale in units of nm. The expected deformations are below the flatness spec of the mirror surface.

an optimized coating chosen with input from a design review committee. The mirror was mounted to its rotating support using silicone based adhesive. Thermal flexure analyses were performed to optimize the placement of the adhesive and ensure the wavefront accuracy of the mirror under varying thermal loads, the results of which are shown in Figure 3.3. After removing the first order tilt from the surface of the mirror, one can visualize the 2nd order surface deformations to check for curvature which may compromise the image quality. These deformations were minimized by the choice of adhesive pad surface area and are well below the flatness spec of the mirror (note the colorscale is in units of nm).

In March 2015 the design passed review conducted by a committee including the SOAR telescope director and members of the scientific and technical staff and we were given the green light to begin integration into the instrument.

3.1.2 Integration and Performance

The mechanical assembly along with a dummy camera to simulate the weight and moment of the new camera were installed in May 2015 in advance of the delivery of the Red Camera. In January 2016 the Red Camera arrived at SOAR and we made our first attempt at commissioning. An internal power failure required us to ship the Red Camera back to the manufacturer for repair. In March 2016 we returned to continue commissioning of the Red Camera, which has been installed and operating since. Shared-risk scientific use of the Red Camera by external groups began in the Fall of 2016 and the full scientific release followed in the Spring of 2017. The camera is now available to all SOAR observers including the entire US astronomical community through NOAO shares as a standard Goodman option.

The deep-depletion silicone CCD of the Red Camera has reduced fringe amplitude by more than a factor of 10 compared to the Blue Camera. In Figure 3.4 we show two low resolution spectra which illustrate the improvement. The low frequency pattern seen in both the red and blue data is inherent to the light source, but the high frequency pattern which begins around 650 nm is the fringing in the Blue Camera. The Red Camera shows no

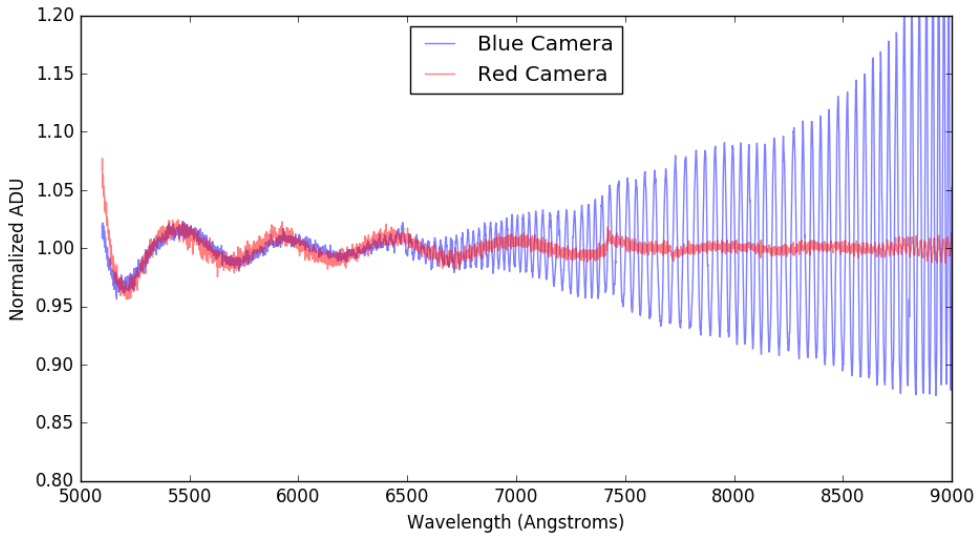

Figure 3.4: Normalized flat-field comparison between spectra taken with the Red and Blue camera. The low-frequency pattern seen in both is inherent to the illumination source, but the high-frequency pattern seen at redder wavelengths is the fringing due to the CCD.

apparent fringing above 2% out to 900 nm.

We also collected filtered photometry using the lamps internal to the telescope dome and standard star fields to quantify the relative throughput between the Red and Blue cameras. With the spectrograph in the Red Configuration, we took a series of SDSS u,g,r,z dome flats, noting the dome lamp percentage and exposure time. The spectrograph was then switched to the Blue Configuration and the dome flats were repeated with the same exposure time and dome lamp percentage. In this way, the data suffers from the uncertainty in the repeatability of the dome lamp percentage. The frames were then bias-subtracted and gain-corrected before taking the ratios of median electron counts in an image region in each filter bandpass to calculate the relative throughput.

For the on-sky data, we used the Sloan Digital Sky Survey Southern Spectrophotometric standard field E9-A. We started the night configured with the Blue Camera, obtained five to seven images in the filters u,g,r, and z, then switched to the Red Camera and repeated the exposures with the same exposure time. We started with the u-band filter on the Blue Camera at an airmass of 1.11, and finished with the z-band filter on the Red Camera at an

SDSS u'	SDSS g'	SDSS r'	SDSS i'	SDSS z'
Dome Flat Comparison				
1.05	0.98	1.00	–	1.37
On Sky Comparison				
0.53	0.94	–	1.29	1.68

Table 3.1: Throughput comparison for the Red Camera vs Blue Camera using two different sources. The Dome Flat measurements rely on the repeatability of the brightness setting of the lamp, which is known to be problematic. Based on the relative quantum efficiencies of the Red and Blue detectors, we suspect the On Sky Comparison to be correct.

airmass of 1.27. The frames were bias subtracted, flat-fielded, and gain corrected, before being combined for aperture photometry. Aperture photometry was performed with a large aperture on the five brightest non-saturated stars for each filter. The median red/blue ratio of the five targets was used to calculate the relative throughput.

Results of both of these tests are given in Table 3.1. The difference between the two methods is likely due to the different spectral shapes of the illuminating sources and the uncertainty in the repeatability of the dome lamp percentage. Based on the relative quantum efficiencies of the Red and Blue detectors, we suspect the On Sky Comparison to be correct. Nonetheless, they provide general guidance for selecting a camera based on scientific needs. Observers are advised to choose the Blue Camera for observations at wavelengths shorter than 400 nm, the Red Camera for any observations longer than 700 nm, and either camera is acceptable in between.

3.2 Initial search for gaseous debris disk hosting systems

With the new Red Camera we were able to rapidly obtain high-quality spectroscopic observations of debris disk hosting systems. One of the outstanding questions in the field is what conditions are needed to produce the gaseous emission lines, which are only observed in about 20% of dusty debris disk hosting systems. As part of search of new gaseous emission line disks and to establish a baseline of observations for future studies, we carried out a survey to probe all debris disk hosting systems observable with the SOAR telescope for gaseous

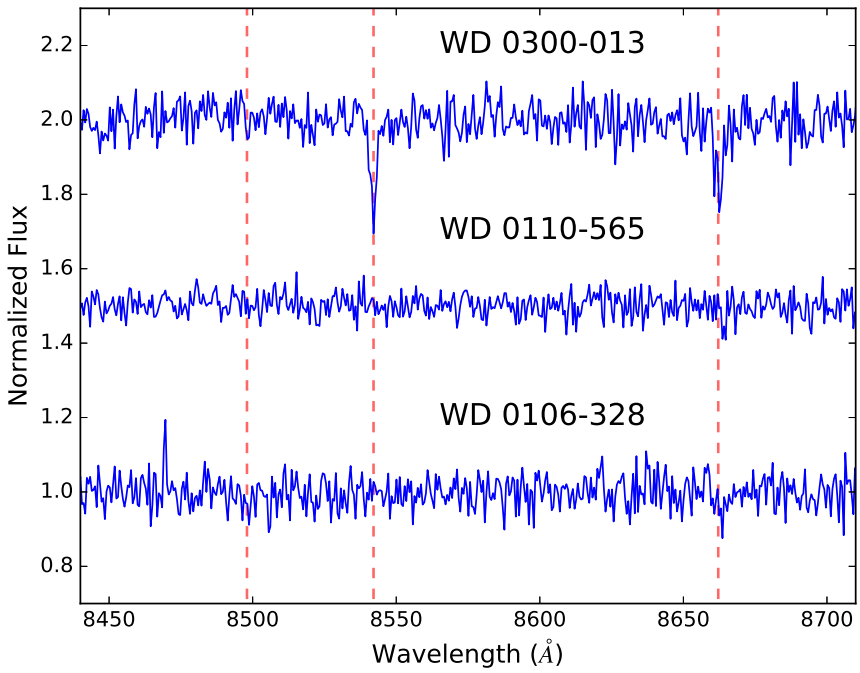

Figure 3.5: SOAR spectra used to rule out Calcium triplet emission in three dusty debris hosting white dwarfs. The dashed red line shows the rest wavelength of the calcium triplet. Atmospheric Calcium is seen in absorption in the DB white dwarf WD 0300-013.

emission at the Calcium Infrared Triplet (Ca II at 850nm, 854nm, and 866nm), which is the most common tracer of gaseous debris in these systems. For each observation we used the 1200 l mm^{-1} grating and the 1.03" slit for a resolution of approximately 2.25 Å and a wavelength coverage of 7900–9000 Å. The spectra from each epoch were bias-subtracted, flat-fielded, wavelength-calibrated, and optimally-extracted using a modified version of the Python reduction package described in Fuchs (2017), before being combined into a final signal-to-noise weighted spectrum. The search returned zero new gaseous emission hosting systems but non-detections are still informative. Examples of our non-detections are shown in Figure 3.5 and we discuss the significance of these non-detections in the context of debris disk evolution in section 4.2

3.3 Follow-up of known Gaseous Debris Disks Systems

As discussed in subsection 1.3.2, a handful of the gaseous emission line hosting systems have been shown to be highly variable on timescales of decades (Manser et al., 2016a), suggesting all eight of the systems should be regularly followed-up. Here we discuss our new observations of the four remaining gaseous emission line hosting debris disks which do not yet have published variability studies.

Three of the four gaseous debris disk systems we followed-up do not show significant variability over the baseline of observations. These systems are WD 0738+1835 Figure 3.6, WD J0959-0200 Figure 3.7, and WD 1144+0529 Figure 3.8. Curiously enough, two of these systems show narrow emission features as opposed to the broad emission features seen in other systems. This could be interpreted as a result of either low inclination or gaseous debris at larger radii. The lack of variability over the observed baseline could also point to a much longer variability timescales, and these observations can therefore serve as reference for future studies.

3.4 Rapid Variations of the Gaseous Emission Profile in HE 1349–2305

The fourth gaseous debris disk, which coincidentally was the first target observed on the first official science night with the Red Camera, turned out to be highly variable. Here we present our comprehensive spectroscopic follow-up of the gaseous debris disk orbiting the dusty, metal-polluted, helium-dominated atmosphere white dwarf HE 1349–2305 (Girven et al., 2012; Melis et al., 2012). Our observations show morphological variations in the Ca II triplet emission profiles on a timescale of one to two years. Despite many similarities with other well-studied systems, the observed timescale is an order of magnitude shorter, and likely incompatible with the general relativistic precession previously invoked to explain the decadal variations seen in other systems. We discuss this scenario and an alternative theory based on the spiral density waves seen in other astrophysical accretion disks in section 4.3.

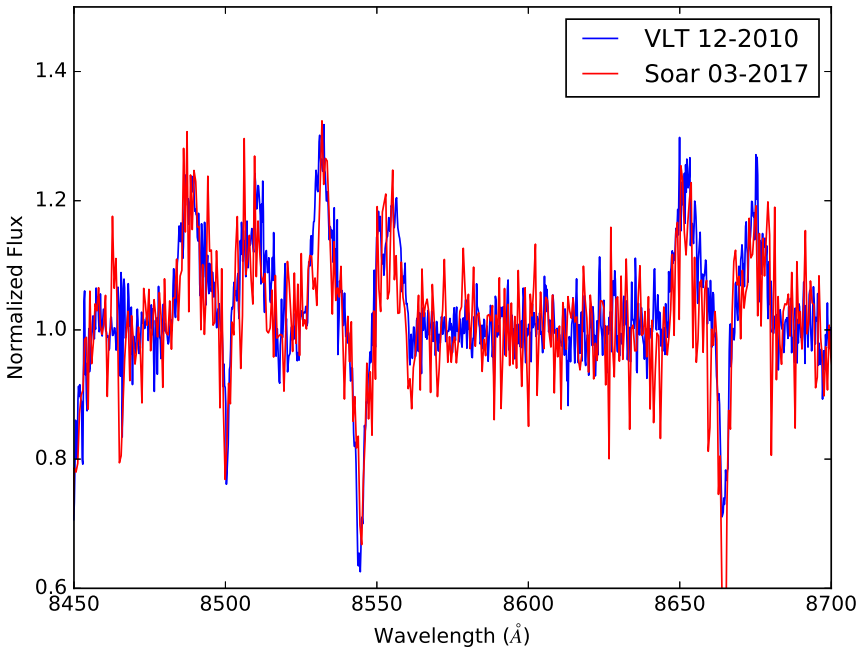

Figure 3.6: WD 0738+1835 showing no apparent evolution despite its minor emission profile asymmetry. This is the only system with asymmetric emission profiles to not show red-to-blue variations.

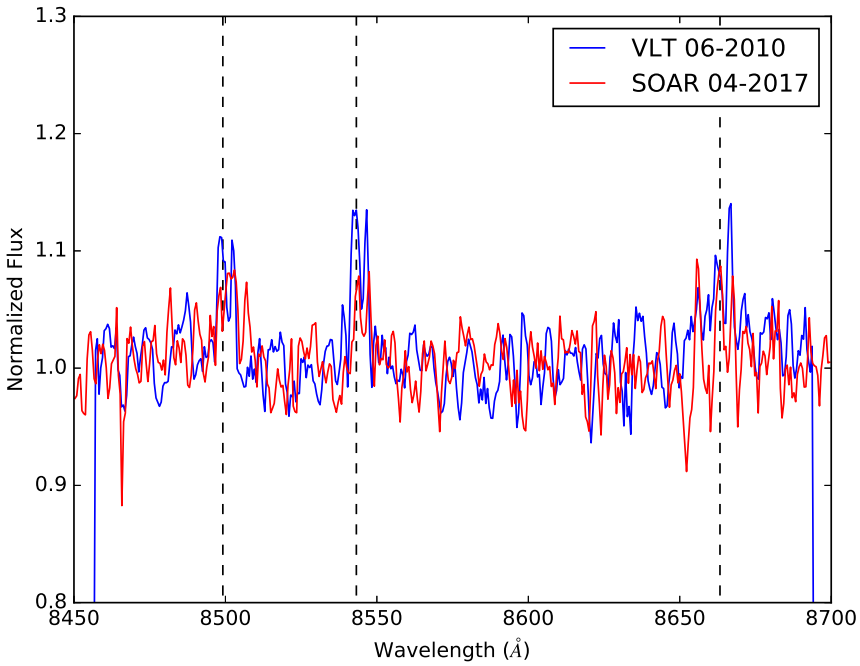

Figure 3.7: WD J0959-0200 showing no apparent evolution. The low signal-to-noise of the observations hinders careful analysis of the profile shapes.

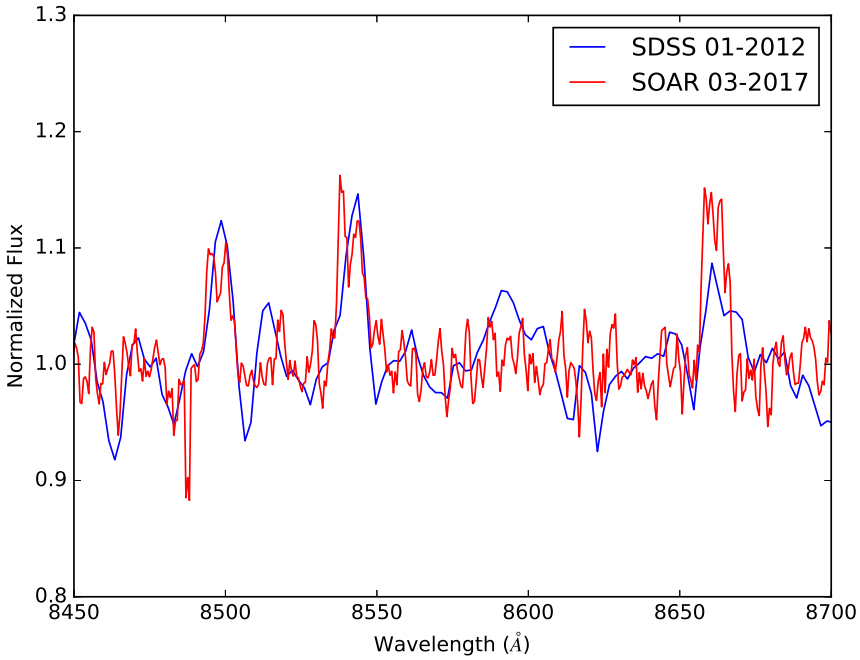

Figure 3.8: WD 1144+0529 showing no obvious evolution in its narrow emission profiles over the five year baseline between observations.

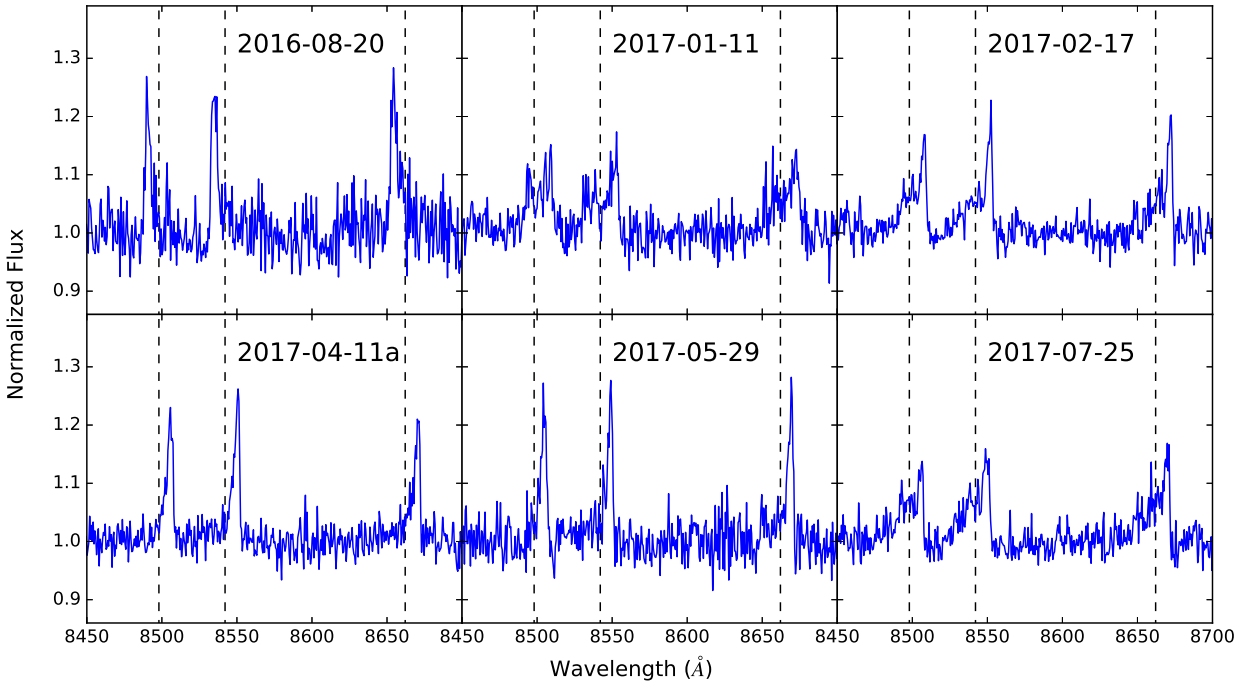

Figure 3.9: Collection of HE 1349–2305 spectra, representative of evolution of the Ca II triplet emission profiles. The vertical dashed lines denote the rest wavelengths of the Ca II transitions at 8498, 8542, and 8662Å. The bulk of the emitting material has undergone a 400 km/s velocity shift in less than nine months.

3.4.1 SOAR/Goodman Observations

HE 1349–2305 is a metal polluted DB type white dwarf star which was initially discovered to host circumstellar gaseous debris via its double-peaked Ca II triplet emission features by Melis et al. (2012) and later shown to also host an infrared bright dusty component to its debris disk (Girven et al., 2012). Given that the Ca II triplet emission features were mildly asymmetric, it was identified as a strong candidate for variable emission (Manser et al., 2016a).

Our initial observations of HE 1349–2305 are shown in the first panel of Figure 3.9. The blue-dominated emission peaks represented a significant change from the mildly red dominated peaks presented in Melis et al. (2012), and suggested morphological evolution similar to other well studied gaseous debris disks. Since the target was setting, our next observation did not come until January 2017. During the observable season of January 2017 to August 2017, we conducted a comprehensive spectroscopic campaign on HE 1349–2305, collecting data over 14 different epochs with separations ranging from a few hours to a few weeks. The observations are detailed in appendix B, along with several measurements of the Ca II triplet emission line profiles which are discussed in subsection 3.4.2.

For each observation we used the 1200 l mm^{-1} grating and the 1.03" slit for a resolution of approximately 2.25 Å and a wavelength coverage of 7900–9000 Å. The spectra from each epoch were bias-subtracted, flat-fielded, wavelength-calibrated, and optimally-extracted using a modified version of the Python reduction package described in (Fuchs, 2017), before being combined into a final signal-to-noise weighted spectrum. Total integration times ranged from 3600 to 7200 seconds resulting in signal-to-noise ratios in the continuum around 8400 Å between 30 and 50 per pixel. Wavelength calibration was performed using the plethora of night sky emission lines available, as identified by Osterbrock et al. (1996), and we have applied heliocentric velocity corrections to each observation.

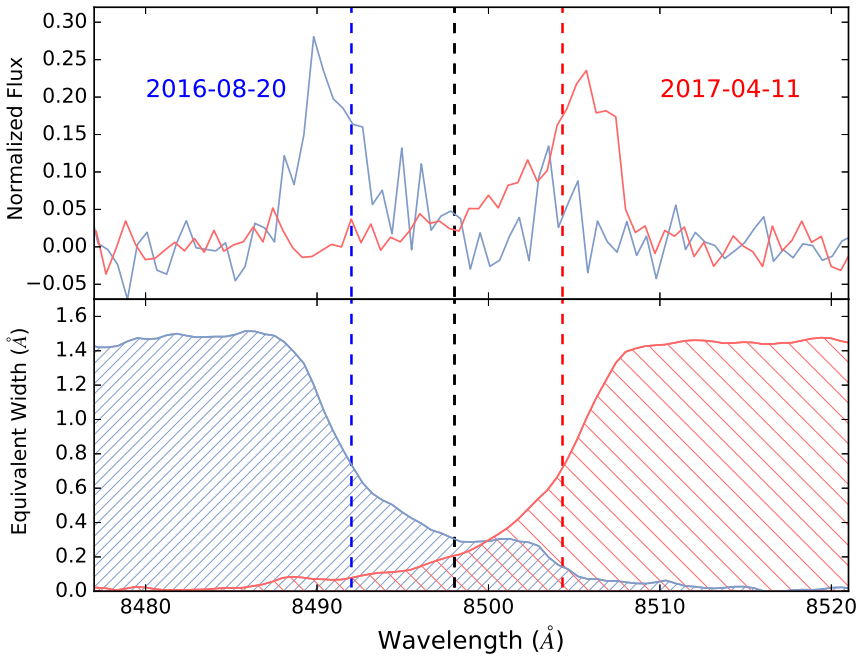

Figure 3.10: Velocity centroid measurements of two epochs with opposite asymmetries. The red and blue dashed vertical lines show the centroid wavelength shifts compared to the rest wavelength of the transition shown in black. The direction of integration is reversed for the 2016 August 20 blue-shifted phase for clarity.

3.4.2 Ca II Triplet Emission Profile Measurements

Throughout the observing campaign, all three of the Ca II triplet emission profiles undergo clear morphological changes, starting with a blue-dominated profile in August 2016, transitioning to a nearly symmetric profile in January 2017, rapidly evolving to a red-dominated profile by April 2017, and finally returning to a nearly symmetric profile by July 2017.

To track the variability, we determine the cumulative equivalent width of each profile and measure the wavelength at which it reaches its midpoint, which we term the centroid of the profile. This technique was previously utilized to study the wavelength shifts of polycyclic aromatic hydrocarbons in Sloan et al. (2005, 2007), and similar techniques have been used to study asymmetries in stellar absorption line profiles (Gray, 2005).

Figure 3.10 demonstrates this centroid measurement for two epochs of opposing phase. In the upper panel we plot the spectra, and in the lower panel we show the cumulative

equivalent widths, or integral, of each spectrum as a function of wavelength. Though the direction of integration is reversed for displaying the blue-shifted profile in Figure 3.10, for our analysis the integration is always performed from blue to red. We translate the wavelength centroids to velocity centroids using the known wavelengths of each transition, providing three independent measurements of centroid velocity for each epoch.

To derive uncertainties for each velocity centroid measurement, we used a Monte Carlo method of re-sampling the spectra assuming a normal distribution with the measured data as the mean and the rms scatter of the data in the continuum as the standard deviation. We also explored systematic effects of continuum fitting by trialing a range of polynomial orders (linear, quadratic, or third order) and continuum widths (between 25 Å and 30 Å away from the known wavelength of the transition) for normalization of the re-sampled spectra. We include this systematic effect in our final calculation of the values in Table B.1, and the measurements and uncertainties represent the mean and range of the velocity centroids found using the different continuum fitting parameters we explored.

We apply this same analysis to the equivalent width measurements of each profile and find that they do not vary to within the calculated uncertainties. We note however that the equivalent width measurement is much more sensitive to continuum fitting than the velocity centroid, and a more careful analysis should be performed before any conclusions on equivalent width variability are drawn.

We plot our velocity centroid measurements as a function of time in Figure 3.11. A sinusoidal fit to the velocity centroids with amplitude, phase, period, and mean as free parameters results in a period of 1.4±0.2 years, which is an order of magnitude shorter than timescales inferred from systems with similar emission profile variations (Manser et al., 2016a). We find no systematic differences in the residuals among the different Ca II triplet profile measurements.

We explored the dependence of this period on observation sampling effects by explicitly rejecting the August 2016 measurements and using a Monte Carlo re-sampling of the velocity

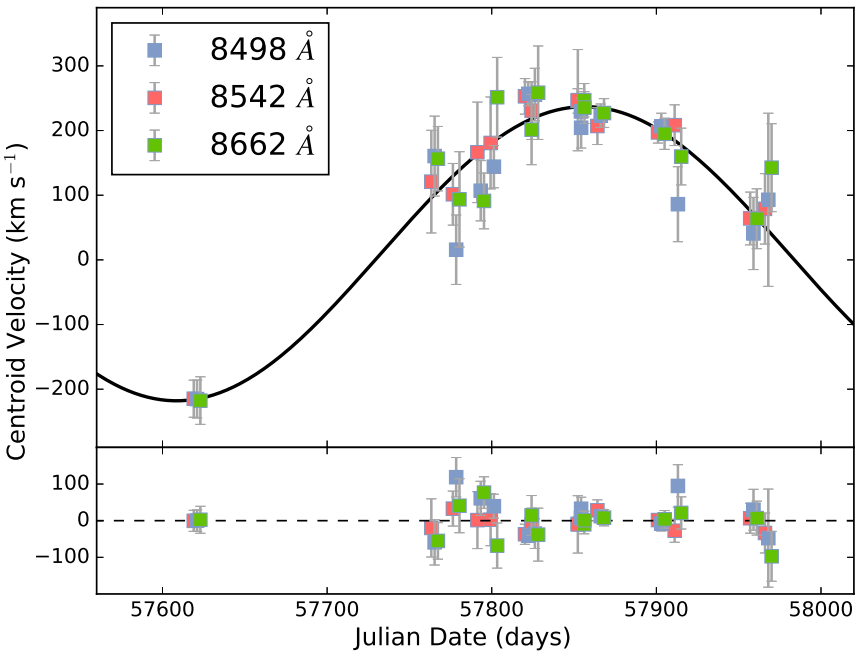

Figure 3.11: The best-fit, 1.4 year period sinusoid (solid line) of the velocity centroid measurements of the Ca II triplet emission profiles (top) and residuals (bottom).

measurements to explore the distribution of best-fit parameters. Without constraints on the mean or amplitude, the best fit sinusoids prefer shorter periods around 0.8 years. However, these solutions require means and amplitudes around 140 km s^{-1} and 100 km s^{-1}, meaning they never result in a phase where the emission profile is blue-shifted, which is confidently ruled out by the three independent August 2016 profiles. If we restrict the mean of the sinusoids to be near zero, we find that the distribution of best fit periods peaks around 1.2 years, with a tail extending to longer periods up to 1.8 years.

Therefore, even in absence of the August 2016 data, the variations support the 1.4 year period interpretation. We note that this interpretation also agrees with our measurement of the velocity centroid for the March 2011 data presented in Melis et al. (2012), but the uncertainty of the measured period prohibits an accurate phasing of the two datasets. Finally, we note that we have not yet observed a complete cycle of variations, and it remains to be seen whether the variability is truly periodic. We discuss the implications of this short timescale in section 4.3.

3.5 Significance of Results

The lasting impact of this work is likely to come from the continued use of the Red Camera on the Goodman Spectrograph by SOAR observers. By eliminating the high amplitude fringing at longer wavelengths, the Red Camera opens a new spectroscopic window for observers, and several studies have already been carried out making use of its unique capability including in the follow-up of the electromagnetic counterpart to the binary neutron star merger gravitational wave detection (Nicholl et al., 2017). The Red Camera also provides a functioning spare to the Blue Camera should it encounter a fault, minimizing downtime to the workhorse instrument of the 4m SOAR telescope.

While our search for new gaseous emission line hosting systems came up empty, the careful analysis of the systems with non-detection can be used to shed light on the origin of the gaseous emission line systems, which we discuss further in section 4.2. Finally, with our confirmation of variability in the emission line profiles of HE 1349–2305, five of the eight known gaseous emission line systems have now been shown to vary, a continuing trend that our observations of the remaining three systems will help test in future studies. The rapid variations observed in HE 1349–2305 also provide a fantastic test for theories of debris disk variability, and we discuss these implications for the current interpretation of debris disk variability in section 4.3.

CHAPTER 4: Global Evolution of the Dusty and Gaseous Debris in the Disks [1]

The new observations for both the gaseous and dusty components of exoplanetary debris disks around white dwarf stars that we have collected for this work have a wide range of applications to theories of global debris disk evolution. An understanding of the global evolution of material through the debris disk would provide independent constraints on the accretion rates of metals onto the white dwarf surface, improving our estimates of the abundace ratios of the accreted bodies. In this chapter we discuss several interpretations of our new observations, demonstrating their utility to theoretical studies.

We begin with a re-analysis of the evolutionary trends observed in the bulk sample of white dwarfs with dusty infrared excesses observed by (Rocchetto et al., 2015), considering what effects the introduction of an elliptical dust model, initially developed in our study of the infrared excess around EC 05365–4749, would have on these trends. We will show that the tendency towards faint infrared disks around younger white dwarfs could reflect a trend in eccentricity, with more frequent disruption events resulting in more eccentric disks around young white dwarfs, which are fainter in the observed near-infrared bands.

We continue with a fresh look at the sample of dusty debris disk hosting white dwarfs in the context of our single temperature blackbody plane introduced in subsection 2.2.3, and identify the systems which also host gaseous debris as forming a boundary of this region. We consider whether this indicates an evolutionary track of dusty debris hosting systems moving towards a state of gaseous emission. We will also demonstrate how population synthesis

[1]Parts of the work presented in this chapter previously appear in *The Astrophysical Journal* and the *Astronomical Society of the Pacific Conference Series*. See Dennihy et al. (2016), Dennihy et al. (2017b), Dennihy et al. (2017a), and Dennihy et al. (2018)

techniques can be used to probe similarities between the gaseous debris disk hosting systems in ways that are not apparent when comparing results from single object studies, potentially leading to what makes these systems different than others that do not show gaseous emission.

Finally, we discuss the rapid variations of the gaseous emission lines in HE 1349–2305 presented in section 3.4. We argue that the current interpretation of the general relativistic precession of a fixed pattern used to describe the longer emission profile variations seen in other similar systems is unable to describe our new observations considering what is already known about the system. We consider the propagation of global density waves within the gaseous component of the disk as an alternative model capable of explaining both the decadal variations seen in other systems and yearly variations we have observed.

4.1 Ellipitical Dust Disk Models

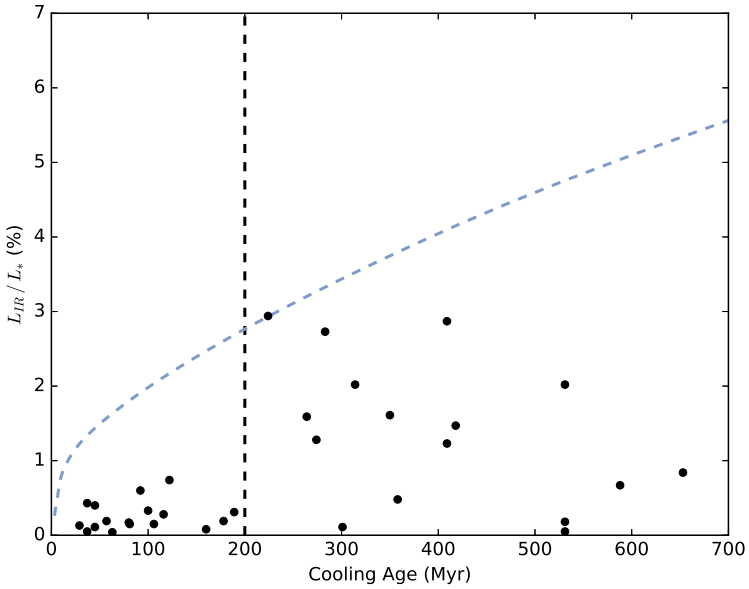

Figure 4.1: The reproduced central panel of Figure 4 from Rocchetto et al. (2015). The dashed blue line tracks the expected fractional infrared luminosity from a face-on disk filling its available orbital space, while the vertical dashed black line delineates the bins of young and old white dwarfs

The sample of dusty white dwarf systems has now grown to the point to where we can

begin examining the properties of the sample as a whole, rather than individual objects. One such study (Rocchetto et al., 2015) examined the distribution of fractional infrared luminosities of all known dust systems as a function of white dwarf cooling age. In Figure 4.1, we show a reproduced version of the central panel from Figure 4 of Rocchetto et al. (2015), which is also described in subsection 1.3.1. Plotted on the vertical axis is the observed fractional infrared luminosity, or a ratio of the brightness of the infrared source to the white dwarf, and on the horizontal axis the white dwarf cooling age. The dashed blue line tracks the fractional infrared luminosity of a disk with dust which fills all of its available orbital space between the sublimation and tidal disruption radius and is seen face on, so the complete disk area is visible to the observer. This line represents a maximum fractional infrared luminosity under the assumption that the dust extends from the theoretical inner limit of the sublimation radius to the expected outer limit of the tidal disruption radius.

The observed fractional infrared luminosity of a given dusty debris disk is not expected to always lie along the dashed blue line even if it does completely fill its available area due to the inclination of the disk with respect to our line of sight. Instead we expect a smooth distribution of fractional infrared luminosities below the dashed blue line, reflecting a sample with random disk inclinations. While that distribution seems apparent for discs around cooler white dwarfs, there is an abrupt drop in the observed fractional disc luminosity at about 200 Myr, identified by the vertical dashed black line. Given the number of systems in the bin of younger white dwarfs, there is a very low probability that the reduced fractional infrared luminosity (relative to the dashed blue line) is due to high inclination. In other words, it is statistically improbable that all of these disks are being observed in an edge-on configuration. Instead, this work clearly suggests the discs around younger white dwarfs are inherently fainter.

One way to make fainter disks without adjusting the inclination, as suggested by Rocchetto et al. (2015), is to assume they are not filling all of their available orbital space. In

other words the discs around young white dwarfs could just be narrower than their counterparts around older white dwarfs. These suggestions are supported by Bochkarev & Rafikov (2011), which demonstrated that the global evolution of an optically thick dust disk trends towards narrow rings, and the increased radiation of the younger white dwarfs could accelerate this process. Here we explore an alternative origin for the fainter infrared excesses by considering the effects an elliptical dust distribution would have on the observed spectral energy distribution.

The concept of elliptical dust distributions is also partially motivated by the fact that the formation scenario of dusty debris disks necessitates highly eccentric orbits during the tidal disruption phase. The eccentric rings formed by individual disruptions are expected to circularize under the effects of Poynting-Robertson drag on timescales ranging from tens to thousands of years for the relevant particle size scales (Veras et al., 2015), but the effects of multiple disruption events and collisions on the eccentricity evolution of disks is largely unknown.

4.1.1 A Case Study of an Elliptical Dust Disk around EC 05365–4749

To construct our elliptical disk model, we begin by adopting the same passive, flat, and opaque assumptions about the dust particles as considered by Jura (2003). We consider the white dwarf to be at the center of our radial coordinate system, and the inner and outer ellipses that bound the disk to be described by the parameters $a_{\rm in}$, $a_{\rm out}$, and e where $a_{\rm in}$ and $a_{\rm out}$ define the semi-major axes of the inner and outer ellipses, and e defines the eccentricity of the ellipses which we hold fixed for all nested ellipses. The ellipses are confocally nested with the white dwarf at one focus. In this way, the coordinate r specifies the distance to a dust particle from the white dwarf which uniquely determines the particle temperature under the assumption of an optically thick, flat disk. The inner/outer ellipses which bound the disk are then described by the equation:

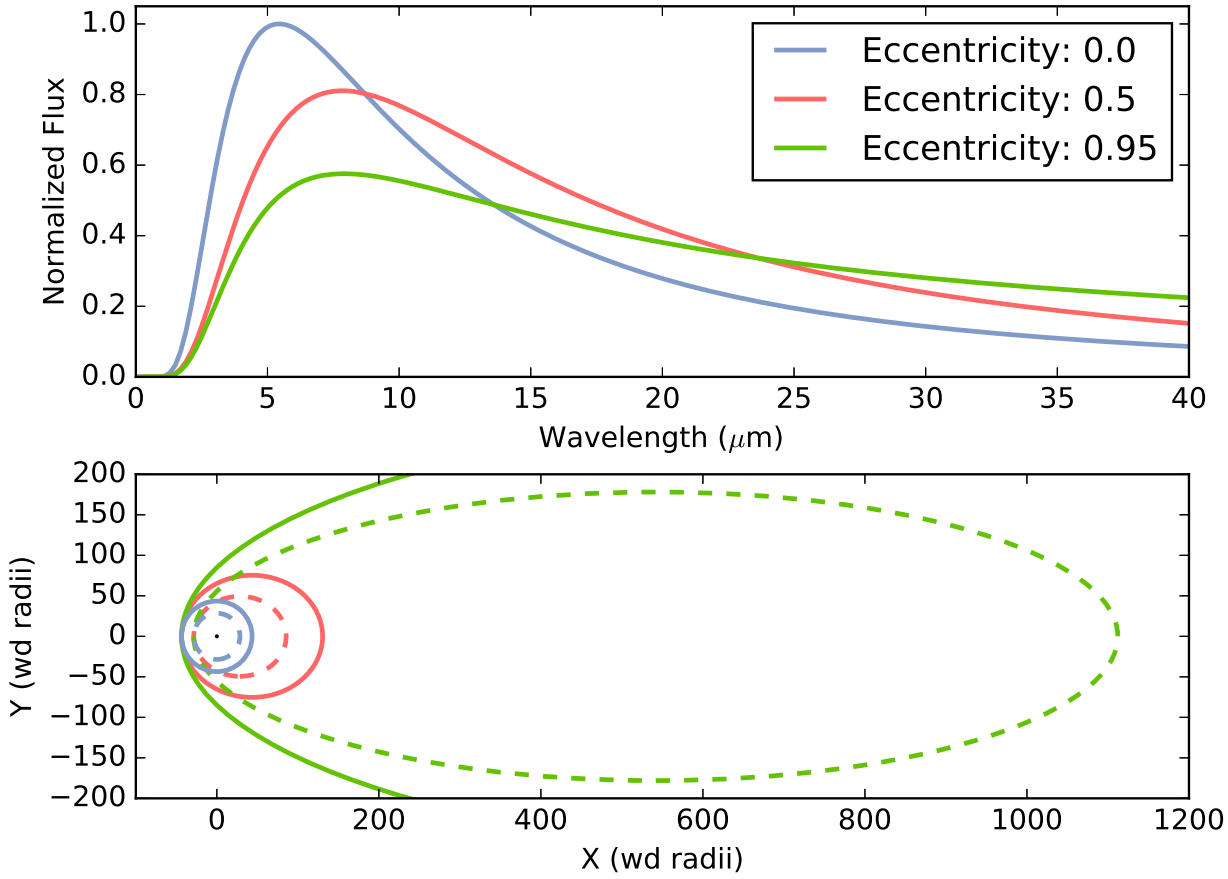

Figure 4.2: Elliptical and Circular spectral energy distributions with corresponding face on geometrical projections. As the eccentricity of the disk grows, material gets redistributed to further distances, decreasing the average temperature of the dust and pushing the flux in the SED to longer wavelengths.

$$r_{\mathrm{in/out}}(\theta) = \frac{a_{\mathrm{in/out}}(1-e^2)}{1-e\cos\theta} \tag{4.1.1}$$

and our integral for the observed monochromatic flux as a function of frequency becomes:

$$F_\nu = \frac{\cos i}{D^2}\int_0^{2\pi} d\theta \int_{r_{\mathrm{in}}(\theta)}^{r_{\mathrm{out}}(\theta)} B_\nu\left(T_{\mathrm{ring}}(r)\right) r dr \tag{4.1.2}$$

where i is the inclination of the disk and D is the distance to the system.

An illustration of this geometry and its effect on the spectral energy distribution is shown in Figure 4.2. Note how as the eccentricity grows and material is redistributed to larger distances from the white dwarf, the monochromatic flux in the resulting spectral energy distribution is redistributed to longer wavelengths, and the luminosity in bands we typically observe (somewhere between 1-10 μm) is decreased, thereby reducing the observed infrared flux of the disk without adjusting its inclination. As a case study, we explored whether the necessity of narrow disk width for low inclinations could be relieved for the subtle infrared excess we discovered around EC 05365–4749 in section 2.1 by modeling the infrared excess as a set of confocally nested elliptical rings rather than concentric circular rings.

For a qualitative comparison between circular and elliptical models, we applied both models to the infrared excess observed for EC 05365–4749 as described in subsection 2.1.5 with a fixed inner radius of the disk corresponding to a temperature of 1100K. We varied the difference between the periastron of the inner/outer ellipses and the inclination for both a circular ($e = 0.0$) and highly elliptical ($e = 0.95$) disk model to produce the constant chi-square boundaries shown in Figure 4.3. The 1, 2, and 3-σ confidence intervals correspond to the chi-squared contours of 2.30, 6.18, and 11.8 above the minimum chi-squared value for each grid, as appropriate for two parameters of interest. The circular and highly eccentric models have comparable minimum chi-squared values which are consistent with a reasonable fit.

There is a stark difference between the acceptable parameter space for EC 05365–4749

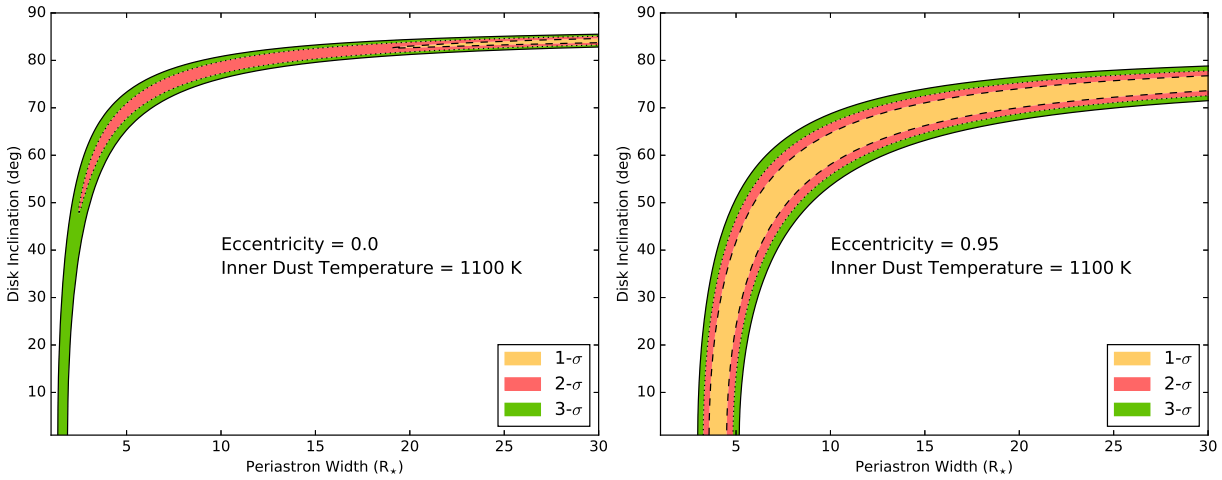

Figure 4.3: Dashed, dotted, and solid lines show filled contours of 1, 2, and 3-sigma confidence intervals of the periastron width and inclination of a dust disk with inner dust temperature 1100 K around EC 05365–4749. The left-hand panel shows how the near infrared flux of the SED constrains the dust to be in either narrow rings or viewed at high inclinations. The right-hand panel shows how elliptical disks might allow a disk at periastron to be wider over a larger range of inclinations.

for circular and elliptical disks illustrated by Figure 4.3: for a given inclination, the elliptical disk is markedly wider at periastron. This can be intuitively understood as close-in material is re-distributed to farther distances along the eccentric orbit, effectively shifting flux from the near-infrared out to longer wavelengths.

This qualitative difference holds true independent of the inner dust temperature assumed. Given the lack of long wavelength data where the models begin to diverge, there is no quantitative (e.g. goodness of fit measurement) distinction between either model, especially considering the addition of the free parameter e. The results are however encouraging for elliptical SEDs as an alternative explanation for the lack of younger disks with dust spanning the available orbital range between the sublimation and tidal disruption radius. The delineation between the dust distributions of the younger and older samples could instead be the product of a third parameter, eccentricity.

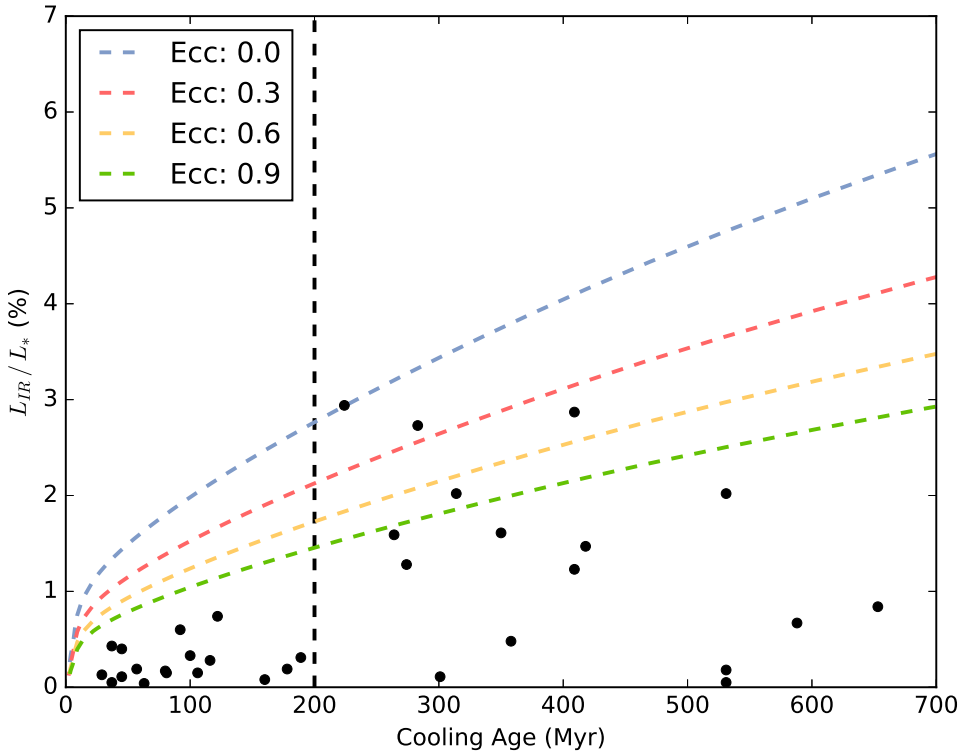

Figure 4.4: The distribution of fractional infrared luminosities compared with face-on disk models of increasing ellipticity.

4.1.2 Elliptical Dust Models Applied to the Whole Sample

Given the success of the elliptical dusty debris model in expanding the range of dusty debris parameters that fit the data without adjusting the inclination of the disk, we also applied this model to the trend of decreasing fractional infrared luminosity observed by Rocchetto et al. (2015). In Figure 4.4 we re-plot Figure 4.1 with additional models of increasing eccentricity using our elliptical dusty debris model. As expected, lines of increasing eccentricity have a reduced fractional infrared luminosity, and better approximate the maximum fraction infrared luminosity of the younger white dwarfs under the assumption that the disks fill all of the available orbital space and have randomly observed inclinations. As an alternative to the narrow rings interpretation, we propose that eccentricity could play a role in the difference between the younger and older sample of white dwarfs. Given that we know

the dusty material must begin on highly eccentric orbits, the difference between the older and younger samples on the fractional infrared luminosity plot could be explained by the younger disks hosting more frequent disruption events, and therefore having disks of higher mean eccentricity.

4.1.3 Caveats of Elliptical Dust Geometries

While it is true that the dust starts off on highly elliptical orbits just after disruption, most of the physical processes we associate with these dust disks seek to circularize material. Veras et al. (2015) recently demonstrated that when considering the evolution of an individual ring of particles under Poynting-Robertson drag alone, the dust can be expected to circularize in hundreds to tens of thousands of years for the younger white dwarfs in this sample. If the circularization timescale is short compared to the lifetime of the disk, we would not expect to observe many eccentric disks.

Furthermore, current observations of dusty debris disks around white dwarfs are insufficient to compare and contrast circular disks versus eccentric disks. As demonstrated in the top panel of Figure 4.2, models of increasing eccentricity only begin to diverge in shape at the wavelengths greater than 10μm, where constraints on dusty debris disks around white dwarfs are sparse. In fact, as of writing this thesis, only seven dusty debris disks have a photometric measurement beyond 10μm, and many of these measurements are contaminated with a strong silicate emission feature (Jura et al., 2009b), which prevents us from measuring the continuum flux at this point. The complex degeneracy between the best-fitted eccentricity, inclination, and outer radius of a dusty debris disk makes it difficult to draw any firm scientific conclusions without additional data.

Currently, there is no facility capable of measuring the faint emission expected from dusty debris disks around white dwarfs at these long wavelengths, but the soon to be launched James Webb Space Telescope offers promise with its suite of sensitive mid-infrared instruments. Until adequate data can be collected to differentiate between the elliptical and

circular dusty debris disk models, this work can serve as a proof-of-concept that eccentric dusty debris streams can be used to model the infrared excesses observed, and the degeneracies between best-fitted parameters must be carefully considered if any conclusions are to be drawn from this work.

4.2 Evolution of Dusty Debris Disks in the single temperature Blackbody Plane

It should come as no surprise that increasing the number of free parameters used to model the dusty debris disks, in the previous case introducing a free eccentricity, increases the degeneracy between parameters when the amount of information is held fixed. Here we consider an alternative strategy, what can we learn from the existing data on dusty debris disks if we decrease the number of free parameters used to model the infrared excess, opting instead for the single temperature blackbody as our physical model. In this way, every debris disk is modeled with just two free parameters, effective temperature and radius, and visualized on the same plane.

4.2.1 Ordering of Dust Disks Within the single temperature Blackbody Plane

Figure 4.5 shows an expanded region of Figure 2.9 with the single temperature blackbody fits to the dusty infrared excesses taken from Rocchetto et al. (2015). It is worth reiterating here that the disks themselves are not spherical, and the best fitted "radius" is a proxy for apparent surface area, which is affected by inclination and the inner/outer disk radius. In red diamonds with black outlines we highlight all of the literature identified systems within the Rocchetto et al. (2015) sample which also contain gaseous debris in emission. We also include our non-detections of gaseous emission, described in section 3.2 as filled grey diamonds. Open grey diamonds represent systems we have not yet surveyed.

Immediately one notices the dearth of dusty debris disks at high ($T_{eff} > 1500$K) and low ($T_{eff} < 750$K) effective temperatures. The lack of debris disks modeled by low effective temperatures could be a selection effect, as these disks are inherently fainter and more

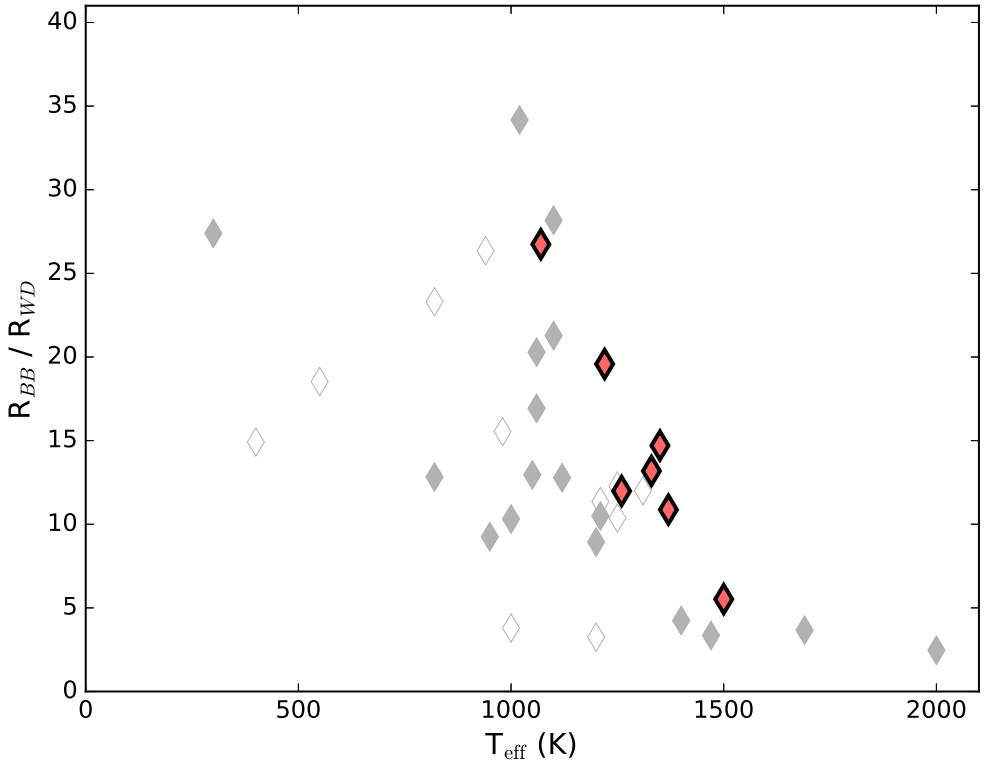

Figure 4.5: Location of all *Spitzer* confirmed dust disks as fitted with single temperature blackbodies by Rocchetto et al. (2015). Systems with observed Ca triplet emission are identified with red diamonds with black outlines, and systems where we found no evidence of Ca triplet emissions with our SOAR observations are shown as filled grey diamonds. Open diamonds are systems we have not yet followed-up for Ca triplet emission.

difficult to detect. In contrast, the lack of debris disks at higher temperature could reflect the physics of dust sublimation, as dust at temperature greater than $\approx$ 1800K is expected to sublimate into gas (Rafikov & Garmilla, 2012). This leads us to another interesting property of this figure which is that white dwarfs with gaseous debris in emission all lie along the terminus of the dusty white dwarf region of Figure 4.5.

Recalling our discussion of the literature on gaseous debris disks in subsection 1.3.2, circumstellar gaseous emission has been observed in the optical spectra of eight white dwarfs which also have dusty debris disks (Manser et al., 2016a). The gaseous debris is believed to be spatially coincident with the dusty debris (Melis et al., 2010), and the interaction between the gas and dust is likely to play large role in the evolution and accretion of the dust disk (Metzger et al., 2012), but no comprehensive theory has been developed as to why these eight dusty debris disks show gaseous debris in emission, while the others do not. In fact, there does not even exist a method to identify dusty systems which are likely to host gaseous debris in emission, as no single common property has been identified.

In the single temperature blackbody plane, the dusty debris disks with gaseous emission emission stand out as defining the high temperature boundary below which dusty debris disks can exist. In other words, for any projected surface area, the dusty disks with gaseous emission congregate at the highest temperatures. This is not terribly surprising as the high temperature side of the dust disk region should be defined by the dust sublimation temperature. It seems natural then that gas disks appear most frequently in systems with copious amounts of dust at the sublimation temperature.

Another interpretation is that for a given temperature the white dwarfs with gaseous debris host the largest, and therefore most luminous dusty debris disks. The observation that white dwarfs with gaseous and dusty debris tend to have brighter dusty debris disks is not novel (Farihi, 2016), but we find it particularly interesting in the context of the results from the dynamical modeling that has been performed on the emission profiles. Typically, high inclinations ($i > 60°$) are needed to reproduce the large velocity dispersion and deep

inner regions of the Ca emission profiles (Gänsicke et al., 2006, 2007; Melis et al., 2012). This is difficult to reconcile with the brightness of the infrared dusty components, as all other things considered equal, one would expect the low inclination, face-on dust disks to be the highest luminosity disks. The implication is that systems which host gaseous debris in combination with dusty debris may not display equivalent, flat geometry as those without gaseous debris. This could be expected if the gas was collisionally produced, perhaps during a recent disruption or collision with an existing disk as described in Jura (2008).

4.2.2 Population Synthesis of the Sample

Another method to extract information from the position of all the dusty debris disks in the single temperature blackbody plane is to generate a synthetic population of disks by drawing random values for the model input parameters and comparing the resulting sample of synthetic fits against the observed population. In this way, one can determine if the model represents a good fit to the bulk properties of the sample (as opposed to a single model fitting a single object), and also can probe which distributions of model parameters best represent the data. This type of study is called a population synthesis study, and in this section we will use it to search for trends that push systems towards the high-temperature boundary in a effort to uncover what qualifies a dusty system to host gaseous debris in emission.

To perform a population synthesis study, one first has to adopt a model, for which we choose the optically thick and circular dusty debris disk developed by Jura (2003) and discussed in subsection 1.3.1. In this model the flux from the debris disks is dependent on the white dwarf effective temperature, the white dwarf radius, the temperature of the inner edge of the dusty debris disk, the distance to the outer edge of the dusty debris disk, and the observed inclination of the debris disk.

Next, we need to determine what the appropriate distributions for drawing random values for each parameter will be. For the white dwarf effective temperature, we adopt the observed distribution of white dwarf effective temperatures for systems known to host dusty

debris. We also assume the mean white dwarf surface gravity, $\log g = 8.0$, setting the white dwarf radius. For the observed inclination of the debris disk we know that the inclination should be random, but since the debris disks can be inclined in two planes, the probability of drawing an inclination i is actually proportional to $\sin(i)$.

Finally, the appropriate distributions for the inner temperature and outer radius are unknown. We do however have some reasonable constraints. We know that the dust in the debris disk cannot survive above its sublimation temperature of around 1800K, and that it should always be greater than the temperature of the dust at the outer edge of the disk. We also know that the outer radius of the debris disk should have a maximum value corresponding to the tidal disruption radius, but it could lie anywhere within this maximum.

With all of these constraints in mind, we setup a monte-carlo simulation to randomly simulate white dwarf and circular dusty debris models, which we then fit with single temperature blackbody models to compare against the measurements, as shown in Figure 4.5. Our results are shown in terms of the four randomly draw parameters of interest (white dwarf effective temperature, disk inclination, inner disk temperature, and outer disk temperature) in Figure 4.6 with our models as colored dots and the measured dusty debris disk values as diamonds.

Examining the bulk distribution of our colored model points as compared to the observed systems in grey diamonds, we first note that they are broadly the same shape, with a mild slope forming the boundary at higher temperatures within which dusty debris disks exist. This indicates that our model choice for the dusty debris disks, the optically thick circular debris disk mode of Jura (2003) is reasonable. Examining the panels one-by-one, we can see a few trends develop among the different model parameter choices.

In the upper-left panel, we see that debris disks around white dwarfs with higher effective temperatures (pink/purple dots), are occasionally brighter, though with the proper combination of of inner disk temperature and inclination can still end up being fitted with low temperature and radius blackbody, well away from the high temperature gaseous boundary.

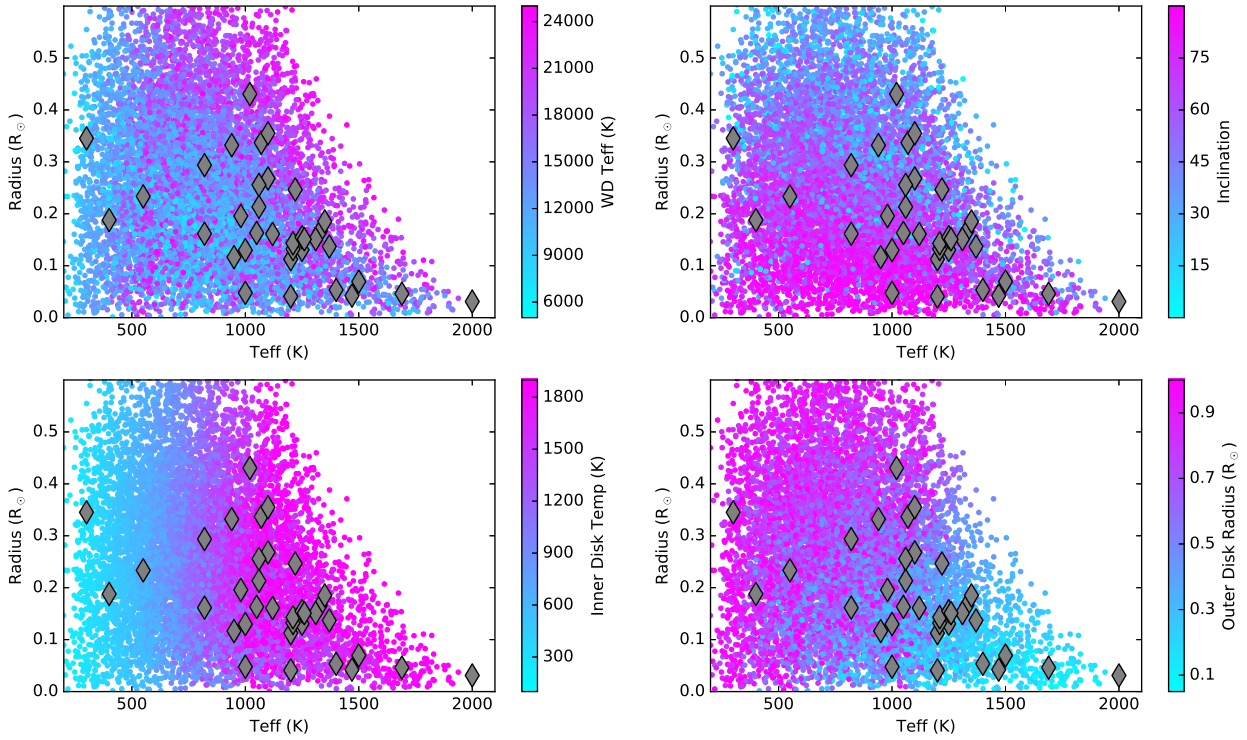

Figure 4.6: Single Temperature Blackbody Plane overplotted with randomly drawn sample of white dwarf plus dusty debris disk systems. This example population synthesis study of the region of the single temperature blackbody plane occupied by dusty debris disks demonstrates the potential of the technique to reveal bulk properties of the dusty debris disk sample.

Moving on to inclination in the upper-right panel, we see that adjusting the inclination of dusty debris disk with respect to the observer has the simple effect of moving a system up or down on the single temperature blackbody plane, with low inclination, face-on debris disks (in light blue) generally being the brightest systems.

In the lower-left panel, higher inner disk temperatures (pink/purple dots) result in higher effective temperature fits, creating a horizontal vector for systems to slide to the left or right in the plane. It is interesting to note that there are no model systems at the high temperature gaseous boundary with effective temperatures below 1000K, suggesting that gaseous emission does require at least some close-in dust, as opposed to just collisional gas production at a large distance. Finally, in the lower-right panel we see that compact disks with close-in outer radii (light blue), congregate at high effective temperatures and small radii, which makes sense as they will mostly be comprised of hot, close-in dust, with little cool dust at large radii.

While informative, none of the four parameters explored provide a direction of motion that is purely towards or away from the high temperature gaseous debris disk boundary. In other words, none of the vectors which describe the change in location of a model point with the change in a parameter of interest is perpendicular to the boundary. The inclination vector is purely vertical, the inner disk temperature horizontal, and the outer disk nearly parallel to the boundary. It is clear that none of these four parameters uniquely determine whether a dust debris disk system should host gaseous debris in emission. Instead, it is likely to be some combination of these or other parameters that makes the systems along the boundary unique, and informs the probability of hosting gaseous debris in emission.

4.2.3 Caveats for Continued Work

Though the shape of the dusty debris disk region is reproduced well by our synthetic population, it is worth pointing out that the distribution of points with respect to effective temperature is not. In Figure 4.7 we compare the histograms of both populations, modeled

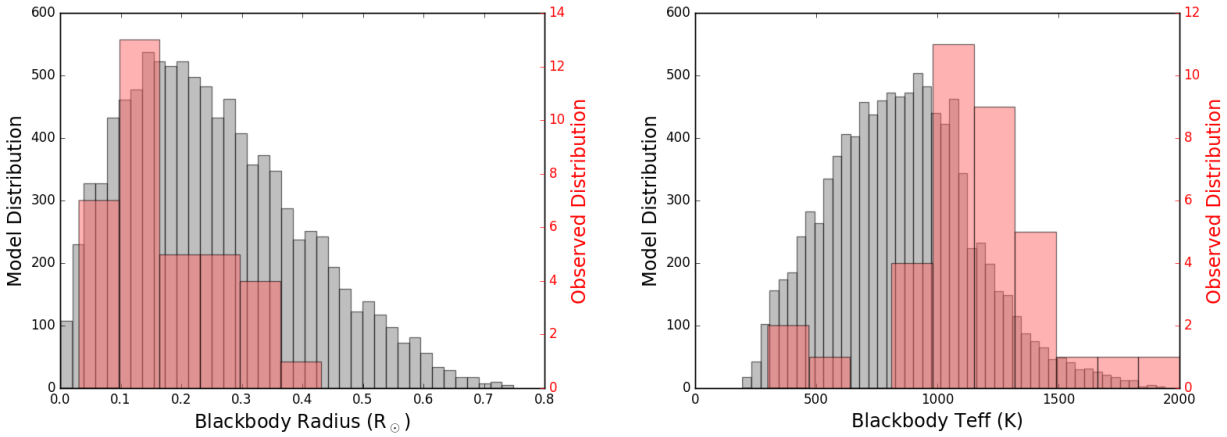

Figure 4.7: Single Temperature Blackbody Plane population synthesis histograms

in grey vs observed in red, along both axes, blackbody effective temperature and radius. The model distribution over-predicts the density of systems at low blackbody effective temperature, though this could be a selection effect as the thesis systems are inherently fainter and harder to observe. The same cannot be said however about the distributions of blackbody radius, where the model over-predicts the number of bright debris disks with a large projected area.

One way to address this issues is to adjust the distributions of selected parameters. For example, we could allow for smaller maximum outer radii in such a way that we select against systems with large amounts of cool dust, increasing the mean effective temperature of our blackbody sample and decreasing the size of the debris disks. Or we could consider an alternative model, such as with the eccentric debris disk models developed in section 4.1. We will discuss these options in the context of future work in chapter 5.

4.3 Rapid Variability in Emission Profiles of the Gaseous Debris around HE 1349–2305

While bulk studies of systems in various evolutionary phases such as the single temperature blackbody plane are useful, the best way to study the evolution of an astrophysical system is to search for signs of real-time variability. In section 3.4, we presented a discovery

of such a system with our observations of the emission profile variability in the gaseous debris disk around HE1349–2305. The morphological variability of the asymmetric emission profiles of HE 1349–2305 explored in section 3.4 mimics what has been seen in the gaseous debris disks surrounding WD 1226+110 (Manser et al., 2016b), WD 0845+2257 (Wilson et al., 2015), and WD 1043+0855 (Manser et al., 2016a), all of which have been observed to vary on 10-30 year timescales, though none have been observed over a complete cycle of variations. With the confirmation of variability in HE 1349–2305, five of the eight gaseous debris disks around white dwarf stars have undergone significant dynamical changes since their discovery (see Table 2 of Manser et al. 2016a). The shorter timescale makes HE 1349–2305 a challenging test case for theories of the variability.

The leading theory for the asymmetric emission profile variability is the precession of a fixed intensity pattern, which, for the case of WD 1226+110, has been well modeled with both elliptical (Manser et al., 2016b) and spiral-shape geometries (Hartmann et al., 2016). Manser et al. (2016b) further demonstrated that the rate of the gaseous emission profile variability roughly matches the rate expected from the general relativistic precession of mildly eccentric orbits near the midpoint of the debris disk. This interpretation can be similarly applied to the variations observed in the emission profiles of WD 0845+2257 and WD 1043+0855 (Manser et al., 2016a), but fails in the case of HE 1349–2305. As an alternative, we consider whether the propagation of global density waves could explain both the yearly timescale seen in our observations and the decadal timescales observed in other gaseous emission systems.

4.3.1 General Relativistic Precession

A key component of general relativistic precession is that the timescale is strongly dependent on the orbital radius. In the case of WD 1226+110, the precession timescales range from 1.5 years at the inner edge of the disk to 134 years at the outer edge of the disk, and it is near the midpoint of the disk that the expected precession due to general relativity of 27.8 years matches the observed 24-30 year variations of the emission profiles (Manser et al.,

2016b).

The radial extent of the debris disk in HE 1349–2305 is not as well constrained as in WD 1226+110, but we do have a few reasonable expectations for its inner and outer boundaries. Modeling the gaseous emission lines as optically thick line profiles, Melis et al. (2012) find the outer radius of the gaseous debris to be near 100 white dwarf radii, and the inner radius, well constrained by the maximum observed velocity of the emission lines, to be between 15 and 20 white dwarf radii depending on inclination. These inferred inner and outer radii also match the physical expectations for the boundaries of tidally disrupted debris disks around white dwarfs, where the outer edge corresponds to the tidal disruption radius and the inner edge is set by the dust sublimation radius (Farihi, 2016).

Following the Manser et al. (2016b) analysis of WD 1226+110 and adopting a white dwarf mass of 0.67 $M_{\odot}$ as determined spectroscopically by Melis et al. (2012), in the limit of small eccentricities we find the precessional period due to general relativity at the midpoint of the disk at 60 R_{WD} to be 37.2 years, far too long to explain the 1.4 year variations observed. In order to match the 1.4 year period observed, the emitting gaseous debris would have to be concentrated at 16 R_{WD}, which is inconsistent with the extent of the gaseous debris as modeled by Melis et al. (2012).

If we relax the assumption of small eccentricity, we can ask at what eccentricity does the precessional period expected from general relativity match the expected midpoint of the debris disk? The eccentricity required for orbits at the midpoint of the disk to precess at 1.4 years is $e = 0.998$, which would carry material from the inner edge of the debris disk at 20 R_{WD} all the way out to $\approx$ 1AU. Such an extremely eccentric orbit is not unexpected at the formation of the tidally disrupted dust rings (Veras et al., 2014b), but it is unknown how long such an eccentricity could be sustained under the effects of Poynting-Roberston drag and collisional cascades (Veras et al., 2014b; Kenyon & Bromley, 2017a).

Furthermore, we have additional independent geometric constraints on the eccentricity

from the observed infrared excess if we assume the dust and gas are co-orbital. This assumption is justified as differences in the eccentricity of the orbits of the dust and gas can lead to runaway accretion scenarios which rapidly deplete the debris disk (Metzger et al., 2012). Using the elliptical dust ring models developed in section 4.1, we modeled the infrared excess with extremely eccentric rings ($e > 0.9$) and find that they require a near face-on configuration, which contradicts the expected inclination of the gaseous debris as modeled by Melis et al. (2012). Therefore, it is not feasible for the dust and gas to be both co-planar and highly eccentric.

In summary, in order for general relativistic precession to explain the observed timescale of emission profile variations the emitting gaseous material would need to be concentrated in a narrow ring between 16 and 20 R_{WD}. Such a compact gas distribution would contradict the previous modeling efforts of the gaseous debris by (Melis et al., 2012), who find that it should extend out to ≈ 100 R_{WD}. Given this disagreement, we find it unlikely for general relativistic precession to explain the 1.4 year variations observed in HE 1349–2305 unless the emission profiles can equivalently be modeled with a narrow, inner ring of gas. It is worth noting that if the emission profiles are found to be well modeled by a narrow, inner ring of gas, it could mean that HE134–2305 is in a unique state of evolution, as the gaseous debris in other white dwarf debris disks has been found to extend much further and completely overlap with the dusty debris (Melis et al., 2010).

4.3.2 Global Density Waves

As an alternative to general relativistic precession, we propose the evolution of the emission line profiles could be governed by the propagation of global density waves within the gaseous debris disk, and dominate the emission of the gaseous debris. By global density waves, we mean any non-axisymmetric density perturbations that propagate through the gaseous disk, such as spiral density patterns observed in the direct imaging of protoplanetary disks (e.g. Pérez et al. 2016), or the precessing, elliptical density distributions used

to explain emission profile variability in B[e] stars (Okazaki, 2016). Pattern speeds of these density perturbations can depend on viscosity prescriptions, mechanisms responsible for excitation, and geometric constraints, and thus offer greater flexibility than general relativistic precession.

Spiral density waves observed in protoplanetary disks are often interpreted as evidence of disk-planet interactions with unseen, perturbing bodies (Fung & Dong, 2015). For spiral density waves excited by external perturbers on circular orbits, the pattern speed of the wave is expected to match the orbital frequency of the perturber, meaning the variations we have observed would correspond to a perturbing body at a distance of 1-2 AU. Given that the debris disk is completely contained within 1 $R_{\odot}$, a perturbing body at this distance should have little to no effect on the disk. It is worth noting however that spiral density waves can also be excited by recent flyby events, or perturbing bodies on highly eccentric orbits (Dong et al., 2015), though hydrodynamical simulations would be needed to place constraints on these interactions, which is beyond the scope of this paper.

Simulations of turbulence in generalized accretion disks have also shown that disk instabilities such as the magneto-rotational instability readily excite spiral density waves (Heinemann & Papaloizou, 2009a,b). The propagation speed of these waves is coupled to the local sound speed of the gas, though there is some dependence on whether the density waves are treated with non-linear effects (Heinemann & Papaloizou, 2012).

Though their excitation mechanism is largely unknown (Okazaki, 2016), the one-armed density waves proposed to explain the emission profile variability of the disks observed in B[e] stars offer a more directly analogy to our observations, and similarities between the asymmetric emission profiles observed in B[e] stars and the gaseous debris disks around white dwarf stars were first noted by Gänsicke et al. (2006). The timescales observed for emission profile variations in B[e] stars range in period from years to decades, which, similarly to the debris disks around white dwarf stars, is several orders of magnitude longer than the orbital timescales of particles within the disks (Okazaki, 1991). There is observational evidence that

longer emission profile variations correspond to larger disks (Reig et al., 2005), though the data suggest the radial dependence of this effect is less dramatic than general relativistic precession.

4.3.3 Difficulties with Global Density Wave Interpretation

The challenge to this interpretation is likely to be whether density waves can survive long enough to explain the observed variations, particularly given the interactions between the gaseous and dusty debris, which are believed to be spatially coincident (Melis et al., 2010). If the gas and dust are strongly coupled, density enhancements in the gaseous debris could be rapidly suppressed. Attempts to model this interaction in the environments around white dwarf stars have shown that strong coupling between the gas and dust leads to runaway accretion events which rapidly deplete the debris disk (Metzger et al., 2012). This runaway accretion occurs on timescales shorter than the baseline over which some gaseous debris disks have been observed to vary (Manser et al., 2016b), suggesting the coupling in these disks is relatively weak. Continued driving of the density enhancements could also allow them to survive in the presence of damping. These caveats point towards a clear need for tracing the evolution of the period of the emission profile variations over multiple cycles, which we discuss in the context of future work in chapter 5.

4.4 Significance of Results

The elliptical dusty models we have introduced in this section can be applied to all dusty debris disk hosting white dwarfs as an alternative to the circular models previously used. Their utility is currently limited by the lack of mid-infrared observations where the circular and dusty models diverge, but future studies with the James Webb Space Telescope should provide the observations necessary to distinguish between the two models. In the meantime, these models can be used to test specific scenarios around individual systems, such as how we used them in section 4.3 to rule out the possibility of having a co-aligned disk of highly

eccentric gas and highly eccentric dust.

The identification of the gaseous debris disk hosting white dwarfs as forming a boundary on the single temperature blackbody plane is new and exciting as there is no previous work that isolates the dusty systems which host gaseous debris in such a way. The population synthesis technique we applied to explore the parameters which lead to dust disks arriving at this boundary is just one example of how the single temperature blackbody plane can be used to study the evolution of the dusty debris disks around white dwarfs.

Finally, the identification of the rapid emission profile variations observed in HE 1349–2305 as problematic for the current understanding of eccentric gaseous debris precessing due to general relativistic effects opened the door to a new spiral density wave interpretation for the profile variations. We argue that the precession of spiral density waves could explain both the long and short term emission profile variations and that the general relativisic precession of an eccentric disk cannot, calling into question the mechanism for emission profile variability. Future studies should be open to considering both possibilities, and others not yet explored, when considering the evolution of the gaseous debris in these systems.

CHAPTER 5: CONCLUSIONS & FUTURE OUTLOOK

As demonstrated in this thesis, there are two primary methods in which the remnant exoplanetary debris disks around white dwarfs can be observed: the infrared radiation emitted by the dusty component of the debris disk and the double-peaked emission lines that originate from the gaseous component of the debris disk. We have presented new observations and interpretations of the debris disks using both, and in this final section we summarize our accomplishments, their current impact on the field, and future directions they enable.

5.1 Results in Dusty Exoplanetary Debris

The sample size of dusty debris disks around white dwarfs has only recently reached the point such that trends in the sample can be revealed (e.g. Rocchetto et al. (2015)), but the sample is not yet large enough to draw firm, statistical conclusions. Continued discovery is needed to enable these and future studies.

Our discoveries of thirteen new dusty debris disk candidates have the potential to increase the sample of known dusty debris disk hosting white dwarfs by more than 25% with appropriate follow-up. Each new discovery also offers the promise of a detailed exoplanetary abundance study that has the potential to reveal new classes of rocky exoplanetary bodies, such as the unique calcium to magnesium ratio we discovered in the atmosphere of EC 05365–4749. The atmospheres of white dwarf stars offer the only avenue to study rocky exoplanetary compositions in such detail (Jura & Young, 2014), and the new systems we have discovered provide opportunities to do so over the next few years.

On a more general note, the techniques we have pioneered to discover such systems, notably the single temperature blackbody technique, are robust against poor or mixed quality

photometric data samples. This technique will immediately be applicable to searches for infrared excesses around the tens of thousands of new white dwarfs expected to be discovered by GAIA (Gänsicke et al., 2016a). Application of our single temperature blackbody technique will accelerate the prioritization of follow-up of new dusty debris disk candidates from the GAIA sample, which has the potential to increase the number of known dusty white dwarf systems by an order of magnitude.

Our attempts to model the observed infrared excesses as both elliptical rings and single temperature blackbodies each provided new interpretations for the evolution of dusty debris disks. The application of elliptical debris streams could explain the observed trend of fainter debris disks around younger white dwarfs as being more eccentric due to more recent formation. The organization of the known dusty debris disk systems on the single temperature blackbody plane provides an opportunity for population synthesis studies to quickly uncover bulk properties of the sample. Continued study of the elliptical debris model awaits future observatories capable of mid-infrared photometry, and though the population synthesis work is immature, we have laid out the foundation for future studies to build-upon.

5.2 Results in Gaseous Exoplanetary Debris

The addition of the new Red Camera to the Goodman Spectrograph was largely motivated by the desire for continued follow-up of gaseous debris disks and our comprehensive observations of the known gaseous debris disk hosting systems demonstrate its effectiveness. For three systems, we have observed no changes in the emission profiles over baselines of 5-8 years, and the observations presented here can be referenced by future variability studies searching for decadal length variations. In our observations of HE1349–2305, we have discovered rapid emission profile variations, which occur a on timescale more than an order of magnitude shorter than its counterparts, challenging the current theories for the emission profile evolution.

We argue that these rapid emission profile variations require a new driving mechanism to

replace the interpretation of the general relativistic precession of an eccentric disk. The new theory must be capable of explaining both the short term variations we have observed and the longer variations seen by other groups. We considered the application of global density waves in analogy with what is seen in proto-planetary disks among others, and show that the observations are so far consistent with this theory. We have also given recommendations for future observations to test these theories.

Finally, the identification of the dusty debris disks which also host gaseous debris in emission as forming the terminus of dusty debris disks in our single temperature blackbody plane provided the first direct indication that there is a unique property associated with the dusty debris in these systems that results in the gaseous emission. We have provided a first attempt to uncover this property using population synthesis techniques, but fail to identify a single common parameter among those explored.

5.3 The Path Forward

5.3.1 Follow-up of New Candidates

One of the next steps which should be taken to advance this work is the follow-up of the new dusty debris disk candidates revealed in section 2.2, at same the level of detail which we followed-up EC05365–4749 in section 2.1. This includes high resolution spectroscopic observations to search for signs of atmospheric accretion and high spatial resolution near-infrared imaging to search for potential nearby contaminants that could be contributing to the observed infrared excess. If the candidates are suitably bright for study with the Hubble Space Telescope (HST), ultra-violet spectra should be collected to perform comprehensive abundance analyses of the accreted material for comparison with known solar system objects. HST observations of EC 05365–4749 have already been collected by another research group and the analysis is pending. Given the unique calcium to magnesium ratio we discovered in the optical spectra, we suspect that the detailed abundance analysis will reveal the past

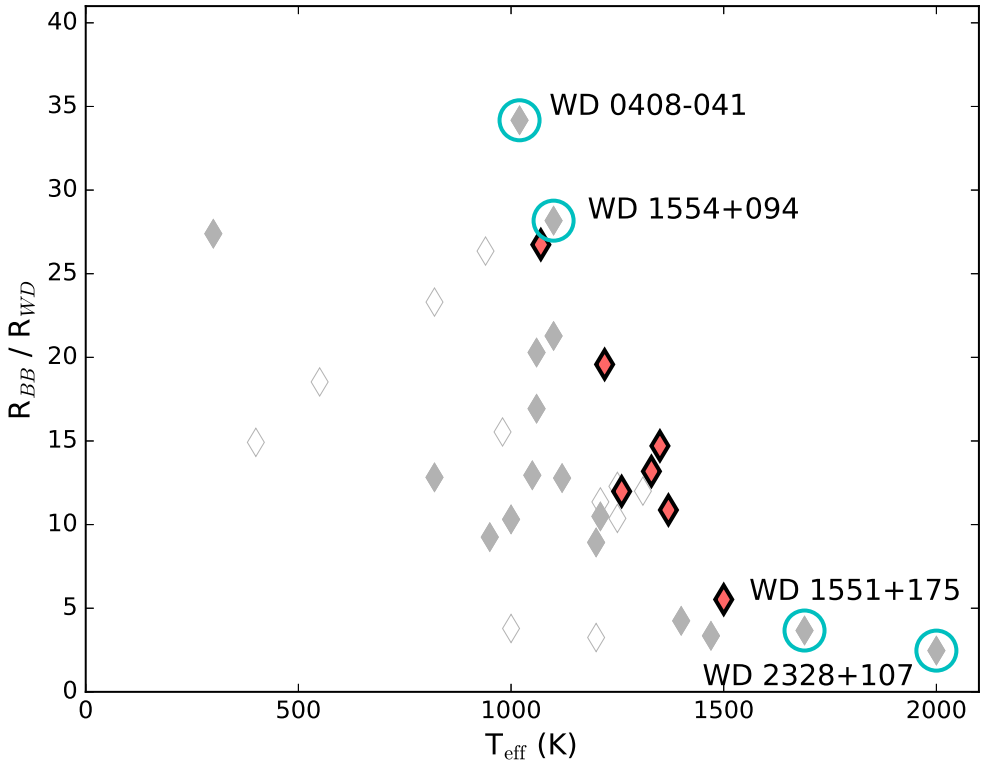

Figure 5.1: Peculiar systems in the single temperature blackbody plane.

accretion of a rocky object unlike what has been seen in other white dwarf atmospheres.

5.3.2 The Single Temperature Blackbody Plane

The single temperature blackbody selection technique is well-suited to handle searches for infrared excesses around large samples of white dwarfs, and should prove useful for the upcoming studies of the GAIA white dwarf sample. However, the organization of the dusty white dwarf systems in the single temperature blackbody plane, and the identification of the systems with gaseous debris in emission as forming the high temperature boundary offers greater promise to impact our understanding of the evolution of such systems.

The single temperature blackbody plane enables for the first time a prediction of whether a system should have gaseous debris in emission. Prior discoveries of gaseous emission line systems have relied entirely on serendipitous discovery, but the identification of new dusty white dwarfs from the GAIA sample which lie along the boundary should be targeted directly

for gaseous emission. On that note, it is worth addressing a few of the systems which lie along the boundary and do not show gaseous debris in emission. We highlight and label these systems in Figure 5.1.

The first is WD 1554+094, which is best-fitted by a blackbody with an effective temperature of 1100K and near the top of the dusty region. This system was recently revealed to be a compact binary system, with a white dwarf primary and L-dwarf secondary by Farihi et al. (2017). The authors find that the L-dwarf contributes to the infrared excess observed, but that there must be a circumbinary dust disk to completely account for the infrared brightness of the system. In the single temperature blackbody plane this object lies along the boundary, but likely due to the flux of the L-dwarf star, not the dusty debris disk, so it should not necessarily be expected to host gaseous emission. This does however provide another example of how the single temperature blackbody technique can reveal systems of interest, as the circumbinary disk around WD 1554+094 was one of the first discovered (Farihi et al., 2017).

This brings us to WD 0408-041, which is best-fitted with a blackbody effective temperature of 1020K and is even brighter than WD 1554+094. Despite obtaining very high signal-to-noise spectra, we find no evidence of gaseous emission in this system. Furthermore, near-infrared spectroscopic studies show no evidence of a sub-stellar companion (Kilic et al., 2006) such as what was found around WD 1554+094. In the absence of a stellar companion and gaseous emission, the brightness of the inferred dusty infrared excess around WD 0408-041 is truly unique. One explanation is that the additional brightness is the signature of a recent disruption event, and we have caught the system in a temporary bright state. Given the recent detection of the active disruption of the planetesimal around WD 1145+017 discussed in subsection 1.3.3, we know that it is possible to capture such transient states, and future studies should target WD 0408-041 for near-infrared variability.

The two systems identified in the lower-right hand corner of Figure 5.1, WD 1551+175 and WD 2128+107 exhibit much more subtle infrared excesses than those around WD

1554+094 and WD 0408-041, and could possibly be the result of a nearby, unresolved contaminant such as what we discovered around PG 14572-086 in section 2.2.3. These systems should be studied at high-spatial resolution to confirm whether the observed infrared excess is truly associated with the white dwarf.

By applying this tool to the dusty white dwarf sample expected from GAIA, we expect to be able to predict the systems which should have gaseous debris in emission for the first time, and in cases where no emission is found, closer analysis may reveal additional systems like WD 1554+094.

5.3.3 Gaseous Emission Profile Variability

Our discovery of a new timescale for yearly variability in the gaseous emission profiles of HE 1349–2305 has already begun to inform theoretical studies of debris disk variability. Three weeks after our observations of HE 1349–2305 were made public, a new study examining the global precession timescales expected under general relatvisitc precession was published on the arXiv, including a full hydrodynamic treatment of the general relativistic precession of a fluid disk. Previous analyses, including our own, were done under the assumption of point-like particle precession, which neglects the hydrodynamical effects of the evolution of coupled gas particles. Miranda & Rafikov (2018) demonstrate that with a proper fluid treatment, general relativistic precession could explain the long and short timescales if the inner edge of the gaseous debris in HE 1349–2305 is significantly inside of the inner edges of the gaseous debris around WD 1228+110. Such a scenario is not ruled out by current observations, and revives the theory that the emission profile variations could be the result of a precessing, eccentric gaseous disk.

5.3.4 Closing Remarks

When considering the interpretation of gaseous emission profile variations as precessing eccentric disks in addition to the eccentric dusty models we explored in section 4.1, it is

reasonable to conclude that the work in this thesis points towards the remnant exoplanetary debris disks around white dwarf stars as necessarily elliptical disks. I caution the reader against such an interpretation. Extending our models of these debris disks to include elliptical geometries is a logical first step away from simple circular models, but an all-encompassing solution for these incredibly diverse and dynamic systems is always destined to fail.

The true nature of these systems is certain to be complex and surprising to our imagination, and the observations and techniques presented in this thesis work provide just one step of many. The take-away from this work should therefore be the importance of never becoming too comfortable with the current state of explanations. With each new observation we should not consider the ways in which the data supports existing ideas, but the ways it challenges them, including the ones presented in this thesis.

APPENDIX A: ECXWIRED TABLES

In this appendix, we present the ECxWIRED infrared excess candidates, separated by Region Classification as detailed in section 2.2.

Table A.1: Region I: Dusty White Dwarf Candidates.

EC Name	Right Ascension (J2000)	Declination (J2000)	V (mag)	EC Sptype	WD T_{eff} (K)	WD $\log g$ (cm^{-2})	BB T_{eff} (K)	BB Rad (R_{WD})	Im Flag	Ref
New Candidates:										
00169-2205	4.8676032	-21.817987	15.33	DA	13264.0[a]	7.78[a]	1675.0	2.0	20	1
01071-1917	17.3880821	-19.0216157	16.16	DA	14304.0[a]	7.79[a]	537.5	39.0	10	1
01129-5223	18.7553121	-52.1286677	16.47	DA	22000.0	8.0	1725.0	5.0	00	1
02566-1802	44.7483175	-17.8387548	16.51	DA	26212.0[a]	7.76[a]	575.0	49.0	10	1
03103-6226	47.8357894	-62.2545421	16.05	DA	16000.0	8.0	1050.0	11.0	00	1
05276-4305	82.3005907	-43.0595245	16.10	DA	13000.0	8.0	1150.0	5.0	00	1
13140-1520	199.1818104	-15.5976591	14.86	DA3	16152.0[a]	7.72[a]	1862.5	3.0	20	1
20036-6613	302.099844	-66.0769588	15.91	DA	24250.0	8.0	1500.0	8.0	20	1
21010-1741	315.9666489	-17.4904601	16.57	DA	18750.0	8.0	975.0	13.0	01	1
21548-5908	329.5997382	-58.8983987	15.75	DA	12000.0	8.0	1037.5	9.0	00	1
23379-3725	355.1531593	-37.1454489	16.18	DA	13250.0	8.0	837.5	18.0	00	1
Previously Identified:										
04203-7310	64.9071296	-73.0622893	15.61	DA	19000.0	8.0	1125.0	19.0	20	2
05365-4759	84.473051	-47.9679045	15.63	DA	22250.0	8.0	1037.5	16.0	01	3

Continued on next page

EC Name	Right Ascension (J2000)	Declination (J2000)	V (mag)	EC Sptype	WD T_{eff} (K)	WD $\log g$ (cm^{-2})	BB T_{eff} (K)	BB Rad (R_{WD})	Im Flag	Ref
11507-1519	178.3133581	-15.6099161	16.00	DA5	12132.0[a]	8.03[a]	862.5	31.0	20	4
21159-5602	319.9006626	-55.8370306	14.27	DA	9625.0[a]	8.01[a]	900.0	10.0	00	5
22215-1631	336.0727067	-16.263386	15.45	DA	9937.0[a]	8.16[a]	925.0	6.0	00	6
Rejected Candidates:										
00323-3146	8.7072847	-31.4978588	16.09	DAwk	36965.0[a]	7.19[a]	1225.0	11.0	10	1
04114-1243	63.4385557	-12.5944927	16.70	DA	50000.0	8.0	1500.0	16.0	20	1
04139-4029	63.9157837	-40.3757732	16.23	DA	43000.0	8.0	825.0	83.0	01	1
04516-4428	73.3031017	-44.394365	15.35	DA	16750.0	8.0	662.5	92.0	01	1
04552-2812	74.3051311	-28.1312704	13.98	DAwk	54386.0[a]	7.68[a]	1975.0	4.0	20	7
05024-5705	75.8461981	-57.0227396	16.22	DA	44000.0	8.0	1237.5	14.0	01	1
11023-1821	166.1945881	-18.6200168	15.99	DA5	8057.0[a]	7.85[a]	962.5	4.0	20	8
12303-3052	188.2520412	-31.1432902	15.81	DA2	22764.0[a]	8.28[a]	1150.0	6.0	20	1
19442-4207	296.9186198	-42.0074873	10.38	CV/DAe	9500.0	8.0	1325.0	5.0	01	9

Continued on next page

EC Name	Right Ascension (J2000)	Declination (J2000)	V (mag)	EC Sptype	WD T_{eff} (K)	WD $\log g$ (cm^{-2})	BB T_{eff} (K)	BB Rad (R_{WD})	Im Flag	Ref

Table A.1: References: (1) Dennihy et al. (2017a); (2) Hoard et al. (2013); (3) Dennihy et al. (2016); (4) Kilic & Redfield (2007); (5) von Hippel et al. (2007); (6) Farihi et al. (2010); (7) Dobbie et al. (2005); (8) Farihi et al. (2008); (9) O'Donoghue et al. (2013). Under the column Im Flag, the first bit refers to the quality of imaging, with objects that have VHS K_s band-images receiving a 0, VST-ATLAS z band images a 1, and those without follow-up images a 2. The second bit refers to the potential for contamination. Objects which appeared as single stars were assigned a 0, those with one or more potential contaminants within the 7.8", circle were assigned a 1. Footnote[a] denotes spectroscopic parameters from Koester et al. (2009).

Table A.2: Region 2: White Dwarf with Stellar Excess Candidates.

EC Name	Right Ascension (J2000)	Declination (J2000)	V (mag)	EC Sptype	WD T_{eff} (K)	WD $\log g$ (cm^{-2})	BB T_{eff} (K)	BB Rad (R_{WD})	Im Flag	Ref
New Candidates:										
00050-1622	1.8951187	-16.0922234	16.29	DA	15141.0[a]	7.59[a]	2837.5	6.0	10	1
00166-4340	4.775084	-43.4051481	15.53	DA	7250.0[a]	8.0[a]	2812.5	6.0	00	1
00286-6338	7.7279283	-63.3624649	15.23	DA	19750.0	8.0	3225.0	10.0	00	1
00370-4201	9.8542309	-41.7470551	16.37	DA	10750.0	8.0	3875.0	1.0	00	1
00594-5701	15.3797183	-56.7644763	16.55	DA	13000.0	8.0	3187.5	9.0	00	1
01077-8047	17.0733956	-80.5236636	14.47	DA	5500.0	8.0	2912.5	4.0	20	1
01176-8233	19.3494814	-82.3011543	16.43	DA	17750.0	8.0	3737.5	17.0	20	1
01346-4042	24.2001527	-40.4593443	16.36	DA/DAB	13500.0	8.0	2950.0	17.0	00	1
02223-2630	36.1504952	-26.2812935	15.68	DA	23198.0[a]	7.91[a]	2087.5	6.0	10	2
02434-1254	41.4726889	-12.7056873	15.05	DA	29250.0	8.0	3275.0	11.0	10	1
03155-1747	49.4484126	-17.601521	16.48	DA	22750.0	8.0	2875.0	32.0	10	1
03378-8348	53.0676708	-83.6389586	16.24	DA	36750.0	8.0	3387.5	11.0	20	1
04094-3233	62.838107	-32.4373756	16.01	DA	18250.0[a]	8.0[a]	3037.5	16.0	20	1
04233-2822	66.3363893	-28.255434	16.48	DA	10907.0[a]	8.07[a]	2087.5	6.0	20	1

Continued on next page

EC Name	Right Ascension (J2000)	Declination (J2000)	V (mag)	EC Sptype	WD T_{eff} (K)	WD $\log g$ (cm^{-2})	BB T_{eff} (K)	BB Rad (R_{WD})	Im Flag	Ref
04310-3259	68.2266693	-32.8872894	17.6	DA	3750.0	8.0	2600.0	2.0	20	1
04365-1633	69.6966934	-16.4545871	16.03	DA	14092.0[a]	7.96[a]	2825.0	2.0	20	1
04567-2347	74.714622	-23.7150737	16.62	DA	23645.0[a]	7.79[a]	3175.0	5.0	20	1
05089-5933	77.4280658	-59.4939338	15.78	DA	28500.0	8.0	3750.0	61.0	00	1
05230-3821	81.1923171	-38.3099344	16.55	DA	18250.0	8.0	2712.5	11.0	20	1
05237-3856	81.3667125	-38.903283	16.17	DA	15750.0[a]	8.0[a]	2937.5	15.0	20	1
05387-3558	85.1301338	-35.9572189	13.97	DA	13250.0	8.0	3925.0	2.0	20	1
05430-4711	86.09625	-47.1715794	15.97	DA	8000.0	8.0	2650.0	9.0	00	1
12204-2915	185.7709471	-29.5410766	15.79	DA3	17702.0[a]	7.89[a]	2387.5	2.0	20	1
13123-2523	198.7660094	-25.6497229	15.69	DA1	75463.0[a]	7.68[a]	3425.0	17.0	20	1
13324-2255	203.7936553	-23.1771076	16.30	DA3	20264.0[a]	7.86[a]	2125.0	6.0	20	1
14265-2737	217.3638143	-27.8498806	15.92	DA3	18087.0[a]	7.66[a]	3062.5	2.0	20	1
14361-1832	219.744523	-18.7615606	16.56	DA?	29250.0	8.0	3737.5	8.0	20	1
19272-7152	293.2369964	-71.7669411	15.92	DA	20250.0	8.0	3525.0	12.0	20	1
20453-7549	312.7909386	-75.6400976	16.05	DA	25750.0	8.0	2500.0	3.0	20	1
20503-4650	313.4347278	-46.6575692	15.76	DAwk	19250.0	8.0	4100.0	10.0	01	1

Continued on next page

EC Name	Right Ascension (J2000)	Declination (J2000)	V (mag)	EC Sptype	WD T_{eff} (K)	WD $\log g$ (cm^{-2})	BB T_{eff} (K)	BB Rad (R_{WD})	Im Flag	Ref
21053-8201	318.3144577	-81.8191237	13.63	DA	10600.0[a]	8.24[a]	3587.5	1.0	20	1
21105-5128	318.4991085	-51.2753573	16.68	DA	16500.0	8.0	3262.5	4.0	01	1
21161-2610	319.7694033	-25.9702383	16.10	DA	24750.0	8.0	3400.0	2.0	01	1
21188-2715	320.4373582	-27.0364774	15.16	DA	5250.0	8.0	2625.0	6.0	20	1
21335-3637	324.162532	-36.4000738	15.73	DA	26940.0[b]	7.75[b]	3725.0	2.0	10	1
21459-3548	327.2267922	-35.5801944	16.35	DA	12000.0	8.0	2400.0	3.0	11	1
21470-5412	327.6000537	-53.9776573	15.26	DA	11500.0	8.0	2875.0	23.0	00	1
21473-1405	327.5153847	-13.8626911	15.75	DA	22250.0[a]	8.0[a]	3025.0	30.0	00	1
22016-3015	331.1442181	-30.0183606	15.58	DAe	12750.0	8.0	2762.5	31.0	10	1
22158-2027	334.6492133	-20.2113139	16.00	DA	15500.0	8.0	3750.0	2.0	20	1
23016-4857	346.12937	-48.6825705	15.58	DA	4750.0	8.0	2862.5	2.0	00	1
23227-6739	351.4332031	-67.3785049	16.71	DAwk	31500.0	8.0	2900.0	9.0	20	1
Previously Identified:										
00370-6328	9.8125271	-63.2073005	15.82	*DAe sdB+G	50000.0	8.0	3175.0	41.0	00	3,4
01162-2310	19.6547306	-22.9156167	16.15	DA	31990.0[b]	7.63[b]	3225.0	20.0	11	5
01319-1622	23.6002247	-16.1189799	13.94	DA	50110.0[a]	7.87[a]	3337.5	18.0	10	5

Continued on next page

EC Name	Right Ascension (J2000)	Declination (J2000)	V (mag)	EC Sptype	WD T_{eff} (K)	WD $\log g$ (cm^{-2})	BB T_{eff} (K)	BB Rad (R_{WD})	Im Flag	Ref
01450-2211	26.8410187	-21.9475691	14.85	DA(Z)	11747.0[a]	8.07[a]	2387.5	5.0	10	5
01450-7035	26.5471352	-70.339152	15.77	DA	19000.0	8.0	3375.0	6.0	20	5
02083-1520	32.6787961	-15.1095691	15.19	DA+dM	22620.0[b]	7.92[b]	3250.0	28.0	11	5
03094-2730	47.888501	-27.3236914	15.70	DA ?	56610.0[b]	7.53[b]	3712.5	40.0	10	5,6
03319-3541	53.4679871	-35.5210623	14.38	DA+dMe	23000.0[a]	8.0[a]	3200.0	31.0	10	4,5
03338-6410	53.643096	-64.0156465	14.32	DA	50000.0	8.0	3050.0	34.0	20	7
03479-1344	57.5607475	-13.5872177	14.96	DA	14250.0[a]	7.76[a]	2862.5	23.0	11	5
03569-2320	59.7703036	-23.2070023	15.87	DAwk	74710.0[b]	7.86[b]	3625.0	17.0	11	5
10150-1722	154.3701471	-17.6187202	16.77	DA4	32370.0[b]	7.58[b]	4075.0	15.0	20	5,6
12477-1738	192.5921204	-17.9129074	16.20	DA+dMe	21620.0[a]	8.16[a]	3287.5	27.0	20	5,8
12540-1318	194.1649138	-13.5783955	16.04	DA2	23710.0[b]	7.92[b]	3325.0	14.0	20	5
13077-1411	197.5938438	-14.4525458	16.44	DA4	26400.0[b]	7.92[b]	3737.5	25.0	20	5,6
13198-2849	200.6679344	-29.0922276	15.99	DA+dM	16620.0[a]	7.75[a]	2925.0	34.0	20	5,8
13349-3237	204.4613066	-32.872784	16.34	hot DA? sd?	7000.0[a]	8.0[a]	3262.5	4.0	20	9
13471-1258	207.4669075	-13.2272276	14.80	DA+dM	3000.0[a]	8.0[a]	2612.5	2.0	20	8
14329-1625	218.9405799	-16.63817	14.89	DA+dMe	16500.0[a]	8.0[a]	2837.5	27.0	20	8,9

Continued on next page

EC Name	Right Ascension (J2000)	Declination (J2000)	V (mag)	EC Sptype	WD T_{eff} (K)	WD $\log g$ (cm^{-2})	BB T_{eff} (K)	BB Rad (R_{WD})	Im Flag	Ref
14363-2137	219.8024563	-21.8369585	15.94	DA6	23690.0[a]	7.91[a]	3225.0	31.0	20	5
20220-2243	306.2477455	-22.5559774	16.45	DAwk/cont	50000.0	8.0	2200.0	12.0	20	10
20246-4855	307.0651962	-48.7608551	15.69	DA+dM	16250.0	8.0	3175.0	31.0	00	11
21016-3627	316.1957085	-36.2570282	16.79	DA	50000.0	8.0	4137.5	26.0	20	5
21083-4310	317.9062002	-42.9697055	15.77	DA	7750.0	8.0	2787.5	10.0	00	5
21384-6423	325.593066	-64.1624192	15.87	DA+dMe	17750.0	8.0	2962.5	30.0	01	3,4
22049-5839	332.0912832	-58.4093375	14.22	DA+dM	19500.0	8.0	3475.0	26.0	00	3,4
23260-2226	352.1615109	-22.1721571	16.80	DA	19590.0[b]	8.01[b]	3212.5	32.0	11	5

Table A.2: References: (1) Dennihy et al. (2017a); (2) Rocchetto et al. (2015) (3) Kilkenny et al. (2015); (4) Kilkenny et al. (2016); (5) Hoard et al. (2007); (6) Farihi et al. (2010); (7) Tappert et al. (2007); (8) Kilkenny et al. (1997); (9) Tappert et al. (2007); (10) Downes et al. (2001); (11) O'Donoghue et al. (2013). Footnote[a] denotes spectroscopic parameters from Koester et al. (2009). Footnote[b] denotes spectroscopic parameters from Gianninas et al. (2011).

Table A.3: Region 3: White Dwarfs with High Temperature/Low Radius Excesses

EC Name	Right Ascension (J2000)	Declination (J2000)	V (mag)	EC Sptype	WD T_{eff} (K)	WD $\log g$ (cm^{-2})	BB T_{eff} (K)	BB Rad (R_{WD})	Im Flag	Ref
00169-3216	4.8518404	-31.9982455	15.67	sdB/DA?	30750.0	8.0	4287.5	5.0	10	1
02121-5743	33.4391834	-57.4967862	14.34	DAwk	17000.0	8.0	4625.0	2.0	00	1
03120-6650	48.1736862	-66.6561967	16.73	DA/sdB	24250.0	8.0	5125.0	2.0	20	1
03372-5808	54.5997256	-57.9739414	16.45	DA	44250.0	8.0	5500.0	3.0	00	1
03572-5455	59.6228876	-54.7779686	16.09	sdB?/DA?	22250.0	8.0	5287.5	3.0	00	1
04536-2933	73.8992797	-29.4835602	14.97	DAB	20640.0[b]	7.61[b]	4925.0	1.0	20	1
10188-1019	155.3301617	-10.5804209	16.35	DA5	17720.0[b]	8.52[b]	4612.5	2.0	20	1
11437-3124	176.575735	-31.6839625	17.32	DA1	38810.0[b]	8.04[b]	5412.5	4.0	20	1
14572-0837	224.9707361	-8.8247843	15.77	DA2	21448.0[a]	7.92[a]	4500.0	2.0	20	2
19579-7344	300.9522623	-73.5956704	16.65	DA	25250.0	8.0	4975.0	3.0	20	1
20228-5030	306.6264874	-50.3451028	17.13	DA	21250.0	8.0	5500.0	3.0	20	1
21591-7353	330.8978119	-73.6455014	14.46	DA	19750.0	8.0	4812.5	3.0	20	1
22185-2706	335.3493648	-26.8484764	14.76	DA	15039.0[a]	7.8[a]	4825.0	1.0	10	1
23127-4239	348.8769107	-42.392647	16.24	sdB/DAwk	29750.0	8.0	5500.0	2.0	00	1
23513-5536	358.4795859	-55.3316608	16.23	sdB/DA	24000.0	8.0	5275.0	3.0	00	1

Continued on next page

EC Name	Right Ascension (J2000)	Declination (J2000)	V (mag)	EC Sptype	WD T_{eff} (K)	WD $\log g$ (cm^{-2})	BB T_{eff} (K)	BB Rad (R_{WD})	Im Flag	Ref

Table A.3: References: (1) Dennihy et al. (2017a); (2) Farihi et al. (2009). Footnote[a] denotes spectroscopic parameters from Koester et al. (2009). Footnote[b] denotes spectroscopic parameters from Gianninas et al. (2011).

APPENDIX B: HE 1349–2305 OBSERVATIONS

In this appendix, we present the details for the observations of HE 1349–2305 used to measure the short-term variability discussed in subsection 3.4.2

Table B.1: HE 1349–2305 Observations and Ca II triplet Emission Profile Measurements

			Ca II 8498 Å		Ca II 8542 Å		Ca II 8662 Å	
Date	MJD (Days)	Average SNR	EQW (Å)	Centroid Vel (km s^{-1})	EQW (Å)	Centroid Vel (km s^{-1})	EQW (Å)	Centroid Vel (km s^{-1})
2016-08-20	57621.0	29	1.49 ± 0.35	-215 ± 29	1.60 ± 0.47	-215 ± 29	1.64 ± 0.34	-218 ± 37
2017-01-11	57765.3	45	1.47 ± 0.32	160 ± 62	1.67 ± 0.24	121 ± 79	1.61 ± 0.28	156 ± 50
2017-01-24	57778.4	43	1.42 ± 0.30	16 ± 54	1.89 ± 0.44	101 ± 48	1.42 ± 0.39	94 ± 74
2017-02-08	57793.3	33	1.89 ± 0.56	107 ± 47	1.74 ± 0.59	166 ± 78	1.47 ± 0.22	91 ± 43
2017-02-17	57801.3	58	1.56 ± 0.16	144 ± 33	1.55 ± 0.30	181 ± 71	1.07 ± 0.41	252 ± 62
2017-03-10	57822.2	57	1.26 ± 0.14	257 ± 18	1.43 ± 0.15	253 ± 28	1.50 ± 0.29	202 ± 54
2017-03-13	57826.2	35	1.02 ± 0.29	256 ± 41	1.40 ± 0.29	231 ± 45	1.14 ± 0.42	258 ± 72
2017-04-11a	57854.2	50	1.34 ± 0.31	230 ± 20	1.33 ± 0.27	246 ± 19	1.02 ± 0.31	247 ± 26
2017-04-11b	57854.3	52	1.28 ± 0.40	204 ± 31	0.96 ± 0.53	247 ± 78	1.10 ± 0.37	236 ± 25
2017-04-22	57866.2	41	0.97 ± 0.23	223 ± 18	1.64 ± 0.48	207 ± 29	1.42 ± 0.28	227 ± 22
2017-05-29	57903.0	44	0.87 ± 0.29	206 ± 20	1.34 ± 0.17	197 ± 16	1.36 ± 0.38	195 ± 24
2017-06-08	57913.1	32	1.39 ± 0.56	86 ± 58	1.24 ± 0.38	208 ± 32	1.00 ± 0.45	160 ± 44
2017-07-25	57959.0	55	1.14 ± 0.28	41 ± 56	1.53 ± 0.50	64 ± 41	1.16 ± 0.27	64 ± 46
2017-08-02	57968.0	33	1.07 ± 0.62	93 ± 134	1.62 ± 0.27	79 ± 54	1.51 ± 0.38	143 ± 68

Continued on next page

			Ca II 8498 Å		Ca II 8542 Å		Ca II 8662 Å	
Date	MJD	Average SNR	EQW	Centroid Vel	EQW	Centroid Vel	EQW	Centroid Vel
	(Days)		(Å)	(km s^{-1})	(Å)	(km s^{-1})	(Å)	(km s^{-1})

BIBLIOGRAPHY

Barber, S. D., Kilic, M., Brown, W. R., & Gianninas, A. 2014, ApJ, 786, 77

Barber, S. D., Patterson, A. J., Kilic, M., et al. 2012, ApJ, 760, 26

Bergeron, P., Saffer, R. A., & Liebert, J. 1992, ApJ, 394, 228

Bergeron, P., Wesemael, F., & Beauchamp, A. 1995, PASP, 107, 1047

Bernstein, R., Shectman, S. A., Gunnels, S. M., Mochnacki, S., & Athey, A. E. 2003, in Proc. SPIE Conf. Ser., Vol. 4841, Instrument Design and Performance for Optical/Infrared Ground-based Telescopes, ed. M. Iye & A. F. M. Moorwood, 1694–1704

Bianchi, L., Conti, A., & Shiao, B. 2014, VizieR Online Data Catalog, 2335

Bochkarev, K. V., & Rafikov, R. R. 2011, ApJ, 741, 36

Bonsor, A., Farihi, J., Wyatt, M. C., & van Lieshout, R. 2017, MNRAS, 468, 154

Bonsor, A., Mustill, A. J., & Wyatt, M. C. 2011, MNRAS, 414, 930

Bonsor, A., & Veras, D. 2015, MNRAS, 454, 53

Brinkworth, C. S., Gänsicke, B. T., Marsh, T. R., Hoard, D. W., & Tappert, C. 2009, ApJ, 696, 1402

Brown, M. J. I., Moustakas, J., Smith, J.-D. T., et al. 2014, ApJS, 212, 18

Camarota, L., & Holberg, J. B. 2014, MNRAS, 438, 3111

Casewell, S. L., Burleigh, M. R., Wynn, G. A., et al. 2012, ApJL, 759, L34

Casewell, S. L., Lawrie, K. A., Maxted, P. F. L., et al. 2015, MNRAS, 447, 3218

Cauley, P. W., Farihi, J., Redfield, S., et al. 2018, ApJL, 852, L22

Chabrier, G., & Baraffe, I. 1997, A&A, 327, 1039

Chabrier, G., Baraffe, I., Allard, F., & Hauschildt, P. 2000, ApJL, 542, L119

Chayer, P., & Dupuis, J. 2010, in American Institute of Physics Conference Series, Vol. 1273, American Institute of Physics Conference Series, ed. K. Werner & T. Rauch, 394–399

Chiang, E. I., & Goldreich, P. 1997, ApJ, 490, 368

Clemens, J. C., Crain, J. A., & Anderson, R. 2004, in Proc. SPIE Conf. Ser., Vol. 5492, Ground-based Instrumentation for Astronomy, ed. A. F. M. Moorwood & M. Iye, 331–340

Cohen, M., Megeath, S. T., Hammersley, P. L., Martín-Luis, F., & Stauffer, J. 2003a, AJ, 125, 2645

Cohen, M., Wheaton, W. A., & Megeath, S. T. 2003b, AJ, 126, 1090

Croll, B., Dalba, P. A., Vanderburg, A., et al. 2017, ApJ, 836, 82

Cross, N. J. G., Collins, R. S., Mann, R. G., et al. 2012, A&A, 548, A119

Cutri, R. M., & et al. 2013, VizieR Online Data Catalog, 2328

Cutri, R. M., Skrutskie, M. F., van Dyk, S., et al. 2003, VizieR Online Data Catalog, 2246

Debes, J. H., Hoard, D. W., Kilic, M., et al. 2011a, ApJ, 729, 4

Debes, J. H., Hoard, D. W., Wachter, S., Leisawitz, D. T., & Cohen, M. 2011b, ApJS, 197, 38

Debes, J. H., Kilic, M., Faedi, F., et al. 2012a, ApJ, 754, 59

Debes, J. H., & Sigurdsson, S. 2002, ApJ, 572, 556

Debes, J. H., Walsh, K. J., & Stark, C. 2012b, ApJ, 747, 148

Dennihy, E., Clemens, J. C., Debes, J. H., et al. 2017a, ApJ, 849, 77

Dennihy, E., Clemens, J. C., Dunlap, B. H., et al. 2018, ApJ, 854, 40

Dennihy, E., Debes, J. H., & Clemens, C. J. 2017b, in Astronomical Society of the Pacific Conference Series, Vol. 509, 20th European White Dwarf Workshop, ed. P.-E. Tremblay, B. Gaensicke, & T. Marsh, 113

Dennihy, E., Debes, J. H., Dunlap, B. H., et al. 2016, ApJ, 831, 31

Dobbie, P. D., Burleigh, M. R., Levan, A. J., et al. 2005, MNRAS, 357, 1049

Dong, R., Zhu, Z., Rafikov, R. R., & Stone, J. M. 2015, ApJL, 809, L5

Downes, R. A., Webbink, R. F., Shara, M. M., et al. 2001, PASP, 113, 764

Dufour, P., Kilic, M., Fontaine, G., et al. 2010, ApJ, 719, 803

—. 2012, ApJ, 749, 6

Dufour, P., Bergeron, P., Liebert, J., et al. 2007, ApJ, 663, 1291

Farihi, J. 2011, White Dwarf Circumstellar Disks: Observations, ed. D. W. Hoard, 117–171

—. 2016, New Astronomy Reviews, 71, 9

Farihi, J., Becklin, E. E., & Zuckerman, B. 2005, ApJS, 161, 394

Farihi, J., & Christopher, M. 2004, AJ, 128, 1868

Farihi, J., Gänsicke, B. T., Wyatt, M. C., et al. 2012, MNRAS, 424, 464

Farihi, J., Hoard, D. W., & Wachter, S. 2010, ApJS, 190, 275

Farihi, J., Jura, M., & Zuckerman, B. 2009, ApJ, 694, 805

Farihi, J., Parsons, S. G., & Gänsicke, B. T. 2017, Nature Astronomy, 1, 0032

Farihi, J., Zuckerman, B., & Becklin, E. E. 2008, ApJ, 674, 431

Fontaine, G., Brassard, P., & Bergeron, P. 2001, PASP, 113, 409

Frewen, S. F. N., & Hansen, B. M. S. 2014, MNRAS, 439, 2442

Fuchs, J. T. 2017, GitHub repository

Fung, J., & Dong, R. 2015, ApJL, 815, L21

Gänsicke, B., Tremblay, P., Barstow, M., et al. 2016a, in Astronomical Society of the Pacific Conference Series, Vol. 507, Multi-Object Spectroscopy in the Next Decade: Big Questions, Large Surveys, and Wide Fields, ed. I. Skillen, M. Balcells, & S. Trager, 159

Gänsicke, B. T., Koester, D., Farihi, J., et al. 2012, MNRAS, 424, 333

Gänsicke, B. T., Koester, D., Marsh, T. R., Rebassa-Mansergas, A., & Southworth, J. 2008, MNRAS, 391, L103

Gänsicke, B. T., Marsh, T. R., & Southworth, J. 2007, MNRAS, 380, L35

Gänsicke, B. T., Marsh, T. R., Southworth, J., & Rebassa-Mansergas, A. 2006, Science, 314, 1908

Gänsicke, B. T., Aungwerojwit, A., Marsh, T. R., et al. 2016b, ApJL, 818, L7

Gentile Fusillo, N. P., Raddi, R., Gänsicke, B. T., et al. 2017, MNRAS, 469, 621

Gianninas, A., Bergeron, P., & Ruiz, M. T. 2011, ApJ, 743, 138

Girven, J., Brinkworth, C. S., Farihi, J., et al. 2012, ApJ, 749, 154

Graham, J. R., Matthews, K., Neugebauer, G., & Soifer, B. T. 1990, ApJ, 357, 216

Gray, D. F. 2005, PASP, 117, 711

Guo, J., Tziamtzis, A., Wang, Z., et al. 2015, ApJL, 810, L17

Gurri, P., Veras, D., & Gänsicke, B. T. 2017, MNRAS, 464, 321

Hambly, N. C., Collins, R. S., Cross, N. J. G., et al. 2008, MNRAS, 384, 637

Harris, H. C., Munn, J. A., Kilic, M., et al. 2006, AJ, 131, 571

Hartmann, S., Nagel, T., Rauch, T., & Werner, K. 2016, A&A, 593, A67

Heinemann, T., & Papaloizou, J. C. B. 2009a, MNRAS, 397, 52

—. 2009b, MNRAS, 397, 64

—. 2012, MNRAS, 419, 1085

Henden, A. A., Templeton, M., Terrell, D., et al. 2016, VizieR Online Data Catalog, 2336

Henden, A. A., Welch, D. L., Terrell, D., & Levine, S. E. 2009, in American Astronomical Society Meeting Abstracts, Vol. 214, American Astronomical Society Meeting Abstracts #214, 669

Hills, J. G. 1975, Nature, 254, 295

Hoard, D. W., Debes, J. H., Wachter, S., Leisawitz, D. T., & Cohen, M. 2013, ApJ, 770, 21

Hoard, D. W., Wachter, S., Sturch, L. K., et al. 2007, AJ, 134, 26

Holberg, J. B., & Bergeron, P. 2006, AJ, 132, 1221

Horne, K., & Marsh, T. R. 1986, MNRAS, 218, 761

Irwin, M. J., Lewis, J., Hodgkin, S., et al. 2004, in Proc. SPIE Conf. Ser., Vol. 5493, Optimizing Scientific Return for Astronomy through Information Technologies, ed. P. J. Quinn & A. Bridger, 411–422

Jarrett, T. H., Cohen, M., Masci, F., et al. 2011, ApJ, 735, 112

Jura, M. 2003, ApJL, 584, L91

—. 2008, AJ, 135, 1785

Jura, M., Dufour, P., Xu, S., et al. 2015, ApJ, 799, 109

Jura, M., Farihi, J., & Zuckerman, B. 2007a, ApJ, 663, 1285

—. 2009a, AJ, 137, 3191

—. 2009b, AJ, 137, 3191

Jura, M., Farihi, J., Zuckerman, B., & Becklin, E. E. 2007b, AJ, 133, 1927

Jura, M., Klein, B., Xu, S., & Young, E. D. 2014, ApJL, 791, L29

Jura, M., & Xu, S. 2013, AJ, 145, 30

Jura, M., & Young, E. D. 2014, Annual Review of Earth and Planetary Sciences, 42, 45

Kawka, A., Vennes, S., Dinnbier, F., Cibulková, H., & Németh, P. 2011, in American Institute of Physics Conference Series, Vol. 1331, American Institute of Physics Conference Series, ed. S. Schuh, H. Drechsel, & U. Heber, 238–245

Kelson, D. D. 2003, PASP, 115, 688

Kelson, D. D., Illingworth, G. D., van Dokkum, P. G., & Franx, M. 2000, ApJ, 531, 159

Kenyon, S. J., & Bromley, B. C. 2017a, ApJ, 844, 116

—. 2017b, ApJ, 850, 50

Kilic, M., & Redfield, S. 2007, ApJ, 660, 641

Kilic, M., von Hippel, T., Leggett, S. K., & Winget, D. E. 2006, ApJ, 646, 474

Kilkenny, D., O'Donoghue, D., Koen, C., Stobie, R. S., & Chen, A. 1997, MNRAS, 287, 867

Kilkenny, D., O'Donoghue, D., Worters, H. L., et al. 2015, MNRAS, 453, 1879

Kilkenny, D., Worters, H. L., O'Donoghue, D., et al. 2016, MNRAS, 459, 4343

Koester, D. 2009, A&A, 498, 517

—. 2010, Mem. Soc. Astron. Ital., 81, 921

Koester, D., Gänsicke, B. T., & Farihi, J. 2014, A&A, 566, A34

Koester, D., Rollenhagen, K., Napiwotzki, R., et al. 2005, A&A, 432, 1025

Koester, D., Voss, B., Napiwotzki, R., et al. 2009, A&A, 505, 441

Koester, D., & Wilken, D. 2006, A&A, 453, 1051

Koester, D., Napiwotzki, R., Christlieb, N., et al. 2001, A&A, 378, 556

Lang, D. 2014, AJ, 147, 108

Lang, D., Hogg, D. W., & Schlegel, D. J. 2016, AJ, 151, 36

Liebert, J., Bergeron, P., & Holberg, J. B. 2005, ApJS, 156, 47

Loh, E. D., Biel, J. D., Davis, M. W., et al. 2012, PASP, 124, 343

Manser, C. J., Gänsicke, B. T., Koester, D., Marsh, T. R., & Southworth, J. 2016a, MNRAS, 462, 1461

Manser, C. J., Gänsicke, B. T., Marsh, T. R., et al. 2016b, MNRAS, 455, 4467

Martin, D. C., Fanson, J., Schiminovich, D., et al. 2005, ApJL, 619, L1

Maxted, P. F. L., Napiwotzki, R., Dobbie, P. D., & Burleigh, M. R. 2006, Nature, 442, 543

McMahon, R. G., Banerji, M., Gonzalez, E., et al. 2013, The Messenger, 154, 35

Melis, C., Jura, M., Albert, L., Klein, B., & Zuckerman, B. 2010, ApJ, 722, 1078

Melis, C., Dufour, P., Farihi, J., et al. 2012, ApJL, 751, L4

Metzger, B. D., Rafikov, R. R., & Bochkarev, K. V. 2012, MNRAS, 423, 505

Miranda, R., & Rafikov, R. R. 2018, ArXiv e-prints, arXiv:1802.00464

Mustill, A. J., & Villaver, E. 2012, ApJ, 761, 121

Mustill, A. J., Villaver, E., Veras, D., Gänsicke, B. T., & Bonsor, A. 2017, ArXiv e-prints, arXiv:1711.02940

Nicholl, M., Berger, E., Kasen, D., et al. 2017, ApJL, 848, L18

O'Donoghue, D., Kilkenny, D., Koen, C., et al. 2013, MNRAS, 431, 240

Okazaki, A. T. 1991, PASJ, 43, 75

Okazaki, A. T. 2016, in Astronomical Society of the Pacific Conference Series, Vol. 506, Bright Emissaries: Be Stars as Messengers of Star-Disk Physics, ed. T. A. A. Sigut & C. E. Jones, 3

Osterbrock, D. E., Fulbright, J. P., Martel, A. R., et al. 1996, PASP, 108, 277

Pérez, L. M., Carpenter, J. M., Andrews, S. M., et al. 2016, Science, 353, 1519

Raddi, R., Gänsicke, B. T., Koester, D., et al. 2015, MNRAS, 450, 2083

Rafikov, R. R. 2011, ApJL, 732, L3

Rafikov, R. R., & Garmilla, J. A. 2012, ApJ, 760, 123

Rappaport, S., Gary, B. L., Kaye, T., et al. 2016, MNRAS, 458, 3904

Reach, W. T., Lisse, C., von Hippel, T., & Mullally, F. 2009, ApJ, 693, 697

Redfield, S., Farihi, J., Cauley, P. W., et al. 2017, ApJ, 839, 42

Reid, I. N., Brewer, C., Brucato, R. J., et al. 1991, PASP, 103, 661

Reig, P., Negueruela, I., Papamastorakis, G., Manousakis, A., & Kougentakis, T. 2005, A&A, 440, 637

Rocchetto, M., Farihi, J., Gänsicke, B. T., & Bergfors, C. 2015, MNRAS, 449, 574

Roeser, S., Demleitner, M., & Schilbach, E. 2010, AJ, 139, 2440

Schröder, K.-P., & Connon Smith, R. 2008, MNRAS, 386, 155

Shanks, T., Metcalfe, N., Chehade, B., et al. 2015, MNRAS, 451, 4238

Skrutskie, M. F., Cutri, R. M., Stiening, R., et al. 2006, AJ, 131, 1163

Sloan, G. C., Keller, L. D., Forrest, W. J., et al. 2005, ApJ, 632, 956

Sloan, G. C., Jura, M., Duley, W. W., et al. 2007, ApJ, 664, 1144

Spiegel, D. S., & Madhusudhan, N. 2012, ApJ, 756, 132

Steele, P. R., Saglia, R. P., Burleigh, M. R., et al. 2013, MNRAS, 429, 3492

Stern, S. A., Shull, J. M., & Brandt, J. C. 1990, Nature, 345, 305

Subasavage, J. P., Henry, T. J., Bergeron, P., et al. 2007, AJ, 134, 252

Tappert, C., Gänsicke, B. T., Schmidtobreick, L., Mennickent, R. E., & Navarrete, F. P. 2007, A&A, 475, 575

Vanderburg, A., Johnson, J. A., Rappaport, S., et al. 2015, Nature, 526, 546

Vennes, S., & Kawka, A. 2013, ApJ, 779, 70

Veras, D., Jacobson, S. A., & Gänsicke, B. T. 2014a, MNRAS, 445, 2794

Veras, D., Leinhardt, Z. M., Bonsor, A., & Gänsicke, B. T. 2014b, MNRAS, 445, 2244

Veras, D., Leinhardt, Z. M., Eggl, S., & Gänsicke, B. T. 2015, MNRAS, 451, 3453

Villaver, E., & Livio, M. 2007, ApJ, 661, 1192

von Hippel, T., Kuchner, M. J., Kilic, M., Mullally, F., & Reach, W. T. 2007, ApJ, 662, 544

Wilson, D. J., Gänsicke, B. T., Koester, D., et al. 2014, MNRAS, 445, 1878

—. 2015, MNRAS, 451, 3237

Wolszczan, A., & Frail, D. A. 1992, Nature, 355, 145

Wright, E. L., Eisenhardt, P. R. M., Mainzer, A. K., et al. 2010, AJ, 140, 1868

Wyatt, M. C., Farihi, J., Pringle, J. E., & Bonsor, A. 2014, MNRAS, 439, 3371

Xu, S., Jura, M., Dufour, P., & Zuckerman, B. 2016, ApJL, 816, L22

Xu, S., Jura, M., Klein, B., Koester, D., & Zuckerman, B. 2013, ApJ, 766, 132

Xu, S., Jura, M., Koester, D., Klein, B., & Zuckerman, B. 2014, ApJ, 783, 79

Xu, S., Zuckerman, B., Dufour, P., et al. 2017, ApJL, 836, L7

Zuckerman, B. 2015, in Astronomical Society of the Pacific Conference Series, Vol. 493, 19th European Workshop on White Dwarfs, ed. P. Dufour, P. Bergeron, & G. Fontaine, 291

Zuckerman, B., & Becklin, E. E. 1987, Nature, 330, 138

Zuckerman, B., Koester, D., Reid, I. N., & Hünsch, M. 2003, ApJ, 596, 477